KHz) and current swing of the oscillator circuit (Kim & Hawks, 1989). The square-wave oscillator output of each of three identical channels is fed directly to the onboard microprocessor without the need for complicated interface circuitry.

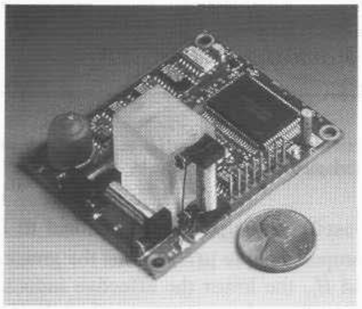

Figure 12-18. The *TCM* compass employs a three-axis strap-down magnetometer in conjunction with a two-axis tilt sensor to compensate for variations in vehicle attitude (courtesy Precision Navigation, Inc.).

Automatic distortion-detection algorithms are incorporated that raise a warning flag when magnetic disturbances (i.e., close-proximity metallic objects or electrical cabling) are compromising compass accuracy. Pitch-and-roll outputs are available for external use with 0.1-degree resolution at an accuracy of ±0.2 degrees. Ambient temperature information is also provided over a range of -20 to +70°C, with an accuracy of ±0.5 degrees. Both digital outputs (RS-232 or NMEA-0183) and linear quadrature analog outputs (0-5 volts) are standard.

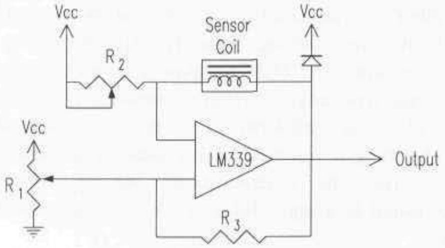

Figure 12-19. Block diagram of a single-axis sense element as implemented on the *TCM* compass (adapted from Kim & Hawks, 1989).

Power requirements for the *TCM* compass are 5 to 25 volts DC at 6 to 12 milliamps, depending on user configuration. The OEM circuit board measures 2.5

by 2 inches wide by 1.1 inches high, weighs 1.6 ounces, and with a tilt range of ±25 degrees costs only $700. (Additional tilt ranges of 60 and 90 degrees are also available at slightly higher cost.) The moderate price, extremely low power consumption, elimination of gimbal-induced measurement errors, small size and weight, plus availability of pitch, roll, and ambient temperature outputs make the *TCM-Series* a strong contender for mobile robotic applications. Field performance evaluations are currently underway for early prototypes installed on both ROBART III and the MDARS Interior robot (Chapter 1).

An extremely low-cost ($50) two-axis electronic compass without tilt compensation, the *Vector-2X*, is available as well for less demanding applications, with an overall accuracy of ±2 degrees.

12.4 Hall-Effect Compasses

Recall from Section 3.2.1 that *Hall-effect* sensors in the presence of an external magnetic field develop a DC voltage across a semiconductor region that is proportional to the magnetic field component at right angles to the direction of current flow (Wood, 1986). One advantage of this technology (i.e., relative to the fluxgate) is the inherent ability to directly sense a static flux, resulting in much simpler readout electronics. Early Hall magnetometers could not match the sensitivity and stability of the fluxgate (Primdahl, 1979), but the sensitivity of Hall devices has improved significantly. The more recent indium-antimonidide devices have a lower sensitivity limit of 10^{-3} Gauss (Lenz, 1990).

The Navy in the early 1960s showed considerable interest in a small solid-state Hall-effect compass for low-power extended operations in sonobuoys (Wiley, 1964). A number of such prototypes were built and delivered by Motorola for evaluation. The Motorola compass employed two orthogonal Hall-effect devices for temperature-nulled non-ambiguous resolution of the geomagnetic field vector. Each sensor element was fabricated from a 2- by 2- by 0.1-millimeter indium-arsenide-ferrite sandwich and inserted between two wing-like *mumetal* flux concentrators as shown in Figure 12-20. It is estimated the 2-inch magnetic concentrators increased the flux density through the sensing elements by two orders of magnitude (Wiley, 1964). The output of the Motorola unit was a variable-width pulse train, the width of the pulse being proportional to the sensed magnetic heading. Excellent response linearity was reported down to flux densities of 0.01 Gauss (Wiley, 1962).

Maenaka, et al. (1990) report on the development of a monolithic silicon magnetic compass at the Toyohashi University of Technology in Japan, based on two orthogonal Hall-effect sensors. Their use of the terminology "magnetic compass" is perhaps an unfortunate misnomer, in that the prototype device was tested with an external field of 1,000 Gauss. Contrast this field strength with that of the earth's magnetic field, which varies from only about 0.1 Gauss at the equator to about 0.9 Gauss at the poles. Silicon-based Hall-effect sensors have a lower sensitivity limit of around 10 Gauss (Lenz, 1990). It is likely the Toyohashi University device was intended for other than geomagnetic applications, such as remote position sensing of rotating mechanical assemblies.

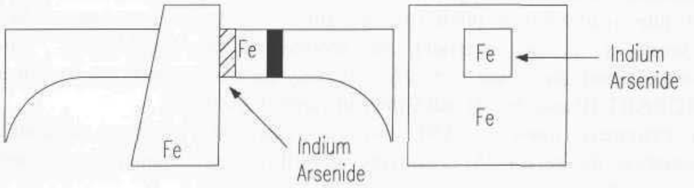

Figure 12-20. A pair of indium-arsenide-ferrite Hall-effect sensors (one shown) are positioned between flux concentrating wings of *mumetal* in this early Motorola prototype (adapted from Wiley, 1964).

This prototype Hall-effect magnetometer is still of interest in that it represents one of the first fully self-contained implementations of a two-axis magnetometer in integrated circuit form. Two vertical Hall cells (Maenaka, et al, 1987) are arranged at right angles as shown in Figure 12-21 on a 4.7-millimeter square chip, with their respective outputs coupled to a companion signal processing IC of identical size. (Two separate chips were fabricated for the prototype instead of a single integrated unit to enhance production yield.) The sensor and signal processing ICs are interconnected (along with some external variable resistors for calibration purposes) on a glass-epoxy printed circuit board.

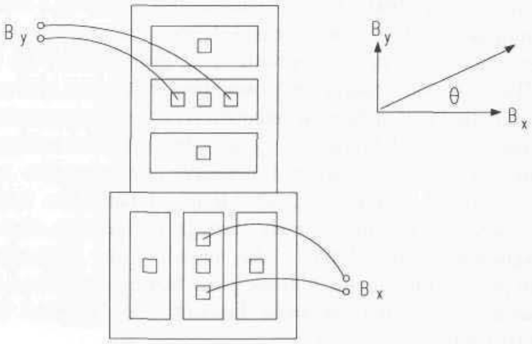

Figure 12-21. Two vertical Hall cells are arranged at right angles on a 4.7-millimeter-square chip in this two-axis magnetometer developed at the Toyohashi University of Technology in Japan (adapted from Maenaka, et al., 1990).

The dedicated signal-processing circuitry converts the *B*-field components B_x and B_y measured by the Hall sensors into an angle θ by means of the analog operation (Maenaka, et al, 1990):

$$\theta = \arctan \frac{B_x}{B_y}$$

where:

θ = angle between B-field axis and sensor
B_x = x-component of B field
B_y = y-component of B field.

The analog output of the signal-processing IC is a DC voltage that varies linearly with vector orientation of the ambient magnetic field in a plane parallel to the chip surface. Reported test results show a fairly straight-line response (i.e., ±2 percent full scale) for external field strengths ranging from 8,000 Gauss down to 500 Gauss; below this level performance begins to degrade rapidly (Maenaka, et al., 1990). A second analog output on the IC provides an indication of the absolute value of field intensity.

While the Toyohashi "magnetic compass" prototype based on silicon Hall-effect technology is incapable of detecting the earth's magnetic field, it is noteworthy nonetheless. A two-axis monolithic device of similar nature employing the more sensitive indium-antimonide Hall devices could potentially have broad appeal for low-cost applications on mobile robotic platforms. For increased sensitivity, an alternative possibility would be to use magnetoresistive sensor elements, to be discussed in the next section.

12.5 Magnetoresistive Compasses

The general theory of operation for *anisotropic magnetoresistive (AMR)* and *giant magnetoresistive (GMR)* sensors as used in short-range proximity detection was previously presented in Chapter 3. Recall three properties of the *magnetoresistive* magnetometer make it well suited for application as a geomagnetic sensor: 1) high sensitivity, 2) directionality, and 3) in the case of AMR sensors, the characteristic "flipping" action associated with the direction of internal magnetization.

AMR sensors have an open-loop sensitivity range of 10^{-2} to 50 Gauss (which easily covers the 0.1- to 1.0-Gauss range of the earth's horizontal magnetic field component), and limited-bandwidth closed-loop sensitivities approaching 10^{-6} Gauss (Lenz, 1990). Excellent sensitivity, low power consumption, small package size, and decreasing cost make both AMR and GMR sensors increasingly popular alternatives to the more conventional fluxgate designs used in robotic vehicle applications.

12.5.1 Philips AMR Compass

One of the earliest magnetoresistive sensors to be applied to a magnetic compass application is the *KMZ10B* offered by Philips Semiconductors BV, The Netherlands (Dibburn & Petersen, 1983; Kwiatkowski & Tumanski, 1986; Petersen, 1989). The limited sensitivity of this device (approximately 0.1 mV/A/m with a supply voltage of 5V DC) in comparison to the earth's maximum horizontal magnetic field (15 A/m) means that considerable attention must be given to the error-inducing effects of temperature and offset drift (Petersen, 1989).

One way around these problems is to exploit the "flipping" phenomenon (Chapter 3) by driving the device back and forth between its two possible magnetization states with square-wave excitation pulses applied to an external coil (Figure 12-22). This switching action toggles the sensor's axial magnetic field as shown in Figure 12-22A, resulting in the alternating response characteristics depicted in Figure 12-22B. Since the sensor offset remains unchanged while the signal output due to the external magnetic field H_y is inverted (Figure 12-22A), the undesirable DC offset voltages can be easily isolated from the weak AC signal.

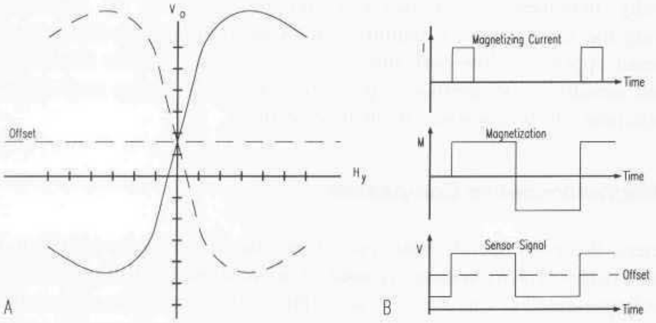

Figure 12-22. External current pulses set and reset the direction of magnetization, resulting in the "flipped" response characteristics shown by the dashed line. Note the DC offset of the device remains constant, while the signal output is inverted (adapted from Petersen, 1989).

A typical implementation of this strategy is shown in Figure 12-23. A 100-Hz square-wave generator is capacitively coupled to the external excitation coil L which surrounds two orthogonally mounted magnetoresistive sensors. The sensors' output signals are amplified and AC-coupled to a synchronous detector driven by the same square-wave source. The rectified DC voltages V_{H1} and V_{H2} are thus proportional to the measured magnetic field components H_1 and H_2. Determination of applied field direction is dependent on the ratio as opposed to absolute values of these output signals, and so as long as the two channels are calibrated to the same sensitivity, no temperature correction is required (Fraden, 1993).

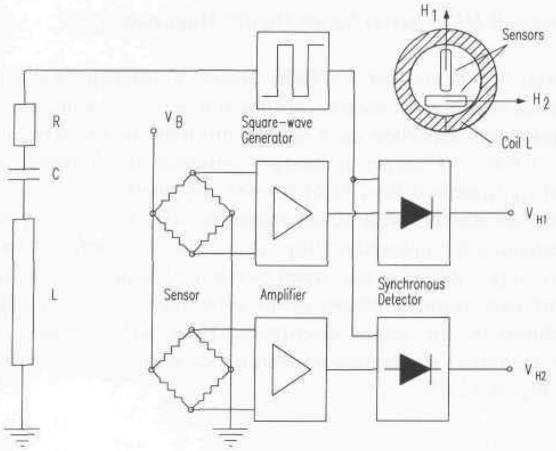

Figure 12-23. Block diagram of a two-axis magnetic compass system based on a commercially available anisotropic magnetoresistive sensor such as the Philips *KMZ10B* (Petersen, 1989).

12.5.2 Space Electronics AMR Compass

The Space Electronics *Micro-Mag* sensor introduced in Chapter 3 (SEI, 1994; Lao, 1994) can be configured as shown in Figure 12-24 to function as an anisotropic magnetoresistive (AMR) compass. The integral 350-ohm temperature compensation resistor (RTD) is connected in the lower arm of a Wheatstone bridge in series with a 100-ohm 10-turn trimming resistor. Two identical channels are required, with their associated AMR sensors mounted in an orthogonal fashion to yield output voltages proportional to the sine and cosine of magnetic field azimuth.

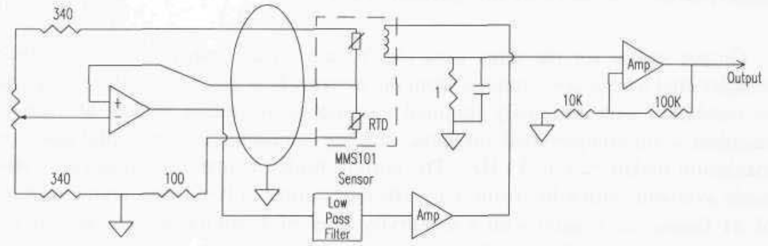

Figure 12-24. Typical application circuit for the SEI *MMS101 MicroMag* that provides an output voltage proportional to the cosine of magnetic azimuth for a gimbaled sensor in the horizontal plane (courtesy Space Electronics, Inc.).

12.5.3 Honeywell *HMR Series Smart Digital Magnetometer*

The *Honeywell Magnetoresistive (HMR) Series* of magnetometers incorporates three orthogonal sensor axes, each consisting of a *permalloy* thin-film Wheatstone bridge configuration deposited on a silicon substrate as discussed in Chapter 3 (Honeywell, 1994b). Changes in bridge resistance are converted to a digital output signal (prespecified RS-232 or RS-485) by internal A/D converters and a dedicated microprocessor, with 12-bit output resolution (11 bits plus sign). A switching technique is employed to "flip" the sensor characteristics back and forth between the two possible magnetic states (see again Chapter 3), thus canceling the DC offset and past magnetic history of the *permalloy* bridges, in addition to any offset introduced by the sensor electronics (Honeywell, 1994a). The unit is packaged in a compact rectangular enclosure measuring 1.12 by 1.75 by 3 inches as shown in Figure 12-25.

Figure 12-25. The Honeywell *HMR-Series Smart Digital Magnetometer* is a three-axis magnetoresistive magnetometer with a sensitivity of 1 milliGauss over a measurement range of ±1 Gauss (courtesy Honeywell Solid State Electronics Center).

Output values for the three axes (X, Y, and Z) are transmitted in two-byte hexadecimal format upon request from the external host processor, where they can be combined with externally supplied information regarding vehicle attitude to calculate a tilt-compensated magnetic heading solution. At 38.4 kilobaud, the maximum update rate is 54 Hz. The current bridge temperature reading is also made available with 8-bit resolution. The magnetometer has a measurement range of ±1 Gauss (each axis) with a sensitivity level of 1 milliGauss and provides a digital resolution of 0.5 milliGauss per least-significant bit. Overall accuracy is ±1 percent of full scale. Power requirements are 12 to 15 volts DC (single supply) at 40 milliamps. An *HMR Series* Development Kit is now available from the Honeywell Solid State Electronics Center, Plymouth, MN, that includes the magnetometer, power supply, cabling, operating manual, and IBM-compatible PC software.

12.6 Magnetoelastic Compasses

A number of researchers have recently investigated the use of *magnetoelastic* (also known as *magnetostrictive*) materials as sensing elements for high-resolution magnetometers. The principle of operation is based on the changes in Young's modulus experienced by magnetic alloys when exposed to an external magnetic field. The *modulus of elasticity E* of a given material is basically a measure of its stiffness, and directly relates stress to strain as follows:

$$E = \frac{\sigma}{\varepsilon}$$

where:

E = Young's modulus of elasticity
σ = applied stress
ε = resulting strain.

Any ferromagnetic material will experience some finite amount of strain (expansion or shrinkage) in the direction of magnetization due to this *magnetostriction* phenomenon. It stands to reason that if the applied stress σ remains the same, strain ε will vary inversely with any change in Young's modulus E. In certain amorphous metallic alloys, this effect is very pronounced.

Barrett, et al. (1973) propose a qualitative explanation, wherein individual atoms in the crystal lattice are treated as tiny magnetic dipoles. The forces exerted by these dipoles on one another depend upon their mutual orientation within the lattice; if the dipoles are aligned end to end, the opposite poles attract, and the material shrinks ever so slightly. The crystal is said to exhibit a negative *magnetostriction constant* in this direction. Conversely, if the dipoles are rotated into side-by-side alignment through the influence of some external field, like poles will repel, and the result is a small expansion.

It follows the strength of an unknown magnetic field can be accurately measured if suitable means is employed to quantify the resulting change in length of some appropriate material displaying a high *magnetostriction constant*. There are currently at least two measurement technologies with the required resolution allowing the magnetoelastic magnetometer to be a realistic contender for high-sensitivity low-cost performance: 1) *interferometric* displacement sensing and 2) *tunneling-tip* displacement sensing.

Lenz (1990) describes a *magnetoelastic* magnetometer which employs a Mach-Zender fiber-optic interferometer to measure the change in length of a *magnetostrictive* material when exposed to an external magnetic field. A laser source directs a beam of light along two optical fiber paths by way of a beam splitter as shown in Figure 12-26. One of the fibers is coated with a material (nickel iron was used) exhibiting a high *magnetostrictive* constant. The length of this fiber therefore is stretched or compressed in conjunction with any *magnetoelastic* expansion or contraction of its coating. The output beam from this fiber-optic cable is combined in a light coupler with the output beam from the uncoated reference fiber and fed to a pair of photodetectors.

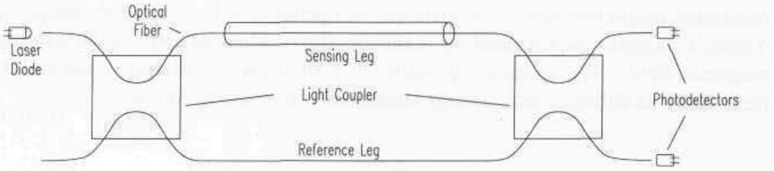

Figure 12-26. Fiber-optic magnetometers, basically a Mach-Zender interferometer with one fiber coated or attached to a magnetoelastic material, have a sensitivity range of 10^{-7} to 10 Gauss (adapted from Lenz, 1990, © IEEE).

Constructive and destructive interferences caused by differences in path lengths associated with the two fibers will cause the final output intensity as measured by the photodetectors to vary accordingly. This variation is directly related to the change in path length of the coated fiber, which in turn is a function of the magnetic field strength along the fiber axis. The prototype constructed by Lenz (1990) at Honeywell Corporation measured 4 inches long by 1 inch wide and was able to detect fields ranging from 10^{-7} Gauss up to 10 Gauss.

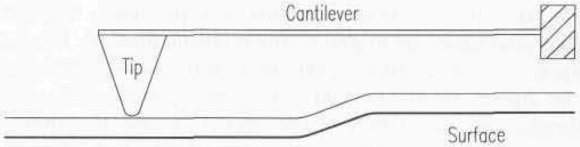

Figure 12-27. *Scanning tunneling microscopy*, invented at IBM Zurich in 1982, uses quantum mechanical tunneling of electrons across a barrier to measure separation distance at the gap (courtesy T.W. Kenny, NASA JPL).

Researchers at the Naval Research Laboratory (NRL) have developed a prototype *magnetoelastic* magnetometer capable of detecting a field as small as 6 x 10^{-5} Gauss using the *tunneling-tip-transducer* approach (Brizzolara, et al., 1989). This new displacement sensing technology, invented in 1982 at IBM Zurich, is based on the measurement of current generated by quantum mechanical tunneling of electrons across a narrow gap (Figure 12-27). An analog feedback circuit compares the measured tunnel current with a desired setpoint and outputs a drive signal to suitably adjust the distance between the tunneling electrodes with an electromechanical actuator (Kenny, et al., 1991). The instantaneous tunneling current is directly proportional to the exponential of electrode displacement. The most common actuators employed in this role are piezoelectric and electrostatic, the latter lending itself more readily to silicon micromachining techniques.

The active sense element in the NRL magnetometer is a 10-centimeter metallic-glass ribbon made from *METGLAS 2605S2*, annealed in a transverse magnetic field to yield a high magnetomechanical coupling (Brizzolara, et al., 1989). The magnetoelastic ribbon elongates when exposed to an axial magnetic field, and the magnitude of this displacement is measured by a tunneling transducer as illustrated in Figure 12-28.

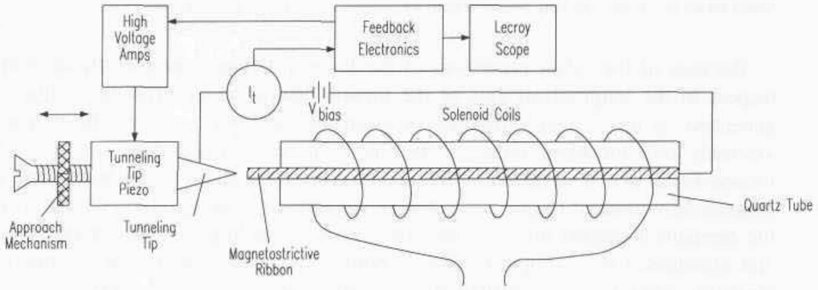

Figure 12-28. The NRL tunneling-transducer magnetometer employed a 10-centimeter magnetoelastic ribbon vertically supported in a quartz tube (Brizzolara, et al., 1989).

An electrochemically etched gold tip is mounted on a tubular piezoelectric actuator and positioned within about 1 nanometer of the free end of the *METGLAS* ribbon. The ribbon and tip are electrically biased with respect to each other, establishing a tunneling current that is fed back to the piezo actuator to maintain a constant gap separation. The degree of magnetically induced elongation of the ribbon can thus be inferred from the driving voltage applied to the piezoelectric actuator. The solenoidal coil shown in the diagram supplies a bias field of 0.85 oersted to shift the sensor into its region of maximum sensitivity.

The NRL group in collaboration with the Jet Propulsion Laboratory, Pasadena, CA, has more recently developed an alternative magnetic sensor that uses a tunneling transducer to measure the induced torque on a suspended magnet due to low-frequency field changes (DiLella, et al., 1995). The sensor consists of two micromachined silicon wafers assembled into a structure measuring approximately 1 inch by 1 inch by 0.1 inch (Figure 12-29). The upper wafer includes a permanent magnet attached to a rectangular support suspended from a pair of torsion beams. The underside of the magnet faces the tunneling tip and serves as both the tunneling counter electrode and one of two rotation control electrodes. The lower component consists of the other rotation control electrode and the tunneling tip as illustrated below.

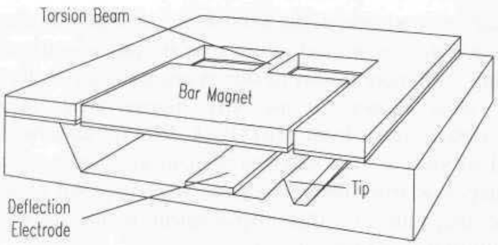

Figure 12-29. Cross-sectional diagram of the NRL/JPL micromachined magnetic-field sensor based on an electron-tunneling displacement transducer (courtesy Naval Research Lab).

Because of the offset placement of the lower rotation control electrode with respect to the longitudinal axis of the torsion beams, an electrostatic torque is generated by the voltage difference between the electrodes, rotating the magnet assembly into tunneling range of the tip. This electrostatic torque about the torsion-beam axis is balanced by the resulting torsional stress in the beams and a magnetically induced torque generated by the ambient magnetic field acting upon the permanent-magnet dipole. Once the desired tunneling current is established and maintained by a simple feedback control circuit, any subsequent change in electrode voltage can be attributed to variations in the ambient magnetic field. The calculated sensitivity limit of this sensor configuration based on fundamental noise sources is 0.002 nT/√Hz at 1 Hz, while the actual measured sensitivity of the prototype is 0.3 nT/√Hz at 1 Hz (DiLella, et al., 1995).

Fenn, et al. (1992) propose yet another tunneling *magnetoelastic* configuration with a predicted sensitivity of 2 x 10^{-11} Gauss, along the same order of magnitude as the cryogenically cooled SQUID. A small cantilevered beam of *METGLAS 2605S2*, excited at its resonant frequency by a gold-film electrostatic actuator, is centered between two high-permeability magnetic flux concentrators as illustrated in Figure 12-30. Any changes in the modulus of elasticity of the beam will directly affect its natural frequency; these changes in natural frequency can then be measured and directly related to the strength of the ambient magnetic field. The effective shift in natural frequency is rather small, however (Fenn reported only a 6-Hz shift at saturation), again necessitating a very precise method of measurement.

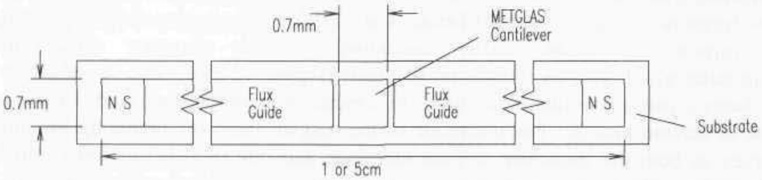

Figure 12-30. Top view of the single cantilevered design (adapted from Fenn, et al., 1992)

A second (non-magnetic) cantilever element is employed to track the displacement of the *METGLAS* reed with subangstrom resolution using tunneling-transducer displacement sensing as illustrated in Figure 12-31. A pair of electrostatic actuator plates dynamically positions the reed follower to maintain constant tunneling current in the probe gap, thus ensuring a constant lateral separation between the probe tip and the vibrating reed. The frequency of the excitation signal applied to the reed-follower actuator is therefore directly influenced by any resonant frequency changes occurring in the *METGLAS* reed. The magnetometer provides an analog voltage output which is proportional to this excitation frequency, and therefore indicative of external magnetic field amplitude.

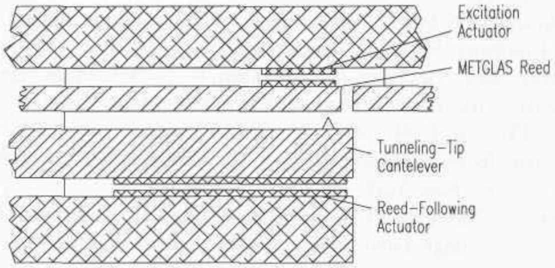

Figure 12-31. Side view of the double cantilevered design (adapted from Fenn, et al., 1992).

One anticipated problem associated with such magnetoelastic devices is that changes in Young's modulus also occur due to temperature shifts. Fenn, et al. (1992) report a 1-Hz bandwidth sensor would require a temperature stability of 10^{-7}°K during the measurement period and suggest thermal isolation using a vacuum jacket and multilayer insulation.

12.7 References

Acuna, M.H., Pellerin, C.J., "A Miniature Two-Axis Fluxgate Magnetometer," *IEEE Transactions on Geoscience Electronics*, Vol. GE-7, pp. 252-260, 1969

Barrett, C.R., Nix, W.D., Tetelman, A.S., *The Principles of Engineering Materials*, Prentice Hall, Englewood Cliffs, NJ, 1973.

Bolz, R.E., Tuve, G.L., eds., *CRC Handbook of Tables for Applied Engineering Science*, CRC Press, Boca Raton, FL, 1979.

Bozorth, R.M., Chapin, D.M., "Demagnetizing Factors of Rods," *Journal of Applied Physics*, Vol. 13, pp. 320-326, May, 1942.

Brizzolara, R.A., Colton, R.J., Wun-Fogle, M., Savage, H.T., "A Tunneling-tip Magnetometer," *Sensors and Actuators*, Vol. 20, pp. 199-205, 1989.

Carlson, A.B., Gisser, D.G., *Electrical Engineering: Concepts and Applications*, Addison-Wesley, Reading, MA, p. 644, 1981.

Carter, E.F., ed., *Dictionary of Inventions and Discoveries*, Crane, Russak, and Co., NY, 1966.

Dahlin, T., Krantz, D., "Low-Cost, Medium Accuracy Land Navigation System," *Sensors*, pp. 26-34, February, 1988.

Dibburn, U., Petersen, A., "The Magnetoresistive Sensor - a Sensitive Device for Detecting Magnetic Field Variations," *Electronic Components and Applications*, Vol. 5, No. 3, June, 1983.

DiLella, D., Colton, R.J., Kenny, T.W., Kaiser, W.J., Vote, E.C., Podosek, J.A., Miller, L.M., "A Micromachined Magnetic-Field Sensor Based on an Electron Tunneling Displacement Transducer," to be published in *Sensors and Actuators*, 1995.

Dinsmore, 1490 and 1525 Magnetic Sensors, Product Literature, Dinsmore Instrument Company, Flint, MI, January, 1991.

Fenn, R.C., Gerver, M.J., Hockney, R.L., Johnson, B.G., "Microfabricated Magnetometer Using Young's Modulus Changes in Magnetoelastic Materials," SPIE Vol. 1694, 1992.

Fraden, J., *AIP Handbook of Modern Sensors*, ed., Radebaugh, R., American Institute of Physics, New York, 1993.

Foster, M., "Vehicle Navigation Using the Plessy Adaptive Compass," RIN Conference Proceedings, Land Navigation and Location for Mobile Applications, York, England, 1985.

Geyger, W.A., *Magnetic Amplifier Circuits*, 2nd ed., McGraw-Hill, New York, 1957.

Geyger, W.A., *J. Appl. Phys*., Vol. 33, suppl., pp. 1280-1281, 1962.

Gilbert, W., "De Magnete," 1600. (Translation: P.F. Mottelay, John Wiley, 1893.)

Gordon, D.I., Lunsten, R.H., *Rev. Phys. Appl*., Vol. 5, pp. 175-177, 1970.

Grenoble, B., "Sensor and Logic Form Digital Compass," *Electronic Design News*, pp. 228-229, 6 December, 1990.

Halliday, D., Resnick, R., *Fundamentals of Physics*, John Wiley, New York, NY, 1974.

Hine, A., *Magnetic Compasses and Magnetometers*, Adam Hilger Ltd., London, 1968.

Honeywell, "Smart Digital Magnetometer," HMR Series Product Literature 900133, Rev. A, Honeywell Solid State Electronics Center, Plymouth, MN, August, 1994a.

Honeywell, "Permalloy Magnetic Sensors," Technical Note, 901XX, Honeywell Solid State Electronics Center, Plymouth, MN, September, 1994b.

ILC, *Synchro Conversion Handbook*, ILC Data Device Corporation, Bohemia, NY, April, 1982.

Kenny, T.W., Waltman, S.B., Reynolds, J.K., Kaiser, W.J., "Micromachined Silicon Tunnel Sensor for Motion Detection," *Applied Physics Letters*, Vol. 58, No. 1, January, 1991.

Kim, N.H., Hawks, T., "Digital Compass and Magnetometer Having a Sensor Coil Wound on a High Permeability Isotropic Core," US Patent 4,851,775, 25 July, 1989.

KVH, *C100 Compass Engine*, Product Literature, KVH Industries, Middletown, RI, April, 1993.

Kwiatkowski, W., Tumanski, S., "The Permalloy Magnetoresistive Sensors - Properties and Applications," *Journal of Physics E: Scientific Instruments*, Vol. 19, pp. 502-515, 1986.

Lao, R., "A New Wrinkle in Magnetoresistive Sensors," *Sensors*, pp. 63-65, October, 1994.

Lenz, J.E., "A Review of Magnetic Sensors," *Proceedings of the IEEE*, Vol. 78, No. 6, June, 1990.

Maenaka, K., Ohgusu, T., Ishida, M., Nakamura, T., "Novel Vertical Hall Cells in Standard Bipolar Technology," *Electronic Letters*, Vol. 23, pp. 1104-1105, 1987.

Maenaka, K., Tsukahara, M., and Nakamura, T., "Monolithic Silicon Magnetic Compass," *Sensors and Actuators*, pp. 747-750, 1990.

Petersen, A., "Magnetoresistive Sensors for Navigation," Proceedings, 7th International Conference on Automotive Electronics, London, England, pp. 87-92, October, 1989.

PNI, "TCM1 Electronic Compass Module: User's Manual," Rev. 1.01, Precision Navigation, Inc., Mountain View, CA, March, 1994

Primdahl, F., "The Fluxgate Mechanism, Part I: The Gating Curves of Parallel and Orthogonal Fluxgates," *IEEE Transactions on Magnetics*, Vol. MAG-6, No. 2, June, 1970.

Primdahl, F., "The Fluxgate Magnetometer," *Journal of Physics E: Scientific Instruments*, Vol. 12, pp. 241-253, 1979.

Rahim, W., "Feedback Limited Control System on a Skid-Steer Vehicle," ANS Fifth Topical Meeting on Robotics and Remote Systems, Knoxville, TN, Vol. 1, pp. 37-42, April, 1993.

Ramsden, E., "Measuring Magnetic Fields with Fluxgate Sensors," *Sensors*, pp. 87-90, September, 1994.

SEI, "High-Sensitivity Magnetoresistive Magnetometer," Product Literature, MMS101, Space Electronics, Inc., San Diego, CA, June, 1994.

Stuart, W.F., "Earth's Field Magnetometry, *Reports on Progress in Physics*, J.M. Zinman, Editor, Vol. 35, Part 2, pp. 803-881, 1972.

Udd, E., "Fiber Optic Sensors Based on the Sagnac Interferometer and Passive Ring Resonator," in Fiber Optic Sensors: An Introduction for Engineers and Scientists, E. Udd, Editor, John Wiley, New York, pp. 233-269, 1991.

Wiley, C.M., "Technical Review of Next Week's National Electronics Conference," *Electronics*, p. 39-41, October 5, 1962.

Wiley, C.M., "Navy Tries Solid-State Compass," *Electronics*, pp. 57-58, February 14, 1964.

Wood, T., "The Hall-Effect Sensor," *Sensors*, pp. 27-36, March, 1986.

13

Gyroscopes

Gyroscopes are for the most part insensitive to the electromagnetic and ferromagnetic anomalies that affect the accuracy of compasses and are particularly useful in applications where there is no geomagnetic field present at all (i.e., deep space), or in situations where the local field is disturbed. Two broad categories of gyroscopes will be discussed: 1) *mechanical gyroscopes* and 2) *optical gyroscopes*.

Mechanical gyroscopes operate by sensing the change in direction of some actively sustained angular or linear momentum, which in either case can be continuous or oscillatory in nature (Cochin, 1963). Probably the most well-known mechanical configuration is the *flywheel gyroscope*, a reliable orientation sensor based on the inertial properties of a rapidly spinning rotor, first demonstrated in 1810 by G.C. Bohnenberger of Germany. In 1852, the French physicist Leon Foucault showed that such a gyroscope could detect the rotation of the earth (Carter, 1966). More recently there has been considerable interest shown in a number of new products classified as *vibrating structure gyroscopes* earmarked for applications in stabilized camera optics, robotics, and intelligent-vehicle highway systems.

Optical gyroscopes have been under development now as replacements for their mechanical counterparts for over three decades. With little or no moving parts, such rotation sensors are virtually maintenance free and display no gravitational sensitivities, eliminating the need for gimbaled mounting. Fueled by a large anticipated market in the automotive industry, highly linear fiber-optic versions are now evolving that have wide dynamic range and very low projected costs.

There are two basic classes of rotation-sensing gyros, whether optical or mechanical in nature: 1) *rate gyros*, which provide a voltage or frequency output signal proportional to the turning rate and 2) *rate integrating gyros*, which indicate the actual turn angle or heading (Udd, 1991). Unlike the magnetic compass discussed in Chapter 12, however, *rate integrating gyros* can only measure relative as opposed to absolute angular position and must be initially referenced to a known orientation by some external means. One convenient way to accomplish this objective takes advantage of the earth's natural rotation..

13.1 Mechanical Gyroscopes

Mechanical gyros operate on the basis of *conservation of momentum* and can be characterized by the type of momentum sustained as follows (Cochin, 1963):

- *Continuous angular momentum* — includes the familiar spinning-rotor *flywheel gyro* and the more esoteric *electron* and *particle gyros*.
- *Oscillatory angular momentum* — employs a torsionally suspended mass oscillating back and forth at its natural frequency.
- *Continuous linear momentum* — incorporates a steady stream of fluid, plasma, or electrons, which tends to maintain its established velocity vector as the platform turns. For example, one concept uses a differential pair of hot-wire anemometers to detect the apparent lateral displacement of a flowing air column.
- *Oscillatory linear momentum* — utilizes a set of discrete masses moving back and forth (radially or in parallel) along a straight-line path. The increasingly popular *tuning-fork rate gyro*, to be discussed later in Section 13.1.3, is a good example of a radial-motion gyroscope of this type.

From a robotics perspective, the two most relevant of the above categories are the *flywheel* and *tuning-fork* gyroscopes.

13.1.1 Space-Stable Gyroscopes

The conventional *flywheel gyroscope* consists of a rapidly spinning wheel or sphere with most of its mass concentrated in the outer periphery, supported by low-friction bearings on either end of the spin axis (Cochin, 1963). Anyone who has ever ridden a bicycle has experienced (perhaps unknowingly) an interesting characteristic of this particular gyro configuration known as *gyroscopic precession*. If the rider leans the bike over to the left around its own horizontal axis, the front wheel turns left in response around the vertical axis. The effect is much more noticeable if the wheel is removed from the bike and held by both ends of its axle while rapidly spinning. If the person holding the wheel attempts to yaw it left or right about the vertical axis, a surprisingly violent reaction will be felt as the axle instead twists about the horizontal roll axis. This is due to the angular momentum associated with a spinning flywheel, which displaces the applied force by 90 degrees in the direction of spin.

The *rate of precession* Ω is proportional to the applied torque T (Fraden, 1993):

$$T = I\omega\Omega$$

where:

T = applied input torque
I = rotational inertia of rotor
ω = rotor spin rate
Ω = rate of precession.

Gyroscopic precession is a key factor involved in the operation of the *north-seeking gyrocompass*, as will be discussed in the next section.

The earth's rotational velocity at any given point on the globe can be broken up into two components: one which acts around an imaginary vertical axis normal to the surface, and another which acts around an imaginary horizontal axis tangent to the surface. These two components are known as the *vertical earth rate* and the *horizontal earth rate*, respectively. At the North Pole, for example, the component acting around the local vertical axis (*vertical earth rate*) would be precisely equal to the rotation rate of the earth, or 15 degrees per hour. As the point of interest moves down a meridian towards the equator, the *vertical earth rate* at that particular location decreases proportionally to a value of zero at the equator. Meanwhile, the *horizontal earth rate* (i.e., that component acting around a horizontal axis tangent to the earth's surface) increases from zero at the pole to a maximum value of 15 degrees-per-hour at the equator.

A typical two-axis *flywheel gyroscope* configuration is shown in Figure 13-1. The electrically driven *rotor* is suspended in a pair of precision low-friction bearings at either end of the rotor axle. The *rotor bearings* are in turn supported by a circular ring known as the *inner gimbal ring*, which in turn pivots on a second set of bearings that attach it to the *outer gimbal ring*. This pivoting action of the *inner gimbal* defines the *horizontal axis* of the gyro, which is perpendicular to the *spin axis* of the *rotor* as shown in the figure. The *outer gimbal ring* is attached to the instrument frame by a third set of bearings that define the *vertical axis* of the gyro. The *vertical axis* is perpendicular to both the *horizontal axis* and the *spin axis*.

Notice that if this configuration is oriented such that the *spin axis* points east-west, the *horizontal axis* is aligned with the north-south meridian. Since the gyro is space-stable (i.e., fixed in the inertial reference frame), the *horizontal axis* thus reads the *horizontal earth rate* component of the planet's rotation, while the *vertical axis* reads the *vertical earth rate* component. If the *spin axis* is rotated 90 degrees to a north-south alignment, the earth's rotation has no effect on the gyro's *horizontal axis*, since that axis is now orthogonal to the *horizontal earth rate* component.

Some finite amount of friction in the support bearings, external influences, and small imbalances inherent in the construction of the rotor cause even the best mechanical gyros to drift with time. Typical systems employed in inertial navigation packages by the commercial airline industry can drift as much as 0.1 degree during a six-hour flight (Martin, 1986).

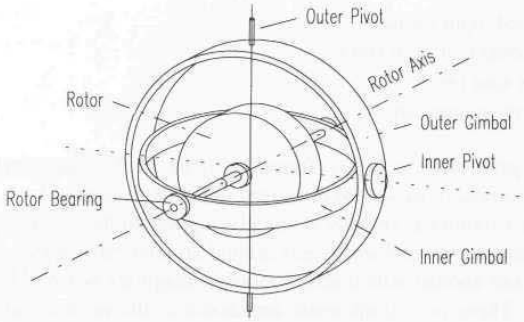

Figure 13-1. Shown here in a typical two-axis configuration, the mechanical *flywheel gyroscope* senses a change in direction of the *angular momentum* associated with a rapidly spinning rotor.

13.1.2 Gyrocompasses

The *gyrocompass* is a special configuration of the *rate integrating flywheel gyroscope*, employing a gravity reference to implement a *north-seeking* function that can be used as a *true-north* navigational reference. This phenomenon, first demonstrated in the early 1800s by Leon Foucault, was patented in Germany by Herman Anschutz-Kaempfe in 1903, and in the US by Elmer Sperry in 1908 (Carter, 1966). The US and German navies had both introduced gyrocompasses into their fleets by 1911 (Martin, 1986). The concept of operation is dependent upon four fundamental principles (Dunlap & Shufeldt, 1972):

- Gyroscopic inertia.
- Gyroscopic precession.
- Earth's rotation.
- Earth's gravitational pull.

Note the *gyrocompass* is in no way dependent upon the earth's geomagnetic field and should not be confused with the *gyromagnetic compass*, wherein a space-stable gyroscope is used to keep a conventional magnetic compass precisely aligned in the horizontal plane (Hine, 1968). The *north-seeking* capability of the *gyrocompass* is instead directly tied to the *horizontal earth rate* component of rotation measured by the gyro's *horizontal axis*. As was pointed out earlier, when the gyro *spin axis* is oriented in a north-south direction, it is insensitive to the earth's rotation, and no tilting occurs. From this it follows that if tilting is observed, the *spin axis* is no longer aligned with the meridian. The direction and magnitude of the measured tilt are directly related to the direction and magnitude of the misalignment between the spin axis and true north.

To transform a two-axis space-stable flywheel gyroscope into a *north-seeking* instrument, some type of weight can be attached to the bottom of the rotor cage in a pendulous fashion to create a simple gravity reference system. Should the gyro spin axis be caused to tilt as a consequence of misalignment with the north-south meridian as discussed above, the restoring weight will be effectively raised against the pull of gravity, creating a torque about the gyro's horizontal axis (Dunlap & Shufeldt, 1972). This resultant torque will in turn induce a perpendicular restoring force that precesses the spin axis back into alignment with the meridian. An alternative non-pendulous approach involves the use of a *mercury ballistic* consisting of one or more pairs of symmetrically arranged vials, partially filled with mercury and connected by a set of equalizing tubes (Arnold & Maunder, 1961; Cochin, 1963).

Primarily used in maritime applications, practical *gyrocompass* implementations today employ an electronic gravity reference system with sophisticated damping, and computer-controlled compensation for host platform speed as well as variations in operating latitude. Such installations are not well suited for mobile robotic applications due to their inherent size and weight, relatively high cost, long spin-up time (i.e., hours) required to initialize, shock and vibration sensitivities, control complexities, and significant power consumption.

13.1.3 Rate Gyros

The common housefly is somewhat unique in the sense that it has only a single pair of wings, instead of two wings on each side of the body as is commonly found on most other flying insects. Remnants of the hind wings, in the form of a pair of small stalks with a swelling at their ends, project outward from the thorax of the fly just behind the base of the wings (Snodgrass, 1930). Known to entomologists as "balancers," or *halteres*, these club-shaped projections consist of two small radially oscillating masses on the ends of cartilage-like fibers, effectively forming a miniature biological *tuning-fork gyro* (Cochin, 1963). If yaw is experienced, the tips of the *halteres* are subjected to *Coriolis forces*, generating muscular signals that assist the acrobatic fly in maintaining controlled flight (Arnold & Maunder, 1961).

Due to its inherent simplicity and reliability, the mechanical *tuning-fork* configuration is one of the most popular low-cost *rate gyroscopes* in use today in land-based mobile applications. Early models consisted of a permanent-magnet fork assembly, torsionally mounted in close proximity to a stationary pair of electromagnetic drive coils (Cochin, 1963). The fork tines were made to vibrate towards and away from one another at a fixed amplitude under temperature-compensated closed-loop control. Any rotation of the gyro assembly about its vertical (torsional) axis caused induced *Coriolis forces* acting on the tines (in the horizontal plane) to generate a harmonic couple about the vertical axis (Arnold & Maunder, 1961). The amplitude of torsional deflection was thus proportional to the rate of turn.

Modern solid-state implementations of the *tuning-fork rate gyro* incorporate *electrostatic* (Boxenhorn, et al., 1989) or *piezoelectric* actuation schemes (Dahlin & Krantz, 1988; Dance, 1993) in lieu of the electromechanical drive mechanisms employed in earlier designs. Variations on the vibratory element include strings, triangular and rectangular bars, cylinders, and hemispheres (Mettler & Hadaegh, 1992). The principles of operation will be addressed in more detail in the following sections describing some commercially available candidate systems.

Systron Donner *GyroChip*

The Systron Donner *GyroChip* is a solid-state angular rate sensor incorporating a micromachined quartz-crystal tuning-fork element and associated electronics sealed in a rugged and compact package as shown in Figure 13-2 (Systron Donner, undated). The double-ended tuning fork and its supporting structure are chemically etched from a single wafer of monocrystalline piezoelectric quartz (Systron Donner, 1994a). The *drive tines* at the upper end of the fork are actively driven toward and away from one another at a precisely controlled amplitude as illustrated in Figure 13-3. Each *drive tine* will experience a *Coriolis force* given by the following equation (Systron Donner, 1992):

$$F = 2m\Omega V_r$$

where:

F = Coriolis force acting on tine
m = mass of tine
Ω = input rotation rate
V_r = instantaneous linear radial velocity of tine.

Figure 13-2. The *GyroChip* solid-state gyro employs a double-ended quartz tuning fork (courtesy Systron Donner Inertial Division).

The *Coriolis force F* is perpendicular to both the input rate Ω and the instantaneous radial velocity V_r. Since the two tines are synchronously moving toward and away from each other, their respective *Coriolis forces* are perpendicular to the plane of the fork assembly, but in opposite directions. The lateral tine offset from the tuning-fork centerline (i.e., the gyro's sensitive axis) causes a torque to be generated by these forces, proportional in magnitude to the input angular velocity (Systron Donner, 1992). In that the *drive-tine* excitation is sinusoidal, the associated radial velocity V_r is also sinusoidal, which means the resultant torque produced by the *Coriolis forces* is sinusoidal as well.

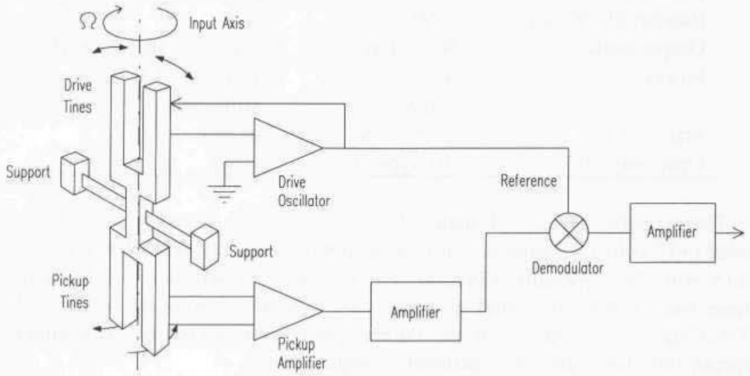

Figure 13-3. Block diagram of the *GyroChip* solid-state rate gyro (courtesy Systron Donner Inertial Division).

The *pick-up tines* react to this oscillating torque by moving in and out of plane as illustrated in Figure 13-3 above, producing a differential signal at the *pick-up amplifier* that is precisely in phase with the radial velocity of the drive tines. The output of the *pick-up amplifier* is then synchronously demodulated (based on the drive oscillator frequency) into a DC signal proportional to the angular rotation rate Ω (Systron Donner, 1992). Since only that component of angular rotation around the axis of symmetry of the tuning fork will generate (from induced Coriolis forces) an oscillating torque at the frequency of the drive tines, synchronous detection ensures input rate sensitivity is uninfluenced by off-axis components (Systron Donner, 1994a).

The *GyroChip* is characterized by a very high *mean-time-between-failure* in excess of 100,000 hours (Orlosky & Morris, 1995) and a low output-noise component that can be classified as *white noise* over a fairly wide operational bandwidth (i.e., all the way down to DC, quite unlike spinning-rotor gyro configurations). The output signal is an analog voltage that varies from 0 to ±2.5 volts DC in accordance with rotational rate and direction, with a linearity typically within less than 0.05 percent of full scale. Selected specifications are provided in Table 13-1 below. The *MotionPak* (Systron Donner, 1994c), an integrated six-DOF package consisting of three rate gyros and three accelerometers is also available for application as a low-cost *inertial navigation system (INS).*

Table 13-1. Selected specifications for the *GyroChip* solid-state rate gyro (courtesy Systron Donner Inertial Division).

Parameter	Value	Units
Range	±10 to ±1000	degrees/second
Scale factor calibration	< 1.0	percent
Linearity	< 0.05	percent full scale
Bandwidth (90 deg.)	> 60	Hz
Output noise	0.012 (typical)	deg./sec/√Hz to 100 Hz
Power	±5	volts DC
	< 0.8	milliwatts
Size	2.25 x 1.92 x .91	inches
Operating life	10 (typical)	years

The recently introduced standard-model *GyroChip II* operates from single-sided (+12 volts DC) supply; a low-noise option is also available for double-sided (±15 volts DC) operation (Systron Donner, 1994b). Selected specifications for these two devices are listed in Table 13-2. A new lower-cost version of the *GyroChip* (i.e., roughly half the current price) is expected to be available in Spring 1995 for slightly less demanding applications.

Table 13-2. Selected specifications for the *GyroChip II* (courtesy Systron Donner Inertial Division).

Parameter	Standard	Low-Noise	Units
Range	±100	±100	degrees/second
Scale factor (±2%)	15	50	millivolts/degree/second
Linearity	< 0.05	< 0.05	percent full scale
Bandwidth (90 deg.)	50	50	Hz
Output noise	< 0.05	< 0.02	degrees/second/√Hz
Power	+12 to + 18	±9 to ±18	volts DC
	35	35 (each)	milliamps
Size	2.34 x 1 x 1	2.34 x 1 x 1	inches
Operating life	> 5	> 5	years

Murata *Gyrostar* Piezoelectric Vibrating Gyroscope

An innovative single-axis *piezoelectric rate gyro* developed by Murata Electronics incorporates three *PZT-6* ceramic elements symmetrically mounted on a triangular metal bar as shown in Figure 13-4 (Nakamura, 1990). If such a bar is made to vibrate in the X direction at its natural frequency f_n, any rotation of the bar around the Z-axis introduces a Coriolis force F_c that causes vibration in the Y direction at the same frequency (Fujishima, 1991):

$$F_c = 2m\Omega\dot{y}$$

where:

F_c = Coriolis force
m = equivalent mass
Ω = angular rotation rate about Z axis.

The actual rotation rate Ω can thus be determined by measuring the amplitude of this induced vibration in the Y direction.

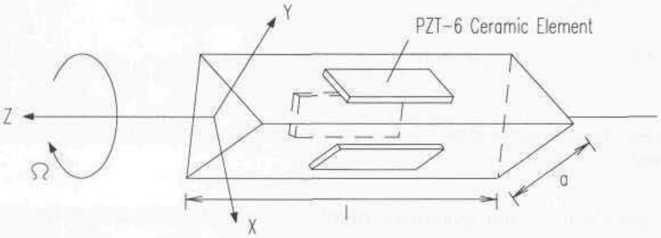

Figure 13-4. Three piezoelectric ceramic elements mounted on a metal bar of triangular cross section form an inexpensive single-axis rate gyro (courtesy Murata Electronics North America).

The flexural resonance frequency of a triangular bar as illustrated in Figure 13-4 is given by (Fujishima, et al., 1991):

$$f_n = \frac{A\,a}{4\pi\,l^2}\sqrt{\frac{E}{6\rho}}$$

where:

A = constant
a = width of bar
l = length of bar
E = Young's modulus of elasticity
ρ = density of bar material.

To ensure good dimensional stability in the Murata gyroscope, the bar is made of *elinvar* (elastic invariable metal), a nickel-chromium-steel alloy with a very small coefficient of thermal expansion (Dance, 1993).

Referring now to Figure 13-5, the 40-millimeter *elinvar* bar is driven into oscillation by the *left* and *right* piezoelectric elements at its natural frequency of 7.85 KHz; a third piezoelectric transducer is used as a detection element to provide feedback to the drive oscillator (Fujishima, et al., 1991). The equilateral-triangle prism arrangement allows the *left* and *right* transducer elements to be located in the direction of the compound vibration mode, and consequently the same *PZT* ceramics can be used for both excitation of the bar and detection of the resultant Coriolis forces (Murata, 1994a).

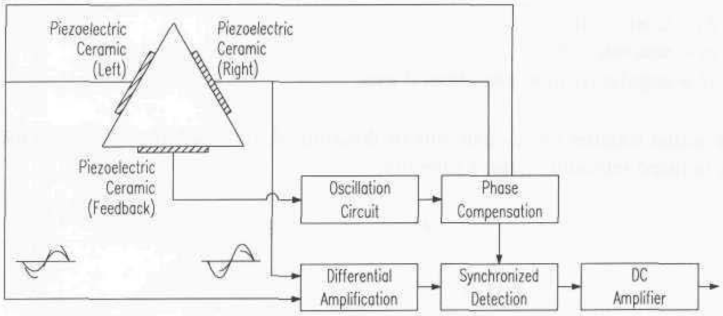

Figure 13-5. Block diagram of the *Gyrostar* piezoelectric rate gyro (courtesy Murata Electronics North America).

The gyro detects and quantifies angular rotation by subtracting the *left* and *right* piezoelectric transducer outputs from each other. This differential amplification scheme provides common-mode rejection of noise and vibration, as the left and right output signals will be equal in magnitude when Ω is zero. As the bar distorts from the effects of rotationally induced Coriolis forces, one detector output increases while the other decreases, effectively doubling the signal magnitude attributed to gyro rotation (Dance, 1993). The differential amplifier output is synchronously detected with respect to the drive oscillator signal, then further amplified to yield an analog voltage that varies linearly above and below a steady-state (no-rotation) value of 2.5 volts DC in response to changes in Ω (Murata, 1994a).

The *Gyrostar's* unique integration of piezoelectric ceramic transducers on an equilateral-triangular prism reportedly offers higher performance than conventional tuning-fork gyros for a tenth of the price (Murata, 1994a). The low power consumption (15 milliamps at 12 volts DC), small package size (roughly 1 by 1 by 2 inches), and low cost (approximately $80 in large quantities) help make the *Gyrostar* a viable and affordable option for a number of consumer as well as mobile robotic applications. On the down side, there is an inherent sensitivity to thermally induced drift (offset and scale factor), in spite of the use of the stable *elinvar* rod material. This tendency to drift is due in part to thermal gradients within the relatively large sensing element, and induced stresses from mismatches in the material thermal expansion rates at the elinvar/ceramic interfaces. Compensation techniques include high-pass filtering to block the DC component of the output signal, and repeated measurement of the offset value under static conditions of zero angular velocity (Murata, 1994a). A detailed technical manual (Murata, 1994b) of test and reliability data including thermal cycle and shock results is available from Murata Electronics North America, Smyrna, GA.

Selected specifications for the *Gyrostar Model ENV-05A* are listed in Table 13-3 below.

Table 13-3. Selected specifications for the *Gyrostar ENV-05A* (courtesy Murata Electronics North America).

Parameter	Value	Units
Range	±90 (max)	degrees/second
Scale factor	22.2	millivolts/degree/second
Scale factor stability	±5 (max)	percent (-10° to 60°C)
Linearity	±0.05 (max)	percent full scale
Hysteresis	0	
Bandwidth	7	Hz
Offset drift	200	millivolts peak-to-peak
Noise level	10 (max)	millivolts DC (rms)
Power	8 - 13.5	volts DC
	15 (max)	milliamps
Size	58 x 25 x 25	millimeters
Weight	45	grams

13.2 Optical Gyroscopes

The principle of operation of the *optical gyroscope*, first discussed by Sagnac (1913), is conceptually very simple, although several significant engineering challenges had to be overcome before practical implementation was possible. In fact, it was not until the demonstration of the helium-neon laser at Bell Labs in 1960 that Sagnac's discovery took on any serious implications; the first operational *ring-laser gyro* was developed by Warren Macek of Sperry Corporation just two years later (Martin, 1986). Navigational quality *ring-laser gyroscopes* were introduced into routine service in inertial navigation systems for the Boeing *757* and *767* in the early 1980s, and over half a million navigation systems have been installed in Japanese automobiles since 1987, many of which employ *fiber-optic gyroscopes* (Reunert, 1993). Numerous technological improvements since Macek's first prototype have made the optical gyro one of the most promising sensors likely to significantly influence mobile robot navigation in the near future.

The basic device consists of two laser beams traveling in opposite directions (i.e., counter-propagating) around a closed-loop path. The constructive and destructive interference patterns formed by splitting off and mixing a portion of the two beams can be used to determine the rate and direction of rotation of the device itself. Schulz-DuBois (1966) idealized the ring laser as a hollow doughnut-shaped mirror, wherein light follows a closed circular path. Assuming an ideal 100-percent reflective mirror surface, the optical energy inside the cavity is theoretically unaffected by any rotation of the mirror itself. The counter-propagating light beams mutually reinforce one another to create a stationary standing wave of intensity peaks and nulls as depicted in Figure 13-6, regardless of whether or not the gyro is rotating (Martin, 1986).

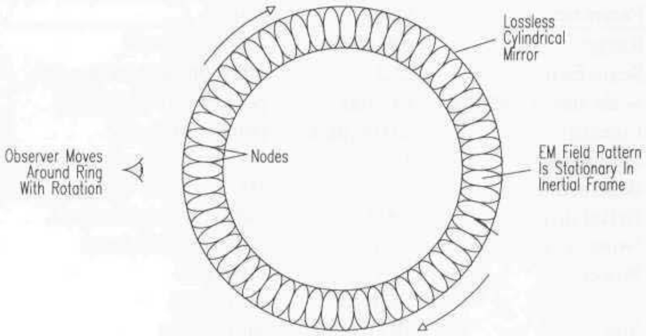

Figure 13-6. Standing wave created by counter-propagating light beams in an idealized ring-laser gyro (adapted from Martin, 1986, © IEEE).

A simplistic visualization based on the Schulz-DuBois idealization is perhaps helpful at this point in understanding the fundamental concept of operation before more detailed treatment of the subject is presented. The light and dark fringes of the nodes are somewhat analogous to the reflective stripes or slotted holes in the rotating disk of an incremental optical encoder and can be theoretically counted in similar fashion by an optical pick-off mounted on the cavity wall (Koper, 1987). (In this analogy, however, the standing-wave "disk" is actually fixed in the inertial reference frame, while the normally stationary "detector" revolves around it.) With each full rotation of the mirrored doughnut, the detector would see a number of node peaks equal to twice the optical path length of the beams divided by the wavelength of the light. For a 632.8-nanometer He-Ne wavelength in a typical 2.4-inch-diameter closed path, there are 300,000 wavelengths and hence 600,000 nodes, yielding over half a million counts per revolution (Koper, 1987).

Obviously, there is no practical way to implement this theoretical arrangement, since there is no such thing as a perfect mirror. Furthermore, the introduction of light energy into the cavity (as well as the need to observe and count the nodes on the standing wave) would interfere with the mirror performance, should such an ideal capability even exist. However, numerous practical embodiments of optical rotation sensors have been developed for use as rate gyros in navigational applications. Five general configurations will be discussed in the following subsections:

- Active optical resonators.
- Passive optical resonators.
- Open-loop fiber-optic interferometers (analog).
- Closed-loop fiber-optic interferometers (digital).
- Fiber-optic resonators.

Aronowitz (1971), Menegozzi & Lamb (1973), Chow, et al. (1985), Wilkinson (1987), and Udd (1991) provide in-depth discussions of the theory of the ring laser gyro and its fiber-optic derivatives. A comprehensive overview of the technologies and an extensive bibliography of preceding works are presented by Ezekiel and Arditty (1982) in the proceedings of the *First International Conference on Fiber Optic Rotation Sensors* held at MIT in November, 1981. An excellent treatment of the salient features, advantages, and disadvantages of *ring-laser gyros* versus *fiber-optic gyros* is presented by Udd (1985; 1991).

13.2.1 Active Ring-Laser Gyros

The *active optical resonator* configuration, more commonly known as the *ring laser gyro*, solves the problem of introducing light into the doughnut by filling the cavity itself with an active lasing medium, typically helium-neon. There are actually two beams generated by the laser that travel around the ring in opposite directions. If the gyro cavity is caused to physically rotate in the counterclockwise direction, then the counter-clockwise-propagating beam will be forced to traverse a slightly longer path than under stationary conditions. Similarly, the clockwise-propagating beam will see its closed-loop path shortened by an identical amount. This phenomenon, known as the *Sagnac effect*, in essence changes the length of the resonant cavity.

The magnitude of this change is given by the equation (Chow, et al., 1985):

$$\Delta L = \frac{4\pi r^2 \Omega}{c}$$

where:

ΔL = change in path length
r = radius of the circular beam path
Ω = angular velocity of rotation
c = speed of light.

Note that the change in path length is directly proportional to the rotation rate Ω of the cavity. Thus, to measure gyro rotation, some convenient means must be established to quantify the associated change in the optical path length.

This requirement to measure minute differences in optical path lengths is where the invention of the laser in the early 1960s provided the needed technological breakthrough that allowed Sagnac's observations to be put to practical use. For lasing to occur in a resonant cavity, the round-trip beam path must be precisely equal in length to an integral number of wavelengths at the resonant frequency. This means the wavelengths (and hence the frequencies) of the two counter-propagating beams must change, as only oscillations with wavelengths satisfying the resonance condition can be sustained in the cavity. The frequency difference between the two beams is given by the following (Chow, et al., 1985):

$$\Delta f = \frac{2fr\Omega}{c} = \frac{2r\Omega}{\lambda}$$

where:

Δf = frequency difference
λ = wavelength.

In practice, a doughnut-shaped ring cavity would be hard to realize. For an arbitrary cavity geometry, the expression becomes (Chow, et al, 1985):

$$\Delta f = \frac{4A\Omega}{P\lambda}$$

where:

A = area enclosed by the closed-loop beam path
P = perimeter of the beam path.

For single-axis gyros, the ring is generally formed by aligning three highly reflective mirrors to create a closed-loop triangular path as shown in Figure 13-7. (Some systems, such as Macek's early prototype, employ four mirrors to create a square path.) The mirrors are usually mounted to a monolithic glass-ceramic block with machined ports for the cavity bores and electrodes. The most stable systems employ linearly polarized light and minimize circularly polarized components to avoid magnetic sensitivities (Martin, 1986). The approximate quantum noise limit is due to spontaneous emission in the gain medium (Ezekiel & Arditty, 1982), representing the "best-case" scenario of the five general gyro configurations outlined in Section 12.2.2.

Dual anodes are generally incorporated as illustrated in the figure below to overcome Doppler shifts attributed to the otherwise moving medium within the laser cavity. In DC-excited plasma, the neutral atoms tend to move towards the cathode along the center of the discharge tube and towards the anode along the walls, a phenomenon known as *Langmuir flow*; the laser radiation being predominately along the tube centerline thus experiences a net motion in the medium itself (Chow, et al., 1985). The opposed dual-anode configuration introduces a reciprocity in the *Langmuir flow* which cancels the overall effect, provided the anode currents are maintained precisely equal.

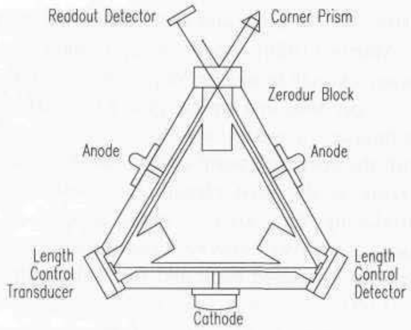

Figure 13-7. A typical three-mirror configuration of the single-axis ring-laser gyro employing dual anodes to cancel the biasing effects of induced *Langmuir flow* in the lasing medium (adapted from Udd, 1985).

The fundamental disadvantage associated with the active ring laser is a problem called *frequency lock-in*, which occurs at low rotation rates when the counter-propagating beams "lock" together in frequency (Chao, et al., 1984). This *lock-in* phenomenon is attributed to constrictions or periodic modulation of the gain medium in conjunction with the influence of a very small amount of *backscatter* from the mirror surfaces (Udd, 1985). The end result is a small deadband region (below a certain threshold of rotational velocity) for which there is no output signal as shown in Figure 13-8A. Above the lock-in threshold, output approaches the ideal linear response curve in a parabolic fashion.

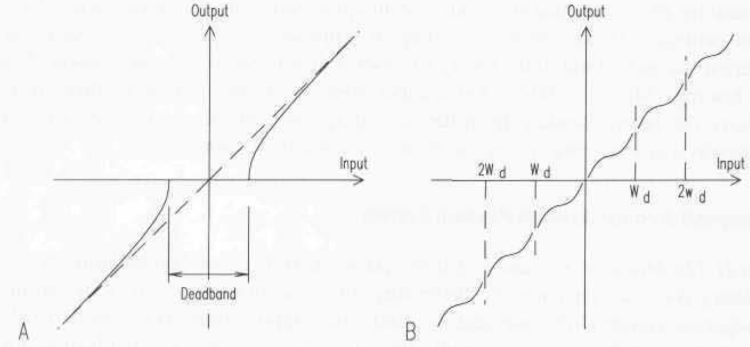

Figure 13-8. *Frequency lock-in* due to a small amount of backscatter from the mirror surfaces results in a zero-output deadband region (A) at low rotational velocities; the application of *mechanical dither* breaks the deadband region up into smaller fragments (B) that occur at input rates equal to harmonics of the dither frequency ω_d (adapted from Martin, 1986, © IEEE).

The most obvious approach to solving the *lock-in* problem is to improve the quality of the mirrors, thereby reducing the resulting *backscatter*. Again, however, perfect mirrors do not exist, and some finite amount of *backscatter* will always be present. Martin (1986) reports a representative value of 10^{-12} the power of the main beam, enough to induce *frequency lock-in* for rotational rates of several hundred degrees per hour in a typical gyro with a 20-centimeter perimeter. A more practical technique for reducing *lock-in* is to incorporate some type of biasing scheme to shift the operating point away from the deadband zone.

Mechanical dithering is the least elegant but most common and effective biasing means, introducing the obvious disadvantages of increased system complexity and reduced *mean time between failures* associated with moving parts. The entire gyro assembly is rotated back and forth about the sensing axis in an oscillatory fashion (±100 arcseconds at 400 Hz typical), with the resulting response curve shown in Figure 13-8B. State-of-the-art dithered active ring-laser gyros have a scale factor linearity that far surpasses the best mechanical gyros. Dithered biasing, unfortunately, is too slow for high-performance systems (i.e., flight control), resulting in oscillatory instabilities (Martin, 1986). Mechanical dithering can also introduce crosstalk between axes on a multi-axis system, although some of the unibody three-axis gyros employ a common dither axis to eliminate this possibility (Martin, 1986).

Buholz and Chodorow, (1967), Chesnoy (1989), Christian and Rosker (1991), as well as Dennis, et al. (1991) discuss the use of extremely short-duration laser pulses (typically 1/15 of the resonator perimeter in length) to reduce the effects of *frequency lock-in* at low rotation rates. The basic idea is to minimize the cross coupling between the two counter-propagating beams by limiting the regions in the cavity where the two pulses overlap. Wax and Chodorow (1972) report an improvement in performance of two orders of magnitude through the use of intracavity phase modulation. Other techniques based on non-linear optics have been proposed (Udd, 1985), including an approach by Litton that applies an external magnetic field to the cavity to create a directionally dependent phase shift for biasing (Martin, 1986). Yet another solution to the *lock-in* problem is to remove the lasing medium from the ring altogether, effectively forming what is known as a *passive ring resonator*, to be discussed in Section 13.2.2.

Honeywell *Modular Azimuth Position* System

The *H-726 Modular Azimuth Position System (MAPS)* developed by Honeywell's Military Avionics Division, St. Petersburg, FL, is a complete stand-alone *inertial navigation system (INS)* intended for land-based applications (Honeywell, 1992). The system can be broken down into three major subcomponents as illustrated in Figure 13-9: 1) the *Dynamic Reference Unit (DRU)*, 2) the *Control Display Unit (CDU)*, and 3) the *Vehicle Motion Sensor (VMS)*. The *DRU* consists of an *Inertial Sensor Assembly (ISA)*, an associated *Inertial Processor*, a *Navigation Processor*, interface electronics, and a low-voltage power supply. The *CDU* communicates with the *DRU* over an RS-422 datalink, providing an operator interface for mode selection, data display, and waypoint navigation. The *VMS* is essentially an incremental optical encoder that attaches to the vehicle odometer cable, providing directional information as well as 32 displacement counts per cable revolution.

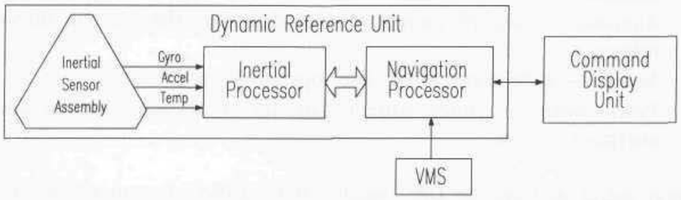

Figure 13-9. Functional block diagram of the stand-alone *H-726 Modular Azimuth Position System* (courtesy Honeywell, Inc., Military Avionics Division).

The *Inertial Sensor Assembly* is comprised of three Honeywell production-model *GG1342* ring-laser gyros and three Sundstrand *QA2000* accelerometers, mounted in a mutually orthogonal configuration as shown in Figure 13-10. The *GG1342* incorporates a three-mirror triangular lasing cavity as depicted earlier in Figure 13-7 and has a demonstrated *mean time between failure* in excess of 50,000 hours. Each of the three gyros is a completely self-contained unit including a laser block assembly, path length control transducer, readout optics, interface electronics, and mechanical dither mechanism.

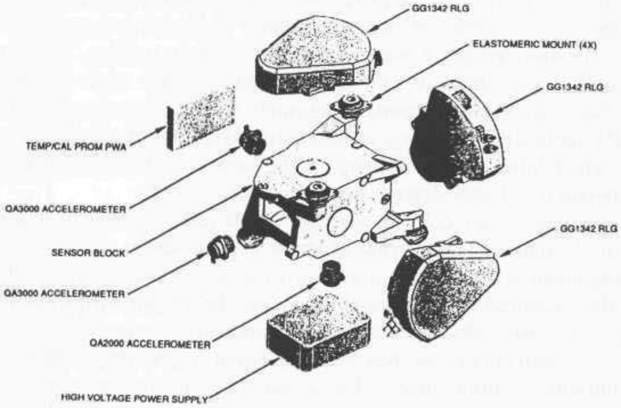

Figure 13-10. Exploded view of the *Inertial Sensor Assembly (ISA)* showing the relative orientations of the three ring-laser gyros and accelerometers (courtesy Honeywell, Inc., Military Avionics Division).

There are four basic modes of system operation:

- *Power-up* — executes a computer-controlled start-up and initialization sequence.
- *Alignment* — accepts current position data and establishes its directional reference.
- *Survey* — is the normal "run-time" operating mode.
- *Power-down* — stores current data for subsequent start-up and de-energizes system.

Upon initial start-up, the *DRU* recalls from EEPROM memory the previous location and heading of the vehicle, if available. If unknown, the current vehicle position is requested from the user in *Universal Transverse Mercator (UTM)* coordinates. A *normal alignment* can then be executed with no prior knowledge of current vehicle heading. This automatic self-alignment feature works by sensing the earth's rotation in a fashion somewhat analogous to the *north-seeking gyrocompass* previously discussed in Section 13.1.2. With the vehicle stationary, the resulting rotational components measured by the three orthogonal gyro axes can be analyzed to determine the angular orientation of the *DRU* with respect to the earth's spin axis (Huddle, 1977). The *normal alignment* process takes anywhere from 8 to 15 minutes to complete, depending on the starting latitude (Honeywell, 1992). Alternatively, a *stored heading alignment* can be performed in approximately 90 seconds using a value recalled from non-volatile memory, if the vehicle has not been moved since the DRU was last powered down.

Once initial alignment is completed, the system enters *survey mode*, ready for normal operation in either of two submodes: 1) *zero-velocity-update (ZUPT) mode* or 2) *odometer-aided mode*. The first of these options, *ZUPT mode*, is invoked only when odometry data is either not available or is of questionable validity. Sammarco (1994) reports an example of this latter situation in the case of a *MAPS* application involving autonomous navigation of a continuous mining machine, where inherent track slippage in the loose coal debris resulting from the cutting operation seriously degraded dead-reckoning results.

To re-reference under *ZUPT mode*, the vehicle must be brought to a standstill every 4 to 10 minutes for a period of about 25 seconds in order to re-establish precise alignment with the earth's axis of rotation. In addition, any differences between the measured velocity components and the known *earth-rate* values are assumed to be *DRU* velocity errors and subsequently compensated. Retroactive position-error corrections can then be made based on the perceived error vector and the duration of prior travel. The actual time interval between *ZUPTs* is a vehicle- and application-specific parameter that must be empirically determined for optimal performance (Honeywell, 1992).

In default *odometer-aided mode*, the *DRU* uses encoder-count information from the *velocity measurement system* to dampen system velocity errors as derived from the *ISA* accelerometer data. A *ZUPT* is automatically requested if a degradation is detected in dead-reckoning data (i.e., due to wheel slippage or a *VMS* component failure, for example), or if the vehicle has been in continuous motion for over an hour (Leiser, 1992). In addition, the *DRU* will continuously update its estimate of azimuth each time the vehicle stops in *odometer-aided mode* for any length of time greater than six seconds (Honeywell, 1992).

Immediately after a *ZUPT* is performed (i.e., before *DRU* velocity errors reaccumulate to any significant degree), the inertial velocity data is used to dynamically recalibrate the odometer scale factor. (Odometry calibration can change as a consequence of variations in tire pressure or vehicle loading as discussed in Chapter 2.) A 19-state *Kalman filter* in the *Navigation Processor* trims the inertial and *VMS* component coefficients during run-time operation (Leiser, 1992). Should odometer velocity not agree with the inertial measurement of velocity to within some prespecified window of acceptance, the *DRU* will set a *VMS* fault condition indicator on the *CDU* and request another *ZUPT*. The system then remains in *ZUPT mode* unless overridden by the operator.

Kearfott *Monolithic Ring-Laser Gyro*

In order to significantly reduce package size and component costs, the Kearfott Guidance and Navigation Corporation, Wayne, NJ, developed a single-block three-axis design employing only six mirrors, each mounted to the center of a cube face as shown in Figure 13-11. Within the enclosed volume of the glass-ceramic block are three mutually orthogonal and functionally independent ring-laser gyros that share a common set of mirrors. Although each mirror is used by two different gyros in the monolithic design, initial system tests in 1981 confirmed there was no interactive crosstalk between axes (Koper, 1987). The reduction in the number of required mirrors represents a considerable costs savings, in that the high-quality mirrors are one of the more costly components in an active ring-laser design. Similarly, only a single cathode and one dither mechanism are needed, instead of three each, further reducing component and assembly costs.

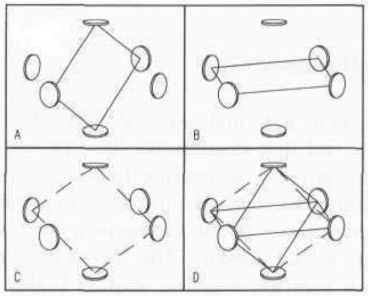

Figure 13-11. Kearfott six-mirror configuration of a three-axis ring laser gyro (adapted from Koper, 1987).

More importantly, however, the monolithic shared-mirror design optimizes the performance-to-size ratio by permitting the maximum closed-path diameter for a given volume. (Increasing the optical path length improves gyro performance, just as using a larger diameter slotted disk with more holes would increase the achievable resolution of an incremental optical encoder, to revisit the Schultz-Dubois analogy.) The medium-sized Kearfott *Monolithic Ring Laser Gyro* shown in Figure 13-12 is typically used for missile guidance and navigation; smaller low-cost units are employed in tactical weapon systems.

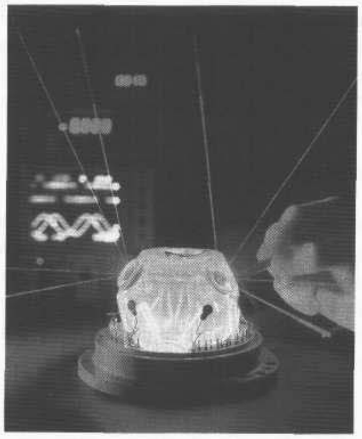

Figure 13-12. Beams of 632.8-nanometer laser light can be seen leaving the ring-laser gyro cavities through the mirrors of the compact Kearfott three-axis *Monolithic Ring-Laser Gyro*, which measures pitch, roll, and yaw in one integrated package (courtesy Kearfott Guidance and Navigation Corporation).

13.2.2 Passive Ring Resonator Gyros

The *passive ring resonator gyro* makes use of a laser source external to the ring cavity (Figure 13-13), and thus circumvents the *frequency lock-in* problem that arises when the gain medium is internal to the cavity itself. The passive configuration also eliminates problems arising from changes in the optical path length within the interferometer due to variations in the index of refraction of the gain medium (Chow, et al., 1985). The theoretical quantum noise limit is determined by *photon shot noise* and is slightly higher (i.e., worse) than the theoretical limit seen for the *active ring-laser gyro* (Ezekiel & Arditty, 1982).

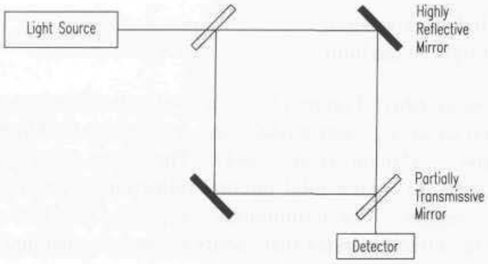

Figure 13-13. Passive ring resonator gyro with laser source external to the ring cavity (adapted with permission from Udd, 1991, © John Wiley and Sons, Inc.).

Classical implementations using mirrored optical resonators patterned after the active ring predecessors suffered from inherently bulky packaging in comparison to the newly emerging alternatives afforded by fiber-optic technology. Such fiber-optic derivatives also promised additional advantage in longer-length multiturn resonators for increased sensitivity in smaller, rugged, and less expensive packages. As a consequence, the *resonant fiber-optic gyro (RFOG)* presented later in Section 13.2.5 has emerged as the most popular of the resonator configurations (Sanders, 1992).

13.2.3 Open-Loop Interferometric Fiber-Optic Gyros

The concurrent development of optical fiber technology, spurred mainly by the communications industry, presented a potential low-cost alternative to the high-tolerance machining and clean-room assembly required for ring-laser gyros. The glass fiber in essence forms an internally reflective waveguide for optical energy, along the lines of a small-diameter linear implementation of the doughnut-shaped mirror cavity conceptualized by Schulz-DuBois (1966). The use of multiple turns of fiber means the resultant path-length change due to the Sagnac effect is essentially multiplied by a factor N equal to the integer number of turns, thereby providing significantly improved resolution (Udd, 1985). An additional advantage of the fiber-optic configuration stems from the fact that operation is not dependent on a high-finesse cavity, thereby significantly reducing manufacturing costs (Blake, et al., 1989).

Recall from Chapter 9 the *refractive index n* relates the speed of light in a particular medium to the speed of light in a vacuum as follows:

$$n = \frac{c}{c_m}$$

where:

n = refractive index of medium

c = speed of light in a vacuum
c_m = speed of light in medium.

Step-index multimode fiber (Figure 13-14) is made up of a core region of glass with index of refraction n_{co}, surrounded by a protective cladding with a lower index of refraction n_{cl} (Nolan, et al., 1991). The lower refractive index in the cladding is necessary to ensure total internal reflection of the light propagating through the core region. The terminology *step-index* refers to this "stepped" discontinuity in the refractive index that occurs at the core-cladding interface.

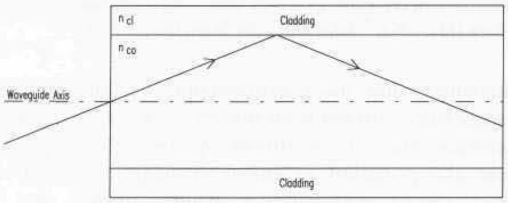

Figure 13-14. Step-index multi-mode fiber (adapted with permission from Nolan, et al., 1991, © John Wiley and Sons, Inc.).

Referring now to Figure 13-15, as long as the entry angle (with respect to the waveguide axis) of an incoming ray is less than a certain critical angle θ_c, the ray will be guided down the fiber, virtually without loss. The *numerical aperture* of the fiber quantifies this parameter of acceptance (i.e., the light-collecting ability of the fiber), and is defined as follows (Nolan, et al., 1991):

$$NA = \sin\theta_c = \sqrt{n_{co}^2 - n_{cl}^2}$$

where:

NA = numerical aperture of the fiber
θ_c = critical angle of acceptance
n_{co} = index of refraction of glass core
n_{cl} = index of refraction of cladding.

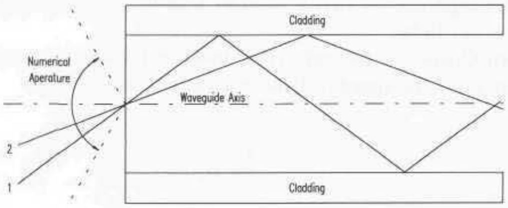

Figure 13-15. Entry angles of incoming rays 1 and 2 determine propagation paths in the fiber core (adapted with permission from Nolan, et al., 1991, © John Wiley and Sons, Inc.).

As illustrated in Figure 13-15 above, a number of rays following different-length paths can simultaneously propagate down the fiber, as long as their respective entry angles are less than the critical angle of acceptance θ_c. Multiple-path propagation of this nature occurs where the core diameter is much larger than the wavelength of the guided energy, giving rise to the term *multimode fiber*. Such multimode operation is clearly undesirable in gyro applications, where the objective is to eliminate all non-reciprocal conditions other than that imposed by the Sagnac effect itself. As the diameter of the core is reduced to approach the operating wavelength, a cutoff condition is reached where just a single mode is allowed to propagate, constrained to travel only along the waveguide axis (Nolan & Blaszyk, 1991).

Light can randomly change polarization states as it propagates through standard *single-mode fiber*. The use of special *polarization-maintaining fiber*, such as *PRSM Corning*, maintains the original polarization state of the light along the path of travel (Reunert, 1993). This is important, since light of different polarization states travels through an optical fiber at different speeds. A typical block diagram of the "minimum-reciprocal" IFOG configuration is presented in Figure 13-16. *Polarization-maintaining single-mode fiber* (Nolan & Blaszyk, 1991) is employed to ensure the two counter-propagating beams in the loop follow identical paths in the absence of rotation.

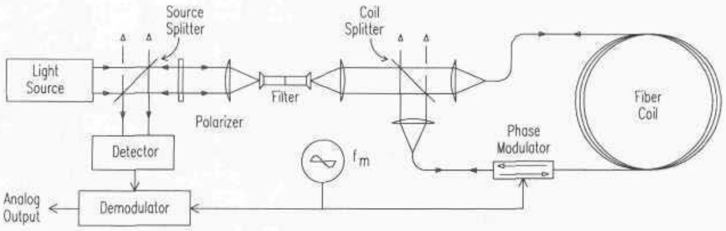

Figure 13-16. Simplified block diagram of the *minimum-reciprocal IFOG* with analog output (adapted from Ezekiel & Arditty, 1982; Lefevre, 1992).

The *Sagnac phase shift* between the two beams introduced by gyro rotation is given by (Udd, 1985):

$$Z_R = \frac{LD}{\lambda c}\Omega$$

where:

Z_R = number of fringes of phase shift due to gyro rotation
L = length of optical fiber in loop
D = diameter of loop
λ = wavelength of optical energy
c = speed of light in a vacuum
Ω = rotation rate.

The stability of the scale factor relating Z_R to Ω in the equation above is thus dependent on the stability of L, D, and λ (Ezekiel & Arditty, 1982). Practical implementations usually operate over plus or minus half a fringe (i.e., $\pm\pi$ radian of phase difference) with a theoretical sensitivity of 10^{-6} radian or less of phase shift (Lefevre, 1992). IFOG sensitivity may be improved by increasing L (i.e., adding more turns of fiber in the sensing loop), peaking at an optimal length on the order of several kilometers, after which the fiber attenuation (1 dB per kilometer typical) begins to degrade performance (Ezekiel & Arditty, 1982). This large amount of required fiber represents a rather significant percentage of overall system cost.

The two counter-propagating beams reunite at the detector, which monitors the cosinusoidal intensity changes caused by constructive and destructive interference. The peak intensity occurs as shown in Figure 13-17A at the point of zero rotation rate, where the phase shift $\Delta\phi$ between the counter-propagating beams is equal to zero. Unfortunately, there is no way to determine the direction of rotation directly from the intensity information (as can be inferred from the symmetrical nature of the plot with respect to the Y-axis), and the sensitivity of I to small changes in rotation rate is greatly reduced due to the horizontal nature of the slope (Blake, 1989).

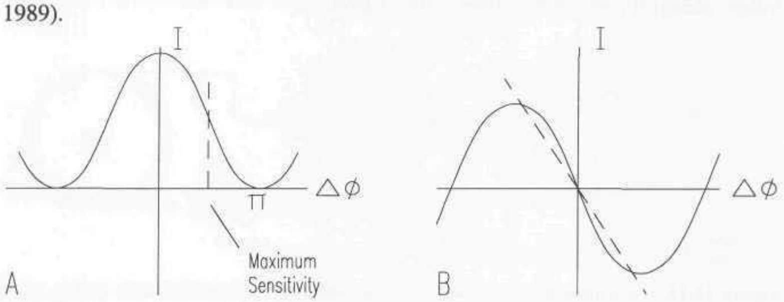

Figure 13-17. (A) Plot of detector intensity versus phase shift, and, (B) resultant demodulator output versus phase shift for the analog *open-loop IFOG* (adapted from Ezekiel & Arditty, 1982).

To overcome these deficiencies, non-reciprocal phase shifts between the two beams are introduced at an oscillatory rate ω, usually by phase modulation of the beams near one end of the interferometer coil (Udd, 1991). This phase modulation can be accomplished using a length of fiber wound around a piezoelectric cylinder and introduces a bias of $\pi/2$ to shift the operating point over into the region of maximum sensitivity on the response curve as shown in Figure 13-17A (Ezekiel & Arditty, 1982). The output of the photodetector is then synchronously demodulated and filtered to yield the sinusoidal analog representation of $\Delta\phi$ shown in Figure 13-17B. Note the direction of rotation is now easily determined from the sign of the output. Disadvantages of this open-loop approach include the non-linear relationship of the demodulated output to rotation rate Ω, and the inherent susceptibility to errors caused by variations in the light source intensity or component tolerances. As Blake (1989) points out, it is difficult to achieve good linearity in analog electronic componentry over six orders of magnitude of dynamic range.

An interesting characteristic of the *open-loop IFOG* is the absence of any narrow-band laser source (Burns, et al., 1983), the enabling technology allowing the *Sagnac effect* to reach practical implementation in the first place. A low-coherence source, such as a *superluminescent diode (SLD)*, is typically employed instead to reduce the effects of noise (Udd, 1985; Tai, et al., 1986), the primary source of which is backscattering within the fiber and at any interfaces. As a result of such backscatter, in addition to the two primary counter-propagating waves in the loop there are also a number of parasitic waves that yield secondary interferometers (Lefevre, 1992). The limited temporal coherence of the broadband SLD causes any interference due to backscattering to average to zero, suppressing the contrast of these spurious interferometers. The detection system becomes sensitive only to the interference between waves that followed identical paths (Ezekiel and Arditty, 1982; Lefevre, 1992).

The *open-loop IFOG* is attractive from the standpoint of reduced manufacturing costs, high tolerance to shock and vibration, insensitivity to gravitational effects, quick start-up, and fairly good sensitivity in terms of bias drift rate and the random walk coefficient. Coil geometry is not critical, and no path-length control is needed. Disadvantages include the long length of optical fiber required (relative to other fiber-optic gyro designs, as will be discussed later), limited dynamic range in comparison to *active ring-laser gyros*, and scale factor variations due to analog component drifts (Adrian, 1991). *Open-loop* configurations are therefore most suited to the needs of low-cost systems in applications requiring only moderate accuracy, such as gyrocompassing in automobile navigation, pitch and roll indicators, and attitude stabilization.

Hitachi Fiber-Optic Gyroscopes

Hitachi Cable, Ltd., Tokyo, Japan, offers several relatively inexpensive single-axis *open-loop IFOG* configurations intended primarily for use in automotive applications. The Hitachi *HOFG-4FT* was the original IFOG used for factory-installed vehicle navigation systems on the Toyota Mark II (a car model sold in Japan). The *HOFG-4FT* was recognized as one of the "Most Technologically Significant New Products of the Year" in 1993 by *R&D* magazine, which subsequently presented an *R&D 100* award to Hitachi. The company established a manufacturing facility in Hitachi City, Japan, with a capacity of 2,500 IFOGs per shift per month in order to meet the demands of automotive customers.

Hitachi has continued to invest in the development of lower-cost designs and manufacturing processes more in line with the needs of the automotive industry. The model *HOFG-X*, for example, is descended from the original *HOFG-4FT* design, while the *HGA-D* (Hitachi, 1994b) represents the follow-on generation of

IFOGs for in-vehicle systems. The design modifications of the *HGA-D* make it more cost effective for applications requiring serial output. Selected performance specifications are presented in Table 13-4.

Table 13-4. Selected specifications for the *HGA-D* fiber-optic gyroscope.

Parameter	Value	Units
Range	±60	degrees/second
Linearity	±2	percent scale
Random walk	1.3	degrees/√Hz
Thermal drift	±0.05	degrees/second/5°C
Update rate	10 (typical)	milliseconds
Warm up time	3 (typical)	seconds
Power	9 - 16	volts DC
	250	milliamps
Size	175 x 120 x 50	millimeters
Output	9600	baud (serial TTL)

In addition to automotive applications, Hitachi has developed IFOGs for a range of industrial and commercial uses. The *HOFG-1* has found wide employment throughout Japan in mobile robotic systems, to include industrial cleaning robots, autonomous heavy equipment, and agricultural helicopters. The system block diagram is shown in Figure 13-18. A single DB-9 connector accommodates power, reset, RS-232 serial communications, and analog output lines (Hitachi, 1994a). Selected specifications are listed in Table 13-5 below.

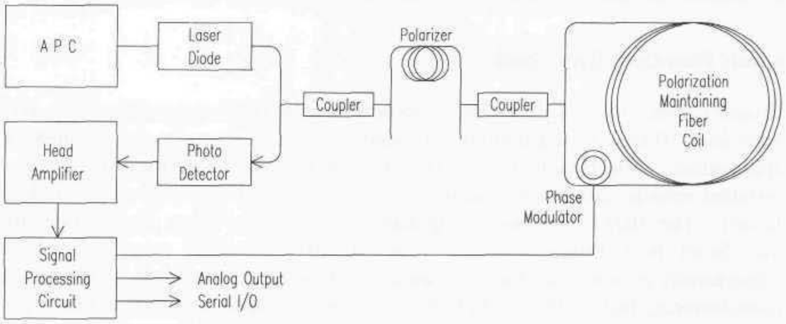

Figure 13-18. The *HOFG-1* open-loop IFOG provides a serial RS-232 as well as an analog (±2.5 volts DC) output of angle and angular rate (adapted from Hitachi, 1994a).

Table 13-5. Selected specifications for the *HOFG-1* fiber-optic gyroscope.

Parameter	Value	Units
Range	±60	degrees/second
Linearity	±1	percent scale
Random walk	<0.1	degrees/√Hz
Update rate	15 (minimum)	milliseconds
Warm up time	5 (typical)	seconds
Power	10 - 16	volts DC
	500	milliamps
Size	120 x 100 x 70	millimeters
Output	9600	baud (serial RS-232C)

13.2.4 Closed-Loop Interferometric Fiber-Optic Gyros

For applications (such as aircraft navigation) demanding higher accuracy than that afforded by the *open-loop IFOG*, the *closed-loop* configuration offers significant promise, with drifts in the 0.001 to 0.01 degree-per-hour range and scale-factor stabilities greater than 100 ppm (Adrian, 1991). Closed-loop digital signal processing is considerably more complex than the analog signal processing employed on *open-loop IFOG* configurations. Feedback into a frequency- or phase-shifting element (Figure 13-19) is employed to cancel the rotationally induced Sagnac phase shift. Since the system is always operated at a null condition where $\Delta\phi$ is equal to zero, minor variations in light-source intensity and analog component tolerances have markedly reduced effect (Ezekiel & Arditty, 1982).

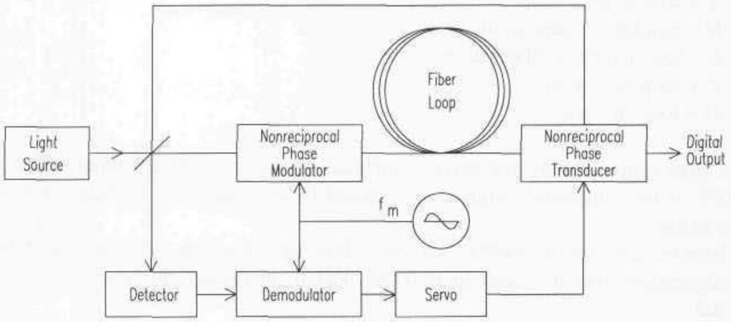

Figure 13-19. Simplified block diagram of a *closed-loop IFOG* employing a *non-reciprocal phase transducer* to null out the Sagnac phase shift $\Delta\phi$ introduced by rotation rate Ω (adapted from Ezekiel & Arditty, 1982).

Referring again to Figure 13-19, the output of the *demodulator* is passed to a servo amplifier that in turn drives a *non-reciprocal phase transducer (NRPT)*, typically an electro-optic frequency shifter placed within the fiber interferometer (Ezekiel & Arditty, 1982). The *NRPT* introduces a frequency difference between the two counter-propagating beams, resulting in an associated fringe shift at the detector given by (Udd, 1991):

$$Z_F = -\frac{\Delta f\, Ln}{c}$$

where:

Z_F = fringe shift due to frequency difference
Δf = frequency difference introduced by the *NRPT*
n = index of refraction
c = speed of light.

To null out $\Delta\phi$ at the detector, the fringe shift Z_R due to gyro rotation must be precisely offset by the fringe shift Z_F due to the relative frequency difference of the two beams:

$$\Delta\phi = Z_R + Z_F = 0\,.$$

Substituting the previous expressions for Z_F and Z_R and solving for Δf yields (Ezekiel & Arditty, 1982; Udd, 1991):

$$\Delta f = \frac{4AN}{n\lambda L}\Omega = \frac{4A}{n\lambda P}\Omega = \frac{D}{n\lambda}\Omega$$

where:

A = area of fiber loop
N = number of turns in the loop
L = total length of fiber cable
P = loop perimeter
D = loop diameter.

The gyro output, being the servo-controlled frequency shift Δf imparted by the *NRPT*, is thus inherently digital, as opposed to an analog DC voltage level, and also linear.

Ezekiel and Arditty (1982) list the following advantages of the closed-loop configuration over the open-loop IFOG design previously discussed in Section 13.2.3:

- It is independent of intensity variations in the light source, since the system is operated at null.
- It is independent of individual component gains (assuming high open-loop gain maintained).

- Linearity and stability depend only on the *non-reciprocal phase transducer*.

13.2.5 Resonant Fiber-Optic Gyros

The *resonant fiber-optic gyro (RFOG)* evolved as a solid-state derivative of the *passive ring resonator gyro* discussed in Section 13.2.2. A passive resonant cavity is formed from a multiturn closed loop of optical fiber as shown in Figure 13-20. An input coupler provides a means for injecting frequency-modulated light from a laser source into the resonant loop in both the clockwise and counterclockwise directions. As the frequency of the modulated light passes through a value such that the perimeter of the loop precisely matches an integral number of wavelengths at that frequency, input energy is strongly coupled into the loop (Sanders, 1992). In the absence of loop rotation, maximum coupling for both beam directions occurs in a sharp peak centered at this resonant frequency.

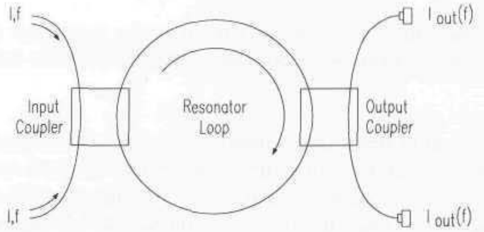

Figure 13-20. In the *resonant fiber-optic gyro (RFOG)*, maximum optical coupling into the loop occurs at that resonant frequency which yields an integral number of wavelengths corresponding to the loop perimeter (adapted from Sanders, 1992).

If the loop is caused to rotate in the clockwise direction, of course, the Sagnac effect causes the perceived loop perimeter to lengthen for the clockwise-traveling beam, and to shorten for the counterclockwise-traveling beam. The resonant frequencies must shift accordingly, and energy is subsequently coupled into the loop at two different frequencies and directions during each cycle of the sinusoidal FM sweep. An output coupler samples the intensity of the energy in the loop by passing a percentage of the two counter-rotating beams to their respective detectors as shown in the diagram. The demodulated output from these detectors will show resonance peaks as illustrated in Figure 13-21, separated by a frequency difference Δf given by the following (Sanders, 1992):

$$\Delta f = \frac{D}{\lambda n}\Omega$$

where:

Δf = frequency difference between counter-propagating beams
D = diameter of the resonant loop
Ω = rotational velocity
λ = free-space wavelength of the laser
n = refractive index of the fiber.

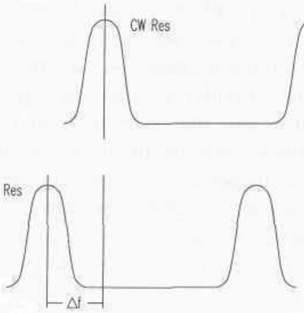

Figure 13-21. The difference (Δf) between the resonance frequencies associated with the clockwise and counterclockwise beams provides a measure of rotation rate Ω (adapted from Sanders, 1992).

In practice, the laser frequency is usually adjusted to maintain resonance in one direction, while an electro-optical frequency shifter is used to drive the other direction back into resonance. This requires a frequency shift of two times the induced Sagnac effect, since the first direction has been locked. Actual rotation rate is then determined from the magnitude of the frequency shift.

Like the IFOG, the all-solid-state RFOG is attractive from the standpoint of high reliability, long life, quick start-up, and light weight. The principle advantage of the RFOG, however, is that it requires significantly less fiber (from 10-100 times less) in the sensing coil than the IFOG configuration, while achieving the same shot-noise-limited performance (Sanders, 1992). Sanders attributes this to the fact that light traverses the sensing loop multiple times, as opposed to once in the IFOG counterpart. On the down side are the requirements for a highly coherent source and extremely low-loss fiber components (Adrian, 1991).

13.3 References

Adrian, P., "Technical Advances in Fiber-Optic Sensors: Theory and Applications," *Sensors*, pp. 23-45, September, 1991.

Arnold, R.N., Maunder, L., *Gyrodynamics and its Engineering Applications*, Academic Press, New York, NY, 1961.

Aronowitz, F., "The Ring Laser Gyro," *Laser Applications*, Vol. 1, M. Ross, ed., Academic Press, 1971.

Blake, J., Cox, J., Feth, J, Goettsche, R., "Design, Development, and Test of a 3-Inch Open Loop All Fiber Gyro," MSD-TR-89-21, 14th Biennial Guidance Test Symposium, Holloman AFB, NM, pp. 255- 266, October, 1989.

Boxenhorn, B., Dew, B., Grelff, P., "The Micromechanical Inertial Guidance System and its Application," MSD-TR-89-21, 14th Biennial Guidance Test Symposium, Holloman AFB, NM, pp. 113-131, October, 1989.

Buholz, N., Chodorow, M., "Acoustic Wave Amplitude Modulation of a Multimode Ring Laser," *IEEE Journal of Quantum Electronics*, Vol. QE-3, No. 11, pp. 454-459, November, 1967.

Burns, W.K., Chen, C.L., Moeller, R.P., "Fiber-Optic Gyroscopes with Broad-Band Sources," *IEEE Journal of Lightwave Technology*, Vol. LT-1, p. 98, 1983.

Carter, E.F., ed., *Dictionary of Inventions and Discoveries*, Crane, Russak, and Co., NY, 1966.

Chao, S., Lim, W.L., Hammond, J.A., "Lock-in Growth in a Ring Laser Gyro," Proceedings, Physics and Optical Ring Gyros Conference, SPIE Vol 487, Snowbird, UT, pp. 50-57, January, 1984.

Chesnoy, J., "Picosecond Gyrolaser," *Optics Letters*, Vol 14, No. 18, pp. 990-992, September, 1989.

Chow, W.W., Gea-Banacloche, J., Pedrotti, L.M., Sanders, V.E., Schleich, W., Scully, M.O., "The Ring Laser Gyro," *Reviews of Modern Physics*, Vol. 57, No. 1, pp. 61-104, January, 1985.

Christian, W.R., Rosker, M.J., "Picosecond Pulsed Diode Ring Laser Gyroscope," *Optics Letters*, Vol. 16, No. 20, pp. 1587-1589, October, 1991.

Cochin, I., *Analysis and Design of the Gyroscope for Inertial Guidance*, John Wiley and Sons, New York, NY, 1963.

Dahlin, T., Krantz, D., "Low-Cost, Medium Accuracy Land Navigation System," *Sensors*, pp. 26-34, February, 1988.

Dance, B., "Piezoelectric Ceramic Elements Form Compact Gyroscope," *Design News*, pp. 113-115, 20 September, 1993.

Dennis, M.L., Diels, J.M., Lai, M., "Femtosecond Ring Dye Laser: A Potential New Laser Gyro," *Optics Letters*, Vol. 16, No. 7, pp. 529-531, April 1, 1991.

Dunlap, G.D., Shufeldt, H.H., *Dutton's Navigation and Piloting*, Naval Institute Press, pp. 557-579, 1972.

Ezekiel, S., Arditty, H.J., Editors, Fiber Optic Rotation Sensors and Related Technologies, Proceedings of the First International Conference, MIT, Springer-Verlag, New York, 1982.

Fraden, J., *AIP Handbook of Modern Sensors*, Radebaugh, R., ed., American Institute of Physics, New York, 1993.

Fujishima, S., Nakamura, T., Fujimoto, K., "Piezoelectric Vibratory Gyroscope Using Flexural Vibration of a Triangular Bar," Frequency Control Symposium, 29 May, 1991.

Hine, A., *Magnetic Compasses and Magnetometers*, Adam Hilger Ltd., London, 1968.

Hitachi, "Fiber Optic Gyroscope (HOFG-1)," Specification No SP 94-28-1005, Hitachi Cable, Ltd., Tokyo, Japan, 10 August, 1994a.

Hitachi, "Fiber Optic Gyroscope (HGA-D)," Specification No SP 94-28-1006, Hitachi Cable, Ltd., Tokyo, Japan, 10 August, 1994b.

Honeywell, "H-726 Modular Azimuth Position System," Technical Description, 1192-12025, Honeywell, Inc., Military Avionics Division, St. Petersburg, FL, December, 1992.

Huddle, J.R., "The Theoretical Principles for Design of the Inertial Surveyor for Position and Gravity Determination," First International Symposium on Inertial Technology for Surveying and Geodesy, Ottawa, Ontario, Canada, 12-14 October, 1977.

Koper, J.G., "A Three-Axis Ring Laser Gyroscope," *Sensors*, pp. 8-21, March, 1987.

Lefevre, H.C., "The Interferometric Fiber-Optic Gyroscope," in *Fiber Optic Sensors*, Udd, E., ed., Vol. CR44, SPIE Optical Engineering Press, Bellingham, WA, September, 1992.

Leiser, K.E., "The Ring Laser Gyro Modular Azimuth Position System Comes of Age: First Article Test Results and Present Applications," reprinted in: *H-726 Modular Azimuth Position System*, Technical Description, 1192-12025, Honeywell, Inc., Military Avionics Division, St. Petersburg, FL, December, 1992.

Martin, G.J., "Gyroscopes May Cease Spinning," *IEEE Spectrum*, pp. 48-53, February, 1986.

Menegozzi, L.N., Lamb, W.E., "Theory of a Ring Laser," *Physical Review A*, Vol. 1, No. 4, pp. 2103-2125, October, 1973.

Mettler, E., Hadaegh, F.Y., "Space Micro-Guidance and Control: Applications and Architectures," Sensors and Sensor Systems for Guidance and Navigation II, SPIE Vol. 1694, Orlando, FL, pp. 144-158, April, 1992.

Murata, "Gyrostar Piezoelectric Vibrating Gyroscope," Product Literature, Catalog No. G-09-B, Murata Electronics North America, Inc., Smyrna, Georgia, 1994a.

Murata, "Gyrostar Piezoelectric Vibrating Gyroscope: Test and Reliability Data," Technical Manual, Catalog No. T-03-B, Murata Electronics North America, Inc., Smyrna, Georgia, 1994b.

Nakamura, T., "Vibration Gyroscope Employs Piezoelectric Vibrator," JEE, pp. 99-104, September, 1990.

Nolan, D.A., Blaszyk, P.E., Udd, E., "Optical Fibers", in *Fiber Optic Sensors: An Introduction for Engineers and Scientists*, E. Udd, ed., John Wiley, New York, pp. 9-26, 1991.

Orlosky, S.D., Morris, H.D., "A Quartz Rotational Rate Sensor," *Sensors*, pp. 27-31, February, 1995.

Reunert, M.K., "Fiber Optic Gyroscopes: Principles and Applications," *Sensors*, pp. 37-38, August, 1993.

Sagnac, G.M., "L'ether lumineux demontre par l'effet du vent relatif d'ether dans un interferometre en rotation uniforme," C.R. Academy of Science, 95, pp. 708-710, 1913.

Sammarco, J.J., "A Navigational System for Continuous Mining Machines," *Sensors*, pp. 11-17, January, 1994.

Sanders, G.A., "Critical Review of Resonator Fiber Optic Gyroscope Technology," in *Fiber Optic Sensors*, Udd, E., Editor, Vol. CR44, SPIE Optical Engineering Press, Bellingham, WA, September, 1992.

Schulz-DuBois, E.O., "Alternative Interpretation of Rotation Rate Sensing by Ring Laser," *IEEE Journal of Quantum Electronics*, Vol. QE-2, No. 8, pp. 299-305, August, 1966.

Snodgrass, R.E., *Insects: Their Ways and Means of Living*, Abbot, C.G., ed., Vol. 5 of the Smithsonian Scientific Series, Smithsonian Institution, New York, NY, 1930.

Systron Donner, "GyroChip," Product Literature, Systron Donner Inertial Division, Concord, CA, undated.

Systron Donner, "GyroChip Theory of Operation," Application Note, Systron Donner Inertial Division, Concord, CA, July, 1992.

Systron Donner, "GyroChip: Industrial Solid-State Rotation Sensor," Product Literature, Systron Donner Inertial Division, Concord, CA, February, 1994a.

Systron Donner, "GyroChip II," Product Literature, Systron Donner Inertial Division, Concord, CA, February, 1994b.

Systron Donner, "MotionPak: Solid-State 6-DOF Motion Sensor," Product Literature, Systron Donner Inertial Division, Concord, CA, June, 1994c.

Tai, S., Kojima, K., Noda, S., Kyuma, K., Hamanaka, K., Nakayama, T., "All-Fibre Gyroscope Using Depolarized Superluminescent Diode," *Electronic Letters*, Vol. 22, p. 546, 1986.

Udd, E., "Fiberoptic vs. Ring Laser Gyros: An Assessment of the Technology," in *Laser Focus/Electro Optics*, December, 1985.

Udd, E., "Fiber Optic Sensors Based on the Sagnac Interferometer and Passive Ring Resonator," in *Fiber Optic Sensors: An Introduction for Engineers and Scientists*, E. Udd, ed., John Wiley, New York, pp. 233-269, 1991.

Wax, S.I., Chodorow, M., "Phase Modulation of a Ring-Laser Gyro - Part II: Experimental Results," *IEEE Journal of Quantum Electronics*, pp. 352-361, March, 1972.

Wilkinson, J.R., "Ring Lasers," *Progress in Quantum Electronics*, Moss, T.S., Stenholm, S., Firth, W.J., Phillips, W.D., and Kaiser, W., eds., Vol. 11, No. 1, Pergamon Press, Oxford, 1987.

14

RF Position-Location Systems

RF position-location techniques can be subdivided into the two broad classes of *ground-based* systems and *satellite-based* systems. Typical non-robotic applications include marine and aircraft navigation, race car performance analysis, range instrumentation, unmanned mobile target control, mine localization, hazardous materials mapping, dredge positioning, geodetic surveys, and fleet management. Fairly low-cost localized implementation of such systems have recently found commercial application providing position location and range information for golfers (Purkey, 1994).

14.1 Ground-Based RF Systems

Ground-based RF position location systems are typically of two types: 1) *passive hyperbolic line-of-position systems* that compare the time-of-arrival phase differences of incoming signals simultaneously emitted from surveyed transmitter sites; and 2) *active radar-like trilateration systems* that measure the round-trip propagation delays for a number of fixed-reference transponders. Passive systems are generally preferable when a large number of vehicles must operate in the same local area, for obvious reasons.

14.1.1 Loran

An early example of the first category is seen in *Loran* (short for long range navigation). Developed at MIT during World War II, such systems compare the time of arrival of two identical signals broadcast simultaneously from high-power transmitters located at surveyed sites with a known separation baseline. For each finite time difference (as measured by the receiver) there is an associated hyperbolic line of position as shown in Figure 14-1. Two or more pairs of master-slave stations are required to get intersecting hyperbolic lines resulting in a two-dimensional (latitude and longitude) fix.

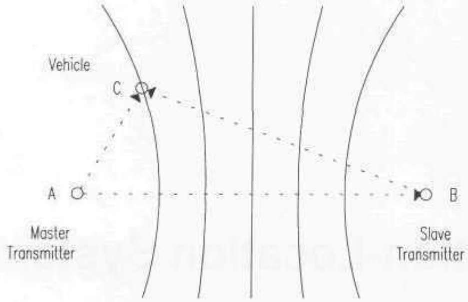

Figure 14-1. For each hyperbolic line of position, length ABC minus length AC equals some constant *K* (adapted from Dodington, 1989).

The original implementation (*Loran A*) was aimed at assisting convoys of liberty ships crossing the North Atlantic in stormy winter weather. Two 100-kilowatt slave transmitters were located about 200 miles on either side of the master station. Non-line-of-sight ground-wave propagation at around 2 MHz was employed, with pulsed as opposed to continuous-wave transmissions to aid in skywave discrimination. The time-of-arrival difference was simply measured as the lateral separation of the two pulses on an oscilloscope display, with a typical accuracy of around 1 microsecond. This numerical value was matched to the appropriate line of position on a special Loran chart of the region, and the procedure then repeated for another set of transmitters. For discrimination purposes, four different frequencies were used, 50 KHz apart, with 24 different pulse repetition rates in the neighborhood of 20 to 35 pulses per second (Dodington, 1989). In situations where the hyperbolic lines intersected more or less at right angles, the resulting (best-case) accuracy was about 1.5 kilometers.

Loran A was phased out in the early '80s in favor of *Loran C*, which achieves much longer over-the-horizon ranges through use of 5-megawatt pulses radiated from 1300-foot towers at a lower carrier frequency of 100 KHz. For improved accuracy, the phase differences of the first three cycles of the master and slave pulses are tracked by phase-lock loops in the receiver and converted to a digital readout, which is again cross-referenced to a preprinted chart. Effective operational range is about 1000 miles, with best-case accuracies in the neighborhood of 100 meters. Coverage is provided by about 50 transmitter sites to all US coastal waters and parts of the North Atlantic, North Pacific, and the Mediterranean.

14.1.2 Kaman Sciences *Radio Frequency Navigation Grid*

The Remote Control Program Group of Kaman Sciences Corporation, Colorado Springs, CO, has developed a scaled-down version of a Loran-type hyperbolic position-location system known as the *Radio Frequency Navigation Grid*

(RFNG). The original application in the late 1970s involved autonomous route control of unmanned mobile targets used in live-fire testing of the laser-guided *Copperhead* artillery round (Stokes, 1989). The various remote vehicles sense their position by measuring the phase differences in received signals from a master transmitter and two slaves situated at surveyed sites within a 100-square-kilometer area as shown in Figure 14-2. Best-case system resolution is 1.5 inches at a 20-Hz update rate, resulting in a typical positioning repeatability of ±1 meter for a 60-ton tank running at speeds up to 45 kilometers per hour.

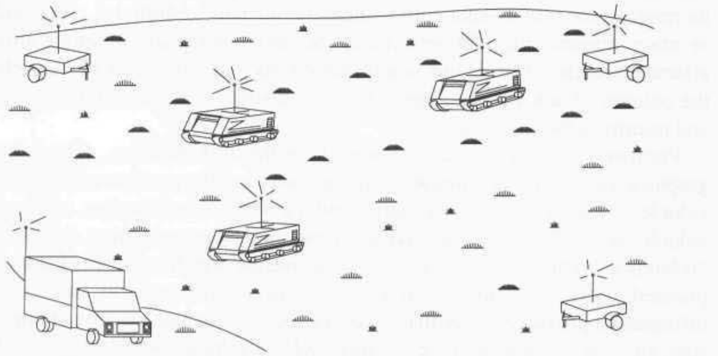

Figure 14-2. Kaman Sciences 1500-watt navigation grid is a scaled-down version of the Loran concept, covering an area 8 to 15 kilometers on a side with a position-location repeatability of ±1 meter (courtesy Kaman Sciences Corp.).

Path trajectories were originally taught by driving a vehicle over the desired route and recording the actual phase differences observed. This file was then played back at run time and compared to measured phase difference values, with vehicle steering servoed in an appropriate manner to null any observed error signal. This approach resulted in the exact replication of the recorded trail, including any changes in velocity or direction. Vehicle speeds in excess of 30 miles per hour are supported over path lengths of up to 15 kilometers (Stokes, 1989). Multiple canned paths can be stored and changed remotely, but vehicle travel must always begin from a known start point (Byrne, et al., 1992).

The *Threat Array Control and Tracking Information Center (TACTIC)* is offered by Kaman Sciences to augment the RFNG by tracking and displaying the location and orientation of up to 24 remote vehicles (Kaman, 1991). Real-time telemetry and recording of vehicle heading, position, velocity, status, and other designated parameters (i.e., fuel level, oil pressure, battery voltage) are supported at a 1-Hz update rate. The *TACTIC* operator has direct control over engine start, automatic path playback, vehicle pause/resume, and emergency halt functions. Non-line-of-sight operation is supported through use of a 23.825-MHz grid frequency in conjunction with a 72-MHz control and communications channel.

In response to requirements for column operations, an *Intelligent Collision Avoidance (ICA)* capability was added to provide automatic management of the vehicle array. The *ICA* software runs on a higher-level computer that utilizes the *TACTIC* computer to perform two-way data communication with each vehicle in the array. The *TACTIC* computer also preconditions vehicle data by computing position, speed, heading, and vehicle status for presentation to the *ICA*, which in turn computes actual vehicle spacing and location. The *ICA* module then commands (through *TACTIC*) necessary adjustments to each vehicle in order to maintain commanded column speed and vehicle spacing. Should a vehicle abort its mission for loss of data communication, off-path conditions, command abort, or other reasons, the *ICA* recognizes the abort and plans a detour around the affected vehicle. The detour is transmitted via *TACTIC* to all of the vehicles in the column. Each vehicle approaching the aborted unit then executes the detour and returns to the main trail.

Pertinent mission data are presented on the *ICA* monitor. These include a graphical display of the intended column route, and the position and status of each vehicle. Also displayed are data showing the communication status of each vehicle as well as mission elapsed time and time remaining for the chosen "reference" vehicle to reach a location of interest which could be, for example, a planned impact location. *TACTIC* logs all mission critical data as well as information provided by ancillary sensors such as exhaust gas temperature, engine rpm, etc. Other features of the enhanced *RFNG* vehicle control system include:

- Expanded operating area (100-plus square kilometers).
- Operation of vehicles from a remote location (i.e., *ICA* is used at range control centers 25 or more miles from the vehicle array).
- Remote turn on/off of grid stations where commercial power is available.
- Mission programming without having to drive the vehicle over the desired mission profile.
- Ability to operate vehicles with manual clutch and shift type transmissions.

14.1.3 Precision Technology Tracking and Telemetry System

Precision Technology, Inc., of Downsview, Ontario, has recently introduced to the automotive racing world an interesting variation of conventional phase-shift measurement approaches to position location. The company's *Precision Location* tracking and telemetry system employs a number of receive-only antennae situated at fixed locations around a racetrack to monitor a continuous sine wave transmission from a moving vehicle (Figure 14-3). By comparing the signals received by the various antennae to a common reference signal of identical frequency generated at the base station, relative changes in vehicle position with respect to each antenna can be inferred from resulting shifts in the respective phase relationships.

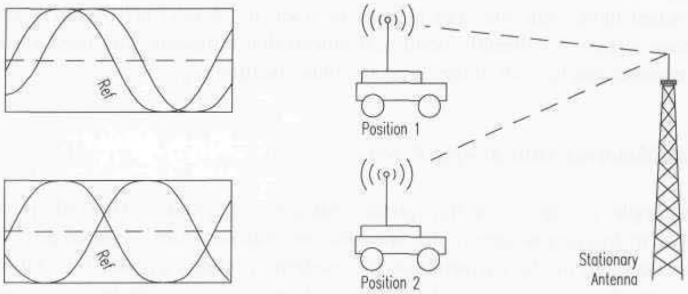

Figure 14-3. Changes in the phase relationship between the received signal and a reference sine wave generated by the base station are used to track relative movement of a race car with respect to the known location of the antenna (adapted from Duchnowski, 1992).

The system update rate for acquiring phase data from each antenna is 100 Hz. The default reporting of vehicle *X-Y* coordinate data is 10 Hz, but this information can be derived from the stored phase data if necessary at any desired sample rate up to 100 Hz. The inherent drift in the vehicle's oscillator with respect to the reference oscillator shows up in the phase data as identical offsets in the distance of the car from each of the three antennae (Figure 14-4). Although this relative bias does not affect the least-squares position determination, the accumulating drift will eventually lead to numbers that become too big for the double-precision calculations to handle. The software therefore subtracts an equivalent amount of perceived offset from each measurement to keep the numbers small.

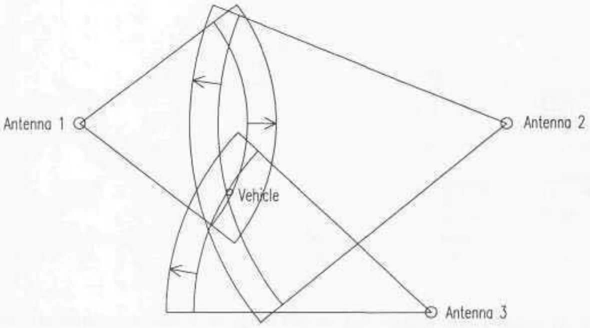

Figure 14-4. Oscillator drift will appear to increase (or decrease) the radii from all antennae by the same amount; the software minimizes the least-squares distance from the solution point to the three range arcs (courtesy Precision Technology, Inc.).

The 40.58-MHz VHF signal allows for non-line-of-sight operation to the moving vehicle, with a resulting precision of approximately 1 to 10 centimeters (Duchnowski, 1992). From a robotics perspective, problems with this approach arise when more than one vehicle must be tracked. A next-generation *Precision Location* system is currently being introduced that eliminates the need for hard-wire connections to each of the three antennae locations.

14.1.4 Motorola *Mini-Ranger Falcon*

An example of the active-transponder category of ground-based RF position-location techniques is seen in the *Mini-Ranger Falcon* series of range positioning systems offered by the Government and Systems Technology Group of Motorola, Inc., Scottsdale, AZ. The *Falcon 484* configuration depicted in Figure 14-5 is capable of measuring line-of-sight distances from 100 meters out to 75 kilometers. An initial calibration is performed at a known location to determine the turn-around delay (TAD) for each transponder (i.e., the time required to transmit a response back to the interrogator after receipt of interrogation). The actual distance between the interrogator and a given transponder is found by (Byrne, et al., 1992):

$$D = \frac{(T_e - T_d)\,c}{2}$$

where:

D = separation distance
T_e = total elapsed time
$\mathrm{T_d}$ = transponder turn-around delay
c = speed of light.

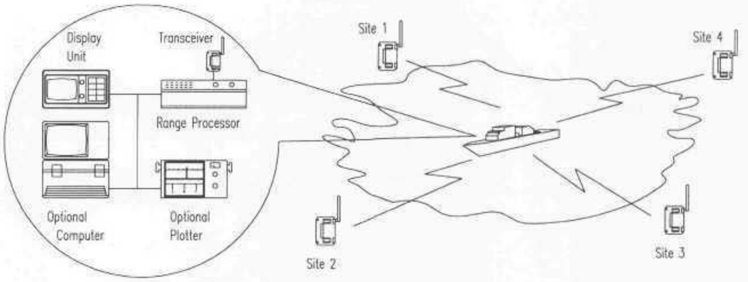

Figure 14-5. Motorola's *Mini-Ranger Falcon 484* RF position location system provides ±2 meters accuracy over ranges of 100 meters to 75 kilometers (courtesy Motorola, Inc.).

The *MC6809*-based range processor performs a least-squares position solution at a 1-Hz update rate, using range inputs from two, three, or four of 16 possible reference transponders. The individual reference stations answer only to uniquely coded interrogations and operate in C-band (5410-5890 MHz) to avoid interference from popular X-band marine radars (Motorola, undated). Up to 20 mobile users can time share the *Falcon 484* system (50 milliseconds/user maximum). System resolution is in tenths of units (meters, feet, or yards) with a range accuracy of ±2 meters probable. Power requirements for the fixed-location reference stations are 22 to 32 volts DC at 13 watts nominal, 8.5 watts standby, while the mobile range processor and its associated transmitter/receiver and display unit draw 150 watts at 22 to 32 volts DC.

14.1.5 Harris *Infogeometric* System

Harris Technologies, Inc., (HTI), Clifton, VA, is developing a ground-based RF position-location and communications strategy wherein moderately priced *infogeometric (IG)* devices cooperatively form self-organizing instrumentation and communication networks (Harris, 1994). Precision position location on the move is based on high-speed range trilateration from fixed reference devices. Each *IG* device in the network has full awareness of the identity, location, and orientation of all other *IG* devices (Figure 14-6), and can communicate in both party-line and point-to-point communication modes.

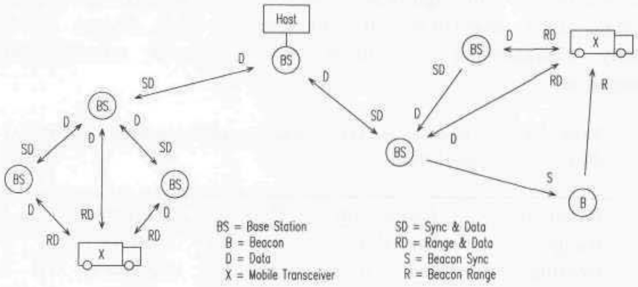

Figure 14-6. A self-organizing *infogeometric* network provides precision position location of multiple platforms through high-speed range trilateration to fixed-location *base stations* and *beacons* (courtesy Harris Technologies, Inc.).

The *IG* devices employ digital *code-division-multiple-access (CDMA)* spread-spectrum RF hardware that can provide the following functional capabilities:

- Network-level mutual autocalibration.
- Associative location and orientation tracking.
- Party-line and point-to-point data communications (with video and audio options).
- Distributed sensor data fusion.

To improve accuracy over alternative range-lateration schemes, the HTI system incorporates mutual data communications, permitting each mobile user access to the time-tagged range measurements made by fixed reference devices and all other mobile users. This additional network-level range and timing information permits more accurate time synchronization among device clocks, and automatic detection and compensation for uncalibrated hardware delays. Each omnidirectional CDMA spread-spectrum "geometric" transmission uniquely identifies the identity, location, and orientation of the transmitting source. Typically the available geometric measurement update rate is in excess of 1 MHz. Tracking and communications at operating ranges of up to 20 kilometers are supported by transmission power levels of 1 to 3 watts. Typical "raw data" measurement resolution and accuracies are cited in Table 14-1 below.

Table 14-1. Raw data measurement resolution and accuracy.

Parameter	Resolution	Biasing	Dimension
Range	1	5	meters
Bearing (Az, El)	2	2	degrees
Orientation (Az)	2	2	degrees

Enhanced tracking accuracies for selected applications can be provided as cited in Table 14-2 below. This significant improvement in performance is provided by *sensor data-fusion algorithms* that exploit the high degree of relational redundancy characteristic of infogeometric network measurements and communications.

Table 14-2. Enhanced tracking resolution and accuracies obtained through sensor data fusion.

Parameter	Resolution	Biasing	Dimension
Range	0.1 - 0.3	0.1 - 0.3	meters
Bearing	0.5 - 1.0	0.5 - 1.0	degrees
Orientation	0.5 - 1.0	0.5 - 1.0	degrees

These *data-fusion algorithms* also provide the following additional capabilities:

- Enhanced tracking in multipath and clutter, permitting precision robotic tracking even when operating indoors.
- Enhanced near/far interference reduction, for shared-spectrum operations in potentially large user networks (i.e., hundreds to thousands).

Distributed *IG* networks support precision tracking, communications, and command and control among a wide variety of potential user devices. No absolute surveyed or known location references are needed when a number of mobile units are interacting on a purely relational basis. When operating within an absolute coordinate frame as is typically the case with most semi-structured robotic applications, only a few surveyed reference locations are required.

Prototype 902- to 928-MHz FCC-compatible *infogeometric transceivers* developed for the MDARS Exterior program were field-tested in October 1994 over distances of 6 to 8 kilometers, using 1-watt transmitters equipped with 3-dB omni-directional antennae. Kinematic tracking tests under typical multipath conditions showed repeatedly achievable resolutions of 10 to 30 centimeters RMS in range, and 1 to 2 degrees RMS in bearing. The nominal communication data rate of 64 kilobits per second can be increased if necessary with a subsequent reduction in detection range and signal jamming resistance. Similarly, the 10-Hz position-update rate required by the MDARS performance specification can be increased at the expense of slightly reduced tracking resolution.

14.2 Satellite-Based Systems

14.2.1 Transit Satellite Navigation System

The Transit satellite navigation system was developed by the US Navy to provide accurate worldwide position location for ballistic missile submarines (Stansell, 1971). The first Transit satellite was launched in 1959; the system became operational in 1964 and was declassified and made available in 1967 for commercial maritime usage. By 1990, seven satellites were on line in polar orbits, accompanied by six spares (Getting, 1993).

The principle of operation for Transit is based on the observed Doppler shift of a stable CW transmitter on board a satellite as it passes through its *closest point of approach* (CPA) to the receiver. (This effect was first noticed by Navy researchers at the Applied Research Laboratory run by Johns Hopkins University, while closely monitoring the transmitter on the Soviet Sputnik 1.) The slope of the resultant Doppler frequency curve is directly related to the radial component of relative velocity, and thus indicative of the slant range from receiver (assumed to be at sea level) to satellite.

In other words, if the receiver is located in the plane of the orbit, the radial velocity component will be maximized, and slant range at CPA will be equal to the satellite altitude directly overhead. As the receiver moves away from a position directly below the orbital path (Figure 14-7), the radial component of relative velocity falls off while the tangential component increases. The overall effect shows up as a decrease in the slope of the curve representing the received Doppler frequency as a function of time during satellite passage (Figure 14-8). Based on the measured value of the slope, the actual slant range from the receiver to the known satellite position (as transmitted by the satellite) at CPA can be derived from precalculated tables. This slant range offset establishes one of two required position coordinates, while the actual time of closest approach provides the other coordinate.

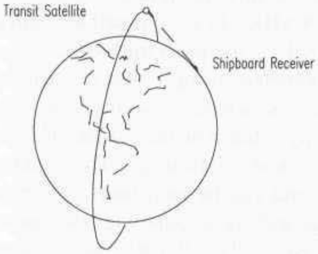

Figure 14-7. Radial component of relative velocity decreases for receiver locations further away from the orbital plane of the satellite (adapted from Dodington, 1989).

In actuality, not one but two separate CW transmissions are broadcast at 150 and 400 MHz. This technique allows the receiver to estimate the propagation delay introduced by the free-electron density of the ionosphere, based on the measured difference in time of arrival of the two signals (Getting, 1993). The Transit satellites circle the globe every hour and 45 minutes in fairly low (600 mile) polar orbits, and may be in view for as long as 20 minutes, during which time repetitive fixes can be taken every 30 seconds. Minor deviations in satellite trajectory caused by air friction and variations in the earth's magnetic field are tracked by ground stations, with updated positional information passed to the satellites for global rebroadcast. The *circular error probable* (CEP) for a single fix can approach 50 to 200 meters for a receiver mounted on a slowly moving platform with known course and speed (Dodington, 1989). For fixed-location receivers, higher accuracies approaching a few meters are possible by averaging the readings over a long period of time (Getting, 1993). In fact, before being abandoned by geodesists in favor of GPS (Section 14.2.2), Transit was providing sub-meter accuracies in certain structured scenarios.

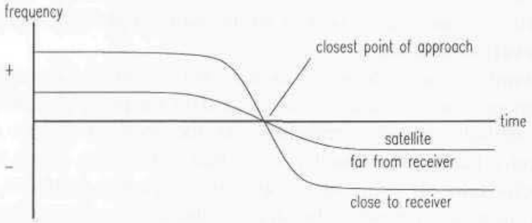

Figure 14-8. Slope of the Doppler frequency shift at time of passage is indirectly related to the slant range between receiver and satellite (Dodington, 1989).

14.2.2 Navstar Global Positioning System

The more recent *Navstar global positioning system (GPS)* developed as a Joint Services Program by the Department of Defense uses a constellation of 24 satellites orbiting the earth every 12 hours at an altitude of about 10,900 nautical miles. Four satellites are located in each of six planes inclined 55 degrees with respect to the plane of the earth's equator (Getting, 1993). The absolute three-dimensional location of any GPS receiver is determined through *trilateration* techniques based on time of flight for uniquely coded *spread-spectrum* radio signals transmitted by the satellites. Precisely measured signal propagation times are converted to *pseudoranges* representing the line-of-sight distances between the receiver and a number of reference satellites in known orbital positions. The measured distances have to be adjusted for receiver clock offset, as will be discussed later, hence the term *pseudoranges*. Knowing the exact distance from the ground receiver to three satellites theoretically allows for calculation of receiver latitude, longitude, and altitude.

Although conceptually rather simple (see Hurn (1993) for an introductory overview), this design philosophy introduces at least four obvious technical challenges:

- Time synchronization between individual satellites and GPS receivers.
- Precise real-time location of satellite position.
- Accurate measurement of signal propagation time.
- Sufficient signal-to-noise ratio for reliable operation in the presence of interference and possible jamming.

A less obvious challenge arises from the fact that, according to Einstein's theory of general relativity, time appears to run slower near a massive body like the earth than at higher altitudes. If not taken into proper consideration, this rather intriguing phenomenon can lead to position errors on the order of miles (Hawking, 1990). Having introduced this particular issue for sake of awareness, I must now defer further discussion as beyond the scope of this chapter.

The first of the previously mentioned problems is addressed through the use of sophisticated atomic clocks (relying on the vibration period of the cesium atom as a time reference) on each of the satellites to generate time ticks at a frequency of 10.23 MHz. (The Block II satellites actually carry two cesium and two rubidium atomic clocks). Each satellite transmits a periodic pseudo-random code on two different L-band frequencies (designated *L1* and *L2*) using *spread-spectrum* techniques in the internationally assigned navigational frequency band. The *L1* and *L2* frequencies of 1575.42 and 1227.6 MHz are generated by multiplying the cesium-clock time ticks by 154 and 128, respectively. The individual satellite clocks are monitored by dedicated ground tracking stations operated by the US Air Force and continuously advised of their measured offsets from official GPS time. (GPS time is kept by a virtual master clock devised through a combination of clocks at the tracking station and the individual satellites.) High precision in this regard is critical since electromagnetic radiation travels at the speed of light, roughly 1 foot per nanosecond.

There are two possible methods that can be used to establish the exact time required for signal propagation, both necessitating careful phase comparison between satellite-transmitted and locally generated waveforms. The signals involved can be: 1) the *L1* or *L2* carrier frequencies themselves or 2) the pseudo-random code modulated onto the carrier frequencies. This section will address only this second option, referred to as *code-phase tracking*, which was the original intended mode of operation for GPS. The subsequently developed and more accurate *carrier-phase tracking* approach, used primarily for static surveying applications (and more recently mobile scenarios as well), will be discussed in a later section.

In the more conventional *code-phase tracking* scheme, an identical pseudocode sequence is generated in the GPS receiver on the ground and compared to the received code from the satellite. The locally generated code is shifted in time during this comparison process until maximum correlation is observed, at which point the induced delay represents the time of arrival as measured by the receiver's clock. The problem then becomes establishing the relationship between the atomic clock on the satellite and the inexpensive quartz-crystal clock employed in the GPS receiver. Deriving this ΔT is accomplished by measuring the range to a fourth satellite, resulting in four independent trilateration equations with four unknowns (i.e., X, Y, Z, and ΔT). Details of the mathematics involved are presented by Langley (1991).

As was the case with the Transit system, precise real-time location of satellite position is determined by a number of widely distributed tracking and telemetry stations at surveyed locations around the world. Referring to Figure 14-9, all measured and received data are forwarded to a master station for analysis and referenced to GPS time. Change orders and signal-coding corrections are generated by the master station and then sent to the satellite control facilities for uploading (Getting, 1993). In this fashion the satellites are continuously advised of their current position as perceived by the earth-based tracking stations, and encode this *ephemeris* information into their *L1* and *L2* transmissions to the GPS receivers. (*Ephemeris* is the space vehicle orbit characteristics, a set of numbers that precisely describe the vehicle's orbit when entered into a specific group of equations.)

GPS time is measured in terms of 1.5-second *epochs* generated by the atomic clocks aboard the various satellites, which are maintained in effective synchronization by uplinked corrections as measured by the Control Segment. These individualized timing correction offsets are included in the navigation messages transmitted by the satellites to user receivers on the ground. The *time of week (TOW)* is defined as the number of elapsed *epochs* since the beginning of the week. The *Z-count* is a 29-bit binary number, where the 10 most-significant digits represent the GPS week number, and the 19 least-significant digits portray the current *time of week* (Mathers, 1994).

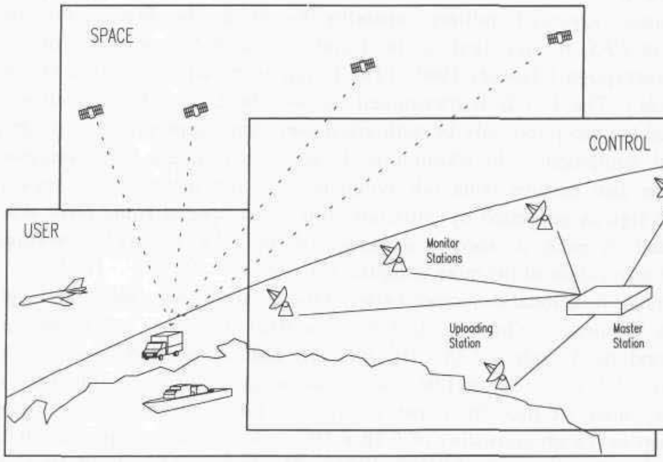

Figure 14-9. The Navstar Global Positioning System consists of three fundamental segments: Space, Control, and User (adapted from Getting, 1993, © IEEE).

In addition to its own timing offset and orbital information, each space vehicle transmits data on all other satellites in the constellation to enable any ground receiver to build up an *almanac* after a "cold start." Diagnostic information with respect to the status of certain onboard systems and expected range-measurement accuracy is also included. This collective "housekeeping" *NAV message* is superimposed on both the *L1* and *L2* signals through modulo-two addition to the pseudo-random code modulation at a very low (50-bits/second) data rate, and requires 12.5 minutes for complete downloading (Ellowitz, 1992). Timing offset and *ephemeris* information are repeated at 30-second intervals during this procedure to facilitate initial pseudorange measurements.

To further complicate matters, the sheer length of the unique pseudocode segment assigned to each individual Navstar satellite (i.e., around 6.2 trillion bits) for repetitive transmission can potentially cause initial synchronization by the ground receiver to take considerable time. For this and other reasons, each satellite broadcasts two different non-interfering pseudocodes. The first of these is called the *coarse acquisition*, or *C/A-code*, and is transmitted on the *L1* frequency to assist in acquisition. There are 1023 different *C/A-codes*, each having 1023 chips (code bits) repeated 1000 times a second (Getting, 1993) for an effective chip rate of 1.023 MHz (i.e., one-tenth the cesium clock rate). Each satellite has its own individual *C/A-code* assignment so as to enable unique identification by the ground receivers. While the *C/A-code* alone can be employed by civilian users to obtain a fix, the resultant positional accuracy is somewhat degraded due to the long chip wavelength of 300 meters. This public-usage satellite navigation service is formally referred to as *Standard Positioning Service*, or *SPS*.

The more advanced military capability known as the *Precise Positioning Service*, or *PPS*, is supported by the *Y-code,* formerly the *precision* or *P-code* prior to encryption 1 January 1994. (The *Y-code* is in fact a scrambled version of the *P-code*.) The *Y-code* is transmitted on both the *L1* and *L2* frequencies and scrambled for reception only by authorized users with appropriate cryptographic keys and equipment. In addition to limiting user access, this *antispoofing* encryption also ensures bona fide recipients will not inadvertently track false GPS-like signals generated by unfriendly forces. A special *Hand-Over-Word* is transmitted in each six-second subframe of the C/A-code *NAV message* to facilitate acquisition of the more complex Y-Code.

The major functional difference between the Y- and C/A-codes is the length of the code segment. While the C/A-code is 1023 bits long and repeats every millisecond, the Y-code is 2.35 x 10^{14} bits long and requires 266 days to complete (Ellowitz, 1992). Each satellite uses a one-week segment of this total code sequence; there are thus 36 unique Y-codes (31 for satellites and five spares for other purposes) each consisting of 6.18 x 10^{12} code bits set to repeat at midnight on Saturday of each week (ARINC, 1991). The higher chip rate of 10.23 MHz (equal to the cesium clock rate) in the precision Y-code results in a chip wavelength of 30 meters for the Y-code as compared to 300 meters for the C/A-code (Ellowitz, 1992), and thus facilitates slightly more precise time-of-arrival measurement for military purposes. For a more detailed treatment of the C/A- and Y-code signal structures, see Spilker (1978).

Brown and Hwang (1992) discuss a number of potential pseudorange error sources as summarized in Table 14-3. Positional uncertainties related to the space vehicles are clearly a factor, introducing as much as 3 meters standard deviation in pseudorange measurement accuracy. As the radiated signal propagates downward towards the earth, varying atmospheric effects introduce an uncertainty in the actual time of arrival due to changes to the speed of signal propagation. Recall from Chapter 9 that the speed of light *c* is only constant in a vacuum and slows in other media by a factor known as the *index of refraction n*:

$$c_m = \frac{c}{n}.$$

Electrons are liberated from the atoms found in various ionospheric gases by the ultraviolet light from the sun, thus contributing to the free-electron density, which in turn directly influences the value of *n* as given in the equation presented earlier in Chapter 9:

$$n = 1 + \frac{N q_e^2}{2 \varepsilon_o m \omega^2}$$

where:

N = number of charges per unit volume
q_e = charge of an electron
ε_o = permittivity of free space
m = mass of an electron
ω = frequency of the electromagnetic radiation

For free electrons, $\omega_0 = 0$ as there is no elastic restoring force (Feynman, et al., 1963).

In other words, the higher the free-electron density of the ionosphere, the more charges per unit volume (N), and the greater the subsequent slowing effect on signal propagation speed c_m. For this reason the mean *ionospheric group delay* during the day (around 50 nanoseconds) is much worse than at night (around 10 nanoseconds) when solar activity is greatly reduced (Spilker, 1978). Ionospheric effects are also very much a function of satellite elevation angle, which determines the length of the signal path through the region of influence, with the shortest possible path of course resulting when the satellite is directly overhead. At low elevation angles the above delays can easily triple (Spilker, 1978). Notice, however, the inverse square dependence on frequency ω in the above equation. This relationship can be exploited by PPS users to dynamically determine the *ionospheric group delay* effects through use of dual-frequency transmissions (i.e., *L1* and *L2*), resulting in two independent equations involving the same satellite (and therefore the same propagation path).

Tropospheric group delays caused by water vapor and other atmospheric constituents, on the other hand, are basically independent of frequency, and more pronounced due to the higher air density. Fortunately, however, tropospheric effects are fairly easy to model based on local barometric pressure, temperature, and humidity measurements (Spilker, 1978). Due to the more immediate proximity of the troposphere (9-16 kilometers) relative to the receiver, the group delay effects are even more dependent on satellite elevation than that associated with ionospheric delays as discussed above. This dependence increases exponentially below elevation angles of 15 degrees due to the stronger concentration of water vapor at altitudes below 12 kilometers (Lachapelle, et al., 1987). Local variations in the moisture content of the troposphere cause problems in eliminating this particular error component through differential-GPS techniques, as will be discussed later in this chapter.

Multipath reflections (i.e., from clouds, land masses, water surfaces) can increase the perceived time of flight beyond that associated with the optimal straight-line path (Figure 14-10). In general, the problem is much worse for marine applications than land-based scenarios, due to the higher reflectivity of water, and also more serious for low satellite elevation angles. The pseudo-random code-modulation scheme employed in the C/A- and Y-code signals inherently rejects signals outside of one chip-size of the direct pseudorange, effectively bounding the maximum possible multipath pseudorange error to 293.2 and 29.3 meters, respectively (Lachapelle, et al., 1987).

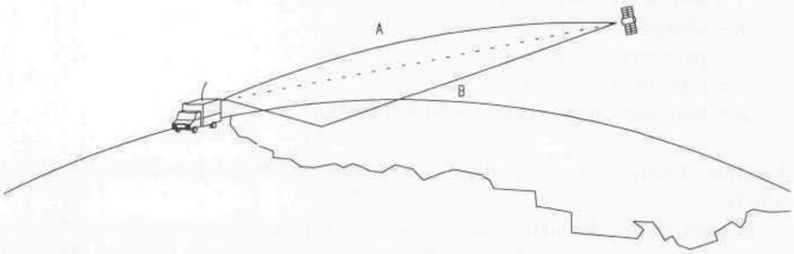

Figure 14-10. Atmospheric refraction (A) and multipath reflections (B) contribute to pseudorange measurement errors, especially at low satellite elevation angles.

In addition to the aforementioned atmospheric effects, small errors in timing and satellite position have been deliberately introduced into the C/A- and P-codes by the master station to prevent a hostile nation from using GPS in support of precision weapons delivery. This intentional degradation in SPS positional accuracy to around 100 meters (2drms) best-case is termed *selective availability (S/A)* (Gothard, 1993). *Selective availability* has been continuously in effect (with a few exceptions) since the end of Operation Desert Storm. The level of induced error was set to zero during the Persian Gulf War from August 1990 until July 1991 to improve the accuracy of commercial hand-held GPS receivers used by coalition ground forces.

There are two aspects of *selective availability*: *epsilon* and *dither*. *Epsilon* is intentional error in the superimposed navigation message regarding the exact location (*ephemeris*) of the satellite, whereas *dither* is induced error in the satellite clock that creates uncertainty in the time-stamped data. Encrypted correction parameters are incorporated into the Y-Code to allow authorized PPS users to remove the effects of both *epsilon* and *dither*. Some SPS receivers (for example, the Trimble *Ensign*) employ running-average filtering to statistically reduce the *epsilon* error over time (typically hours) to a reported value of 15 meters *spherical error probable (SEP)*.

Additional errors can be attributed to group delay uncertainties introduced by the processing and passage of the signal through the satellite electronics. Receiver noise and resolution must also be taken into account. Motazed (1993) reports fairly significant differences of ±0.02 to ±0.07 arcminutes in calculated latitudes and longitudes for two identical C/A-code receivers placed side by side. And finally, the particular dynamics of the mobile vehicle that hosts the GPS receiver plays a noteworthy role, in that best-case conditions are associated with a static platform, and any substantial velocity and acceleration will adversely affect the solution.

Table 14-3. Summary of potential error sources for measured pseudoranges (adapted with permission from Brown & Hwang, 1992, © John Wiley and Sons, Inc.).

Error Source	Standard Deviation	Units
Satellite position	3	meters
Ionospheric effects	5	meters
Tropospheric effects	2	meters
Multipath reflection	5	meters
Selective Availability	30	meters

All of the error sources listed in Table 14-3 are further influenced by the particular geometry of the four reference satellites at time of sighting. Ignoring time synchronization needs for the moment (i.e., three versus four satellites required), the most accurate three-dimensional trilateration solutions will result when the bearing or sight lines extending from the receiver to the respective satellites are mutually orthogonal. If the satellites are spaced closely together in a tight cluster or otherwise arranged in a more or less collinear fashion with respect to the receiver as shown in Figure 14-11, the desired orthogonality is lost and the solution degrades accordingly. This error multiplier, which can range from acceptable values of two or three all the way to infinity, is termed *geometric dilution of precision* (Byrne, et al., 1993).

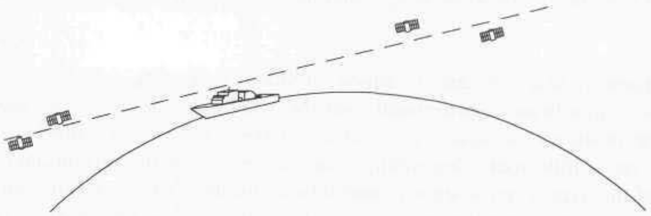

Figure 14-11. Worst case *geometric dilution of precision (GDOP)* errors occur when the receiver and satellites approach a collinear configuration as shown.

Kihara and Okada (1984) mathematically show where the minimum achievable (best-case) value for GDOP is 1.5811 and occurs when the four required GPS satellites are symmetrically located with an angle of 109.47 degrees between adjacent bearing lines as shown in Figure 14-12. In reality (since this criteria places three of the satellites just below the horizon), optimal performance is seen with three satellites equally spaced just above the horizon and one directly overhead.

Overall SPS accuracy can be significantly enhanced when combined with information from other navigational sensors, such as odometry, magnetic compasses, rate gyros, and inclinometers. For example Zexel Corporation, Farmington Hills, MI, has developed an integrated system for Oldsmobile that uses vehicle displacement information from a car's electronic speedometer, in addition to azimuthal information from the Murata piezoelectric gyro (Chapter 13), to augment the solution from a Rockwell GPS receiver (Schofield, 1994). A street-map database supplied by Navigation Technologies Corporation of Sunnyvale, CA, is employed to generate a CRT map display for the driver, with computer-synthesized speech output to advise of upcoming turns and landmarks (Lyons, 1994). The Zexel satellite navigation package was introduced as an option in Avis rental cars in the state of California in late 1994, with coast-to-coast availability expected to follow in 1995 as the associated map databases are tested and debugged.

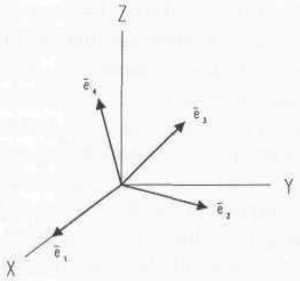

Figure 14-12. *GDOP* error contribution is minimal for four GPS satellites symmetrically situated with respect to the receiver (at origin) along bearing lines 109.47 degrees apart (Kihara & Okada, 1984).

Advertised accuracy of this combined GPS/dead-reckoning system is around 10 meters, a significant improvement over the 100 meters best case for unaided SPS. The positional accuracy needs of an exterior autonomous mobile robot, however, are a little more demanding than can be met with conventional SPS systems of this type, even when augmented by additional dead-reckoning sensors. Accordingly, most system designers are relying instead on an enhanced variation known as *differential GPS (DGPS).* With the exception of multipath (and to a certain extent tropospheric delays), the collective effects of all the error sources depicted in Table 14-3 can be essentially eliminated through use of this practice, the topic of our next section.

Code-Phase Differential GPS

The *differential GPS* concept is based on the premise that a second GPS receiver in fairly close proximity (i.e., within several tens of kilometers) to the first will experience basically the same error effects when viewing identical reference satellites, since the satellites are so far away in comparison to the receiver separation baseline. If this second receiver is fixed at a precisely surveyed location (Figure 14-13), its calculated solution can be compared to the known position to generate a composite error vector representative of prevailing conditions in that immediate locale. This differential correction can then be passed to the first receiver to null out the unwanted effects, effectively reducing position error for commercial systems to well under 10 meters. Hurn (1994) presents a concise and easy to read introduction to the basic fundamentals of DGPS. The terminology *kinematic DGPS* is often used to describe situations where the first receiver is mobile, (i.e., moving in real time), as would be the case in any robotics application.

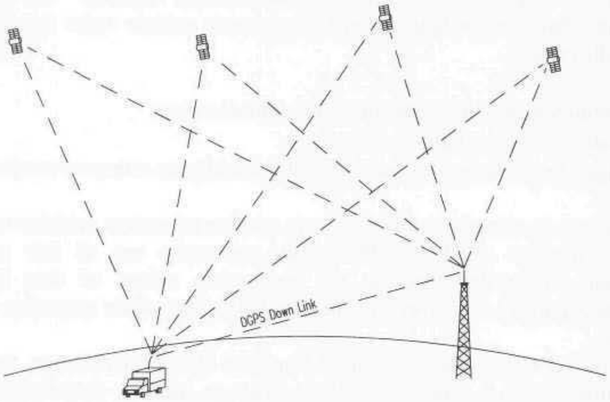

Figure 14-13. A differential GPS receiver placed at a surveyed reference site can be used to relay real-time corrections over an RF downlink to the DGPS-equipped vehicle.

In actuality, there are a number of ways this DGPS concept can be implemented, based on whether the corrections are made in the measurement domain or the solution domain, and the types of datalink employed (Blackwell, 1985). From a robotics perspective, only those procedures which make the upgraded solution available at the mobile-platform end of the datalink are of interest, thus narrowing the possibilities down to two candidate techniques. The general scenario described in the preceding paragraph, where the fixed reference receiver calculates a position correction vector, requires the following information be uplinked from the base station to the mobile unit (Blackwell, 1985):

- ΔX, ΔY, and ΔZ corrections for each user's set of satellites.
- Rate of change of above corrections
- Age of ephemeris data (each satellite) used by the base station.
- Address of the mobile platform.

The fundamental drawback to this approach is the ambiguity associated with which four satellites are used to generate the position solution. If any of the potentially numerous mobile receivers select a dissimilar combination from the available satellites in view than was selected by the reference station receiver, the differential corrections are no longer valid. Since most modern multichannel receivers employ dynamic algorithms for optimal satellite selection, this satellite coordination disconnect presents a real problem.

Accordingly, most equipment vendors have elected to support an alternative method wherein corrections are made in the measurement domain (i.e., to the pseudoranges themselves). The reference receiver basically knows where the satellites are supposed to be and how long the signal propagation should take, and compares this expected transit time to that actually required. The necessary information that must be transferred to the remote vehicle under this scheme is (Blackwell, 1985):

- Pseudorange corrections for each satellite in view.
- Rate of change of above corrections
- Age of ephemeris data (each satellite) used by the reference receiver.

This approach is advantageous in that any number of remote vehicles within the coverage envelope of the DGPS uplink can make use of this correction information simply by choosing the appropriate subset of data (i.e., that corresponding to the four specific satellites selected by their respective onboard receivers).

The fixed DGPS reference station transmits these pseudorange corrections several times a minute (depending on the data rate, message format, and number of satellites in view) to any differential-capable receiver within range. For example, a *Type 1* message format (see Table 14-4) with four satellites in view results in an average transmission rate of once every seven seconds, while 18 seconds would be required with 11 satellites in view (Mathers, 1994). The pseudorange correction is passed to the remote platform in the form of a first-order polynomial (RTCM, 1994):

$$PRC(t) = PRC(t_o) + RRC * [t - t_o]$$

where:

$PRC(t)$ = pseudorange correction at time t
$PRC(t_o)$ = correction at modified Z-count reference time t_o
RRC = range rate correction.

This correction is simply added to the appropriate pseudorange as measured by the mobile receiver:

$$PR(t) = PRM(t) + PRC(t)$$

where:

$PR(t)$ = differentially corrected measurement for time t
$PRM(t)$ = pseudorange measured by mobile receiver at time t.

Many commercial GPS receivers are available with differential capability, and most now follow the *RTCM SC-104* standard developed by the Radio Technical Commission for Maritime Services (Special Committee 104) to promote interoperability. Version 2.1 of this standard now identifies 26 formal message types (Table 14-4), each consisting of a variable number of 30-bit words (RTCM, 1994). The first two words in each message type form the message header consisting of: 1) a preamble (a fixed sequence of binary digits), 2) the message type, 3) the reference station identifier, 4) the modified Z count, 5) a sequence number that increments with each message, 6) the message length (number of words), and 7) the reference station health code (Mathers, 1994). Only the first 24 bits of each word are used for data, with the last 6 bits reserved for parity check.

Table 14-4. Format for the first 21 of 26 identified RTCM SC-104 message types; only seven are defined, nine reserved with form and content to be specified later, and the rest are undefined (Langley, 1994).

Type	Status	Explanation
1	Fixed	Differential GPS Corrections
2	Fixed	Delta Differential GPS Corrections
3	Fixed	Reference Station Parameters
4	Retired	Surveying
5	Tentative	Constellation Health
6	Fixed	Null Frame
7	Fixed	Beacon Almanacs
8	Tentative	Pseudolite Almanacs
9	Fixed	Partial Satellite Set Differential Corrections
10	Reserved	P(Y)-Code Differential Corrections (all)
11	Reserved	C/A-Code L1 and L2 Delta Corrections
12	Reserved	Pseudolite Station Parameters
13	Tentative	Ground Transmitter Parameters
14	Reserved	Surveying Auxiliary Message
15	Reserved	Ionosphere (Troposphere) Message
16	Fixed	Special Message
17	Tentative	Ephemeris Almanac
18	Tentative	Uncorrected Carrier Phase Measurements
19	Tentative	Uncorrected Pseudorange Measurements
20	Tentative	RTK Carrier Phase Corrections
21	Tentative	RTK Pseudorange Corrections

In addition to the more common C/A-code implementations, differential systems can also utilize the higher-resolution Y-code (see message Type 10 in Table 14-4) for even better accuracies. With *antispoofing* now in effect, however, only authorized PPS users are able to access the L2 signal, and so Y-code-DGPS systems have not been perceived as viable products by the vendor community. Prices for DGPS-capable mobile receivers run about $2K, while the reference stations cost somewhere between $10K and $20K. Magnavox is working with CUE Network Corporation (one of several companies providing DGPS correction services) to market a nationwide network to pass differential corrections over an FM link to paid subscribers (GPS Report, 1992).

Typical code-phase DGPS accuracies are around 2 to 4 meters SEP, with better performance seen as the baseline distance between the mobile unit and the fixed reference station is decreased, and the sophistication of receiver hardware and software improves with time. Many receiver manufacturers "smooth" the pseudorange measurements with the carrier, thus eliminating some of the inherent noise for improved performance (McPherson, 1991). The Coast Guard is in the process of implementing *differential GPS* in all major US harbors, with an expected accuracy of around 1 meter SEP (Getting, 1993). A differential GPS system already in operation at O'Hare International Airport in Chicago has demonstrated that aircraft and service vehicles can be located to 1 meter (Hambly, 1992). Surveyors have used differential GPS to achieve centimeter accuracy for years, but this practice involves *carrier-phase tracking* versus *code-phase tracking* (see next section), and until recently required long static dwell times plus significant postprocessing of the collected data (Byrne, 1993).

An interesting variant of kinematic DGPS is reported by Motazed (1993) in conjunction with the *Non-Line-of-Sight Leader/Follower (NLOSLF)* program underway at RedZone Robotics, Inc., Pittsburgh, PA. The NLOSLF operational scenario involves a number of vehicles in a convoy configuration that autonomously follow a lead vehicle driven by a human operator, both on-road and off-road at varying speeds and separation distances. A technique Motazed refers to as *intermittent stationary base differential GPS* is used to provide global referencing for purposes of bounding the errors of a sophisticated Kalman-filter-based GPS/INS position estimation system.

Under this innovative concept, the lead and final vehicle in the convoy alternate as fixed DGPS reference stations. As the convoy moves out from a known location, the final vehicle remains behind to provide differential corrections to the GPS receivers in the rest of the vehicles. After traversing a predetermined distance in this fashion, the convoy is halted and the lead vehicle assumes the role of differential reference station, providing enhanced accuracy to the trailing vehicle as it catches up to the pack. During this time, the lead vehicle takes advantage of on-site dwell to further improve the accuracy of its own fix. Once the last vehicle joins up with the rest, the base-station roles are reversed again, and the convoy resumes transit in "inchworm" fashion along its intended route. Disadvantages to this approach (from a robotics perspective) include the need for intermittent stops, and the accumulating ambiguity in the actual location of the appointed reference station.

Omnitech Robotics, Inc. of Englewood, CO, has developed an integrated vehicle position and orientation (pose) estimation subsystem called *COMPASS (compact outdoor multipurpose pose assessment sensing system)*. Shown in Figure 14-14, *COMPASS* uses a sophisticated suite of position and orientation sensors fused into a single statistically optimal pose estimate using Kalman filter techniques:

- Differential GPS.
- 3-axis inertial-grade accelerometers.
- 3-axis angular rate gyroscopes.
- Barometric altimeter.
- 2-axis fluxgate magnetometer.
- Optical encoder wheel odometry.
- 2-axis inclinometer.
- Magnetic landmark acquisition.

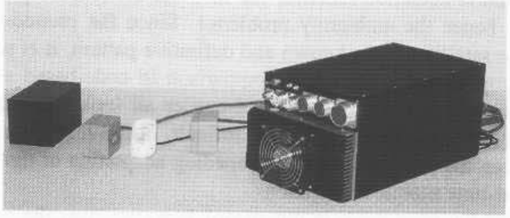

Figure 14-14. Omnitech's *COMPASS* is a commercially available navigational subsystem that uses a Kalman filter approach for fusing data from a magnetic compass, rate gyros, accelerometers, vehicle odometry, and differential GPS (courtesy Omnitech Robotics, Inc.).

The vehicle odometry and inertial navigation systems provide fast analog sensing of position, velocity, angular rate, and orientation, allowing *COMPASS* to provide three-dimensional pose information at a 32-Hz rate. The C/A-code-based DGPS and magnetic landmark sensors supply lower-update absolute position information to constrain the error accumulation to an accuracy of 10 centimeters (1-sigma 2D); in open areas where less accuracy is required, the magnetic landmarks can be omitted with a resulting accuracy of 1 meter. An optional *carrier-phase DGPS capability* (see next section) is available upon request.

Carrier-Phase Differential GPS

As previously mentioned, surveyors use a technique known as *carrier-phase differential*, also referred to (perhaps incorrectly) as *codeless differential*, to achieve improved accuracy over *code-phase differential* schemes. The L1 carrier phase is normally measured using the C/A-code, and therefore is not "codeless." The L2 phase, however, now that the P-code has been encrypted, is measured using "codeless" techniques as follows.

Recall the *Y-code* chip rate is directly equal to the satellite cesium clock rate, or 10.23 MHz. Since the L1 carrier frequency of 1575.42 MHz is generated by multiplying the clock output by 154, there are consequently 154 carrier cycles for every *Y-code* chip. This implies even higher measurement precision is possible if time-of-arrival is somehow referenced to the carrier instead of the pseudocode itself. In other words, while the *Y-code* chip wavelength is 30 meters, the L1 carrier wavelength is only 19 centimeters. Codeless interferometric differential GPS schemes can measure the phase of this carrier signal to within ±2 millimeters, and subsequently achieve 2- to 5-centimeter accuracies, but must start at a known geodetic location and typically require dwell times of several seconds or more (McPherson, 1991).

This on-station dwell time is required at start-up to resolve the unknown integer number of whole carrier cycles making up the pseudorange. (Recall from Chapter 6 that phase-detection schemes can measure the relative phase shift over only one cycle, hence the ambiguity problem.) Since the pseudo-random code generated by the satellites has a known and definitive pattern, it is relatively easy to establish a precise index for phase comparison in code-based systems. The individual cycles that make up the L-band carrier all look just alike, however, making initial synchronization much more difficult. Resolving cycle ambiguity in real time has been the principle problem impeding adaptation of the carrier-phase technique to real-time mobile applications.

Much progress has been made in this regard, however, over the past few years. The Army's Engineer Topographic Laboratories is in the process of developing a real-time *carrier-phase-differential* system that is expected to provide 1- to 3-centimeter accuracy (SEP) at a 60-Hz rate when finished sometime in 1996 (McPherson, 1991). Driven by a number of perceived application areas (i.e., automated agriculture, fleet management, robotics), many other developmental organizations and GPS equipment vendors are also pursuing viable solutions with encouraging results. The off-the-shelf Trimble *MARS* system claims a 2- to 10-centimeter real-time kinematic accuracy at slow speeds typical of the MDARS Exterior robot (i.e., less than 15 kilometers per hour). NovAtel has developed a similar system with a kinematic accuracy of less than 20 centimeters, while Premier GPS reportedly achieves 2-centimeter accuracy using proprietary software in conjunction with any of several commercially available GPS cards.

The significant engineering challenge remaining in this rapidly evolving arena is reliable avoidance, identification, and correction of *cycle slips*. A *cycle slip* is defined as a sudden gain or loss of some integer number of cycles due to receiver dynamics or the temporary occlusion of a satellite (Bock, et al., 1985). Increasing the receiver tracking bandwidth can reduce the occurrence of the former, but with an associated degradation in solution accuracy (Wong, et al., 1988). If the number of *cycle-slip-free* satellites in view ever falls below four, a new static initialization sequence must be performed to eliminate the resulting phase ambiguities (Cannon & Lachapelle, 1992). Modern receivers are addressing this vulnerability through the use of redundant satellite channels, and higher-precision C/A-code phase correlation to minimize the ambiguity interval in the first place, thus facilitating faster recovery.

GPS Summary

Conley (1993) presents an excellent assessment of stand-alone (i.e., non-differential) GPS performance and reliability with an emphasis on Control and Space Segment factors. A reasonable extraction from the open literature of achievable position accuracies for the various GPS configurations is depicted in Table 14-5. As in the case of the earlier Transit system, the Y-code has dual-frequency estimation for atmospheric refraction, and no *selective availability* error component, so accuracies are better than stand-alone single-frequency C/A-code systems. Commercial DGPS accuracy, however, exceeds stand-alone military Y-code accuracy, particularly for small-area applications such as airports. Differential Y-code is currently under consideration and may involve the use of a geosynchronous satellite to disseminate the corrections over a wide area, but the imposed *anti-spoofing* measure seriously restricts availability to potential users. Carrier-phase differential is more likely to surface as the prime contender for high-accuracy kinematic navigational systems, with several prototypes already up and running.

Table 14-5. Summary of achievable position accuracies for various implementations of GPS.

GPS Implementation Method	Position Accuracy
C/A-Code Stand Alone	100 meters 2drms
Y-Code Stand Alone	16 meters SEP
Differential C/A-Code	1 meter SEP
Differential Y-Code	TBD
Phase Differential (Codeless)	1 centimeter SEP

In summary, the fundamental problems associated with using GPS for mobile robot navigation are as follows:

- Periodic signal blockage due to foliage, structures, and hilly terrain.
- Multipath interference due to reflective structures, water, and land masses.
- Insufficient positional accuracy in stand-alone and code-phase differential mode.
- Cycle slips in carrier-phase differential mode.

GPS World provides a comprehensive listing of receiver equipment in each January issue, while Byrne, et al. (1993) present a detailed evaluation of performance for five popular models (Magnavox *6400*, Magnavox *GPS Engine*, Magellan *GPS Module*, Rockwell *NavCore V*, and Trimble *Pacer*) operating in single-point stand-alone mode. McLellan and Battie (1994) present a similar evaluation for several differential-capable receivers (Motorola *PVT6*, Magnavox *GPS Engine*, Rockwell *NavCore V*, Trimble *SVeeSix Plus*, and the Magellan *GPS Module*) operating in both static and kinematic stand-alone and differential modes.

In addition, the University of New Brunswick maintains an Internet-accessible archive of GPS information, to include receiver reviews and user feedback, in the form of the *Canadian Space Geodesy Forum (CANSPACE)*. Electronic mail messages pertaining to news, comments, questions, and answers are regularly exchanged among forum participants on topics such as Navstar GPS, Glonass, Transit, very long baseline interferometry, satellite laser ranging, etc. Although initially intended to link Canadian geodesists and geophysicists together, this valuable resource is now open to the public with a World Wide Web Universal Resource Locator of "http://www.unb.ca/Geodesy/ index.html". For more information, contact the University of New Brunswick at *lang@unb.ca*. (See Appendix.)

With a wide variety of envisioned high-volume applications and intense competition amongst a proliferation of vendors, the cost of differential GPS systems will continue to fall while reliability and accuracy further improve. Although (with the exception of Oldsmobile) the US automotive industry is taking a rather cautious wait-and-see approach, an estimated 25,000 GPS systems are sold by six major car makers in Japan each month (Berg, 1994). The Coast Guard intends to have its harbor-approach DGPS coverage completed by 1996, and the US Army Corps of Engineers is planning similar installations for the country's major navigable rivers. The FAA, meanwhile, has initiated efforts investigating the applicability of DGPS for precision aircraft approach systems at commercial airports. It seems very likely from this gathering momentum that carrier-phase DGPS, augmented by additional dead-reckoning sensors, will be the navigation system of choice for exterior robotic applications over the coming decade.

14.3 References

ARINC, "GPS NAVSTAR Global Positioning System User's Overview," Technical Report YEE-82-009D, ARINC Research Corporation, Under Contract F09603-89-G-0054/0006 to NAVSTAR GPS Joint Program Office, Los Angeles, CA, March, 1991.

Arradondo-Perry, J., "GPS World Receiver Survey," *GPS World*, pp. 46-58, January, 1992.

Berg, P., "Meanwhile, Most US Automakers are Sitting on the Fence," *Car and Driver*, pp. 113-115, May, 1994.

Blackwell, E.G., "Overview of Differential GPS Methods," Navigation: Journal of the Institute of Navigation, Vol. 32, No. 2., pp. 114-125, Summer, 1985.

Bock, Y., Abbot, R.I., Counselman, C.C., Gourevitch, S.A., King, R.W., "Establishment of Three-Dimensional Geodetic Control by Interferometry with the Global Positioning System," *Journal of Geophysical Research*, Vol. 90, No. B9, pp. 7689-7703, August, 1985.

Brown, R.G., Hwang, P.Y.C., Introduction to Random Signals and Applied Kalman Filtering, 2nd ed., New York, NY, John Wiley and Sons, p. 420, 1992.

Byrne, R.H., Klarer, P.R., Pletta, J.B., "Techniques for Autonomous Navigation," Sandia Report SAND92-0457, Sandia National Laboratories, Albuquerque, NM, March, 1992.

Byrne, R.H., "Global Positioning System Receiver Evaluation Results," Sandia Report SAND93-0827, Sandia National Laboratories, Albuquerque, NM, September, 1993.

Cannon, M.E., Lachapelle, G., "Analysis of a High-Performance C/A-Code GPS Receiver in Kinematic Mode," *Navigation: Journal of the Institute of Navigation*, Vol. 39, No. 3, pp. 285-300, Fall, 1992.

Conley, R. "GPS Performance: What is Normal?" Navigation: Journal of the Institute of Navigation, Vol. 40, No. 3, pp. 261-281, Fall, 1993.

Dodington, S.H., "Electronic Navigation Systems," *Electronic Engineer's Handbook,* D. Christiansen and D. Fink, eds., 3rd edition, New York, McGraw Hill, pp. 76-95, 1989.

Duchnowski, L.J., "Vehicle and Driver Analysis with Real-Time Precision Location Techniques," *Sensors*, pp. 40-47, May, 1992.

Ellowitz, H.I., "The Global Positioning System," *Microwave Journal*, pp. 24-33, April, 1992.

Feynman, R.P., Leighton, R.B., Sands, M., *The Feynman Lectures on Physics*, Vol. 1, Addison-Wesley, Reading, MA, 1963.

Getting, I.A., "The Global Positioning System," *IEEE Spectrum,* pp. 36-47, December, 1993.

Gothard, B.M., Etersky, R.D., Ewing, R.E., "Lessons Learned on a Low-Cost Global Navigation System for the Surrogate Semi-Autonomous Vehicle," Proceedings, SPIE Vol. 2058, Mobile Robots VIII, pp. 258-269, 1993.

GPS Report, Phillips Business Information, Potomac, MD, November, 1992.

Hambly, R.M., Chicago O'Hare International Airport Differential GNSS Trials for Airport Surface Surveillance," IEEE/AiAA 11th Digital Avionics Systems Conference, 92CH3212-8, Seattle, WA, October, 1992.

Harris, J.C., "An Infogeometric Approach to Telerobotics," Proceedings, IEEE National Telesystems Conference, San Diego, CA, pp. 153-156, May, 1994.

Hawking, S. W., *A Brief History of Time*, Bantam Books, New York, June, 1990.

Hurn, J., *GPS, A Guide to the Next Utility*, No. 16778, Trimble Navigation, Sunnyvale, CA, November, 1993.

Hurn, J., "Differential GPS Explained," No. 23036, Trimble Navigation, Sunnyvale, CA, July, 1994.

Kaman, "Threat Array Control and Tracking Information Center, Product Literature, PM1691, Kaman Sciences Corp., Colorado Springs, CO, 1991.

Kihara, M., Okada, T., "A Satellite Selection Method and Accuracy for the Global Positioning System," *Navigation: Journal of the Institute of Navigation*, Vol. 31, No. 1, pp. 8-20, Spring, 1984.

Lachapelle, G., Casey, M., Eaton, R.M., Kleusberg, A., Tranquilla, J., Wells, D., "GPS Marine Kinematic Positioning Accuracy and Reliability," *The Canadian Surveyor*, Vol. 41, No. 2, pp. 143-172, Summer, 1987.

Langley, R.B., "The Mathematics of GPS," *GPS World*, pp. 45-49, July/August, 1991.

Langley, R.B., "RTCM SC-104 DGPS Standards," *GPS World*, pp. 48-53, May, 1994.

Lyons, P., "The GPS Olds: Miss Daisy Moves to the Front Seat," *Car and Driver*, pp. 112-113, May, 1994.

Mathers, B.H., "Differential GPS Theory and Operation," Naval Command Control and Ocean Surveillance Center, San Diego, CA, July, 1994.

McLellan, J.F., Battie, J.P., "Testing and Analysis of OEM GPS Sensor Boards for AVL Applications," IEEE Position, Location, and Navigation Symposium, PLANS'94, Las Vegas, NV, April, 1994.

McPherson, J.A., "Engineering and Design Applications of Differential Global Position System (DGPS) for Hydrographic Survey and Dredge Positioning," US Army Corps of Engineers, Washington, DC, Engineering Technical Letter No. 1110-1-150, 1 July, 1991.

Motazed, B., "Measure of the Accuracy of Navigational Sensors for Autonomous Path Tracking," Proceedings, SPIE Vol. 2058, Mobile Robots VIII, pp. 240-249, 1993.

Motorola, Mini-Ranger Falcon, Product Literature, Motoroloa Government and Systems Technology Group, Scottsdale, AZ, undated.

Purkey, M., "On Target," *Golf Magazine*, pp. 120-121, May, 1994.

RTCM, "RTCM Recommended Standards for Differential NavStar GPS Service, Version 2.1," Radio Technical Commission for Maritime Services, Special Committee No. 104, January, 1994.

Schofield, J.A., "Sensors Keep Cars Purring," *Design News*, pp. 133-135, 10 October, 1994.

Spilker, J. J., Jr., "GPS Signal Structure and Performance Characteristics," *Navigation: Journal of the Institute of Navigation*, Vol. 25, No. 2, pp. 121-146, Summer, 1978.

Stansell, T., "The Navy Navigational Satellite System," *Navigation: Journal of the Institute of Navigation*, Vol. 18, No. 1, Spring, 1971.

Stokes, K.W., "Remote Control Target Vehicles for Operational Testing," Association for Unmanned Vehicles Symposium, July, 1989.

Wong, R.V.C., Schwarz, K.P., Cannon, M.E., "High-Accuracy Kinematic Positioning by GPS-INS," *Navigation: Journal of the Institute of Navigation*, Vol. 35, No. 2, pp. 275-287, Summer, 1988.

15

Ultrasonic and Optical Position-Location Systems

15.1 Ultrasonic Position-Location Systems

Ultrasonic trilateration schemes offer a medium- to high-accuracy, low-cost solution to the position location problem for mobile robots operating in relatively small work envelopes, assuming no significant obstructions are present to interfere with wave propagation. The advantages of a system of this type fall off rapidly, however, in large multiroom facilities due to the significant complexity associated with installing multiple networked beacons throughout the operating area.

Two general implementations exist: 1) a single transducer transmitting from the robot, with multiple fixed-location receivers and 2) a single receiver listening on the robot, with multiple fixed transmitters serving as beacons. The first of these categories is probably better suited to applications involving only one or at most a very small number of robots, whereas the latter case is basically unaffected by the number of passive receiver platforms involved (i.e., somewhat analogous to the *Navstar GPS* concept). Both trilateration methods will be discussed in Section 15.1.1.

An alternative ultrasonic position location scheme involves first digitizing the operating area and building a reference database of range signatures as seen by a circular ring of range sensors on the robot. This database can later be searched for an appropriate match with current sensor readings to establish the absolute position of the platform. The advantage of this approach is that no expensive beacon installations or other alterations to the environment are required, but the tradeoffs are reduced accuracy and slower update rates. This *signature-matching* technique will be discussed in Section 15.1.2.

15.1.1 Ultrasonic Transponder Trilateration

An early absolute position-location concept considered towards the end of development on ROBART I (recall the robot had no dead-reckoning capability) was an ultrasonic transponder network consisting of a master receiver unit on the robot, with three or more slaved transmitters situated around the room in known locations. The master would trigger the remote slaves via a short-range RF link, whereupon each would emit a burst of ultrasonic energy. The slaves were theoretically assigned individual operating frequencies to make them uniquely identifiable. The robot's ultrasonic receiver would begin listening for the incoming signals, timing their individual arrivals with respect to the RF trigger signal. The software could then determine the robot's position through simple trilateration.

It was further reasoned that if the master unit were equipped with two separate receiver transducers at a known orientation and lateral separation, the robot's heading could be established as well. In practice, however, a number of engineering issues come into play to complicate matters. In addition to obvious errors resulting from variations in the speed of sound, there is the inherent uncertainty associated with the finite size of the transducers themselves. For example, the original (and only) Polaroid electrostatic transducer available at that time was a full 2 inches in diameter, which differs substantially from an idealized point source or receiver. The measurement uncertainty resulting from transducer width is aggravated in this particular application by the need for wide-angle coverage, resulting in off-axis operation (i.e., the transducers are not always directly facing each other). Ranging errors induced in transmitter/receiver pairs (Figure 15-1) due to angular misalignment between transducers is extensively treated by Lamancusa and Figueroa (1990).

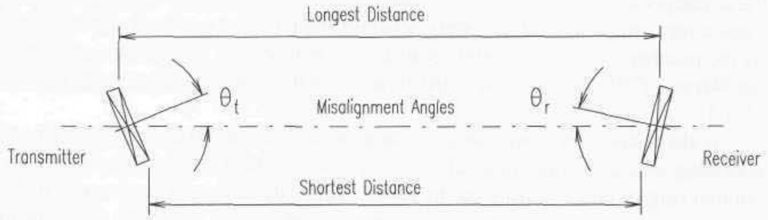

Figure 15-1. Misalignment in opposed transmitter/receiver pairs introduces a range measurement uncertainty due to the finite width of the transducers (adapted from Lamancusa and Figueroa, 1990).

On first glance it would appear that the linear relationship between effective beamwidth and transducer diameter (see Chapter 8) is advantageous in this situation, in that the necessary wide-angle coverage can be achieved in concert with an equally desirable reduction in the finite size of the sensor element.

Unfortunately, overall sensitivity falls off rapidly with any decrease in transducer diameter, significantly limiting the effective volume of coverage. An alternative strategy to achieve an omni-directional receive capability would be to employ an array of outward-facing receiver elements, monitor all transducers in the array for waveform detection, and then take into account the precise location of the actual transducer that first received the incoming acoustic wave. This approach, however, is a little less than elegant from the standpoint of increased complexity and doesn't really eliminate the range measurement errors associated with off-normal transducer alignment. IS Robotics (ISR, 1994) rather painlessly achieves the same results by situating an upward-looking sensor directly beneath a cone-shaped reflector, as will be discussed later.

I briefly toyed around at one point with the idea of using a high-voltage spark gap (Figure 15-2) as an omni-directional emitter on the robot, having read somewhere a large ultrasonic noise component could be generated in such a fashion. This approach would theoretically reduce range measurement uncertainties by more closely emulating a point source, with omni-directional propagation away from the robot to peripherally located receiver elements aimed towards the operating area. The capacitive-discharge spark generators I considered at the time, however, were even less attractive in terms of complexity, power consumption, and potential interference with other electronics, so this concept was never actually reduced to practice.

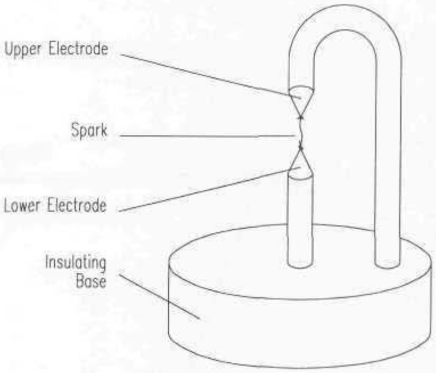

Figure 15-2. Conceptual omni-directional spark-gap emitter considered for use as an approximated point source in an ultrasonic position-location system for ROBART I.

To investigate feasibility of the ultrasonic master/slave position-location concept for possible use on ROBART II, Dunkin (1985) built and evaluated a prototype device as part of his thesis work at the Naval Postgraduate School in Monterey, CA. Although three slave units are needed for an unambiguous general solution in two dimensions, Dunkin showed a working system required only two slaves if certain conditions were taken into account. The equations describing the coordinates of the intersections of the two range arcs reduce to a pair of quadratics of the form:

$$A x^2 + B x + C = 0.$$

By solving for all known solutions, the robot's position can be determined by comparing the set of possible solutions with the estimated position, or by using various restrictions. For example, in the setup of Figure 15-3, the solution is constrained to only the positive quadrant of the Cartesian coordinate system shown, therefore all negative solutions are discarded (Dunkin, 1985).

Dunkin reported overall system accuracy to be ± 12 inches over a test area approximately 18 by 26 feet, primarily due to poor repeatability in the propagation delays associated with the RF control link which triggered the slaves. The magnitude of this inaccuracy obviously precludes any attempt to derive vehicle heading from complementary solutions for a pair of receivers mounted a known distance apart, since the ambiguity is of the same order as the maximum possible receiver separation. Significant improvement in accuracy could theoretically be obtained through optimization of the first prototype circuitry, and in fact Dunkin reported accuracies of ± 3.6 inches for the same test area when the RF link propagation uncertainties were eliminated through temporary use of hard-wired control lines.

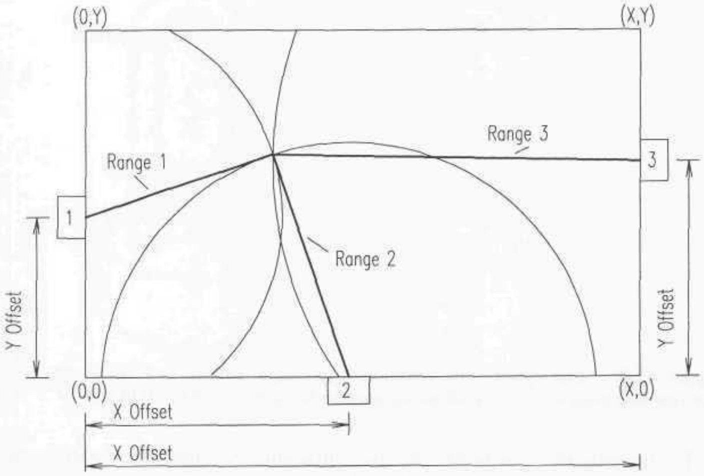

Figure 15-3. Example placement of three slave ultrasonic transmitters used to establish the position of the master receiver (robot) through trilateration (adapted from Dunkin, 1985).

IS Robotics 2-D Location System

IS Robotics, Inc. (ISR), Somerville, MA, markets an inexpensive ultrasonic trilateration system of this type that allows their *Genghis series* robots to localize position to within ±0.5 inches over a 30- by 30-foot operating area (ISR, 1994). The ISR system consists of a base-station master hard-wired to two slave ultrasonic "pingers" positioned a known distance apart (typically 90 inches) along the edge of the operating area as shown in Figure 15-4. Each robot is equipped with a receiving ultrasonic transducer situated beneath a cone-shaped reflector for omni-directional coverage. Communication between the base station and individual robots is accomplished using a Proxim spread-spectrum (902-928 MHz) RF link.

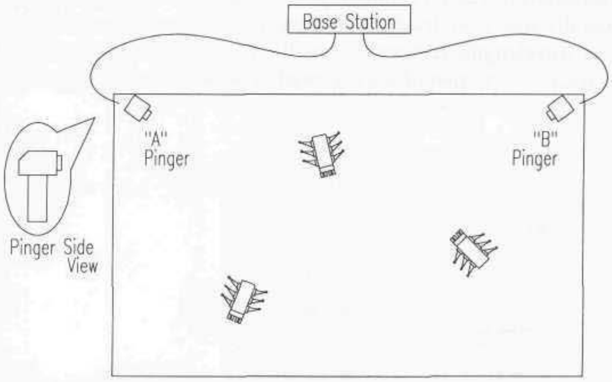

Figure 15-4. The ISR *Genghis* series of legged robots localize X-Y position with a master/slave trilateration scheme using two 40-KHz ultrasonic "pingers" synchronized via an RF spread-spectrum modem (courtesy IS Robotics, Inc.).

The base station alternately fires the two 40-KHz ultrasonic pingers every half second, each time transmitting a two-byte radio packet in broadcast mode to advise all robots of pulse emission. As with Dunkin's prototype, the elapsed time between radio packet reception and detection of the ultrasonic wavefront is used to calculate the distance between the robot's current position and the known location of the active beacon. Inter-robot communication is accomplished over the same spread-spectrum channel using a *time-division multiple-access* scheme controlled by the base station. Principle sources of error include variations in the speed of sound, the finite size of the ultrasonic transducers, non-repetitive propagation delays in the electronics, and ambiguities associated with time-of-arrival detection.

Tulane University 3-D Location System

Researchers at Tulane University in New Orleans, LA, have come up with some interesting methods for significantly improving the time-of-arrival measurement accuracy for ultrasonic transmitter/receiver configurations, as well as compensating for the varying effects of temperature and humidity. In the hybrid scheme illustrated in Figure 15-5, envelope peak detection is employed to establish the approximate time of signal arrival, and consequently eliminate ambiguity interval problems (Chapter 6) for a more precise phase-measurement technique that provides final resolution (Figueroa & Lamancusa, 1992). The desired 0.001-inch range accuracy required a time unit discrimination of ±75 nanoseconds at the receiver, which can easily be achieved using fairly simplistic phase measurement circuitry, but only within the interval of a single wavelength. The actual distance from transmitter to receiver is the summation of some integer number of wavelengths (determined by the coarse time-of-arrival measurement), plus that fractional portion of a wavelength represented by the phase measurement results.

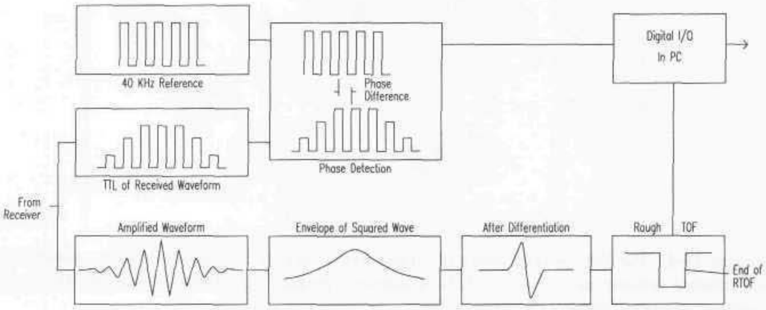

Figure 15-5. A combination of adjustable thresholding and phase detection is employed to provide higher accuracy in time-of-arrival measurements in the Tulane University ultrasonic position-location system (Figueroa & Lamancusa, 1992).

Details of this time-of-arrival detection scheme and associated error sources are presented by Figueroa and Lamancusa (1992). Range measurement accuracy of the prototype system was experimentally determined to be 0.006 inches using both adjustable thresholding (based on peak detection) and phase correction, as compared to 0.021 inches for adjustable thresholding alone. The high-accuracy requirements were necessary for an application that involved tracking the end effector of a six-DOF industrial robot (Figueroa, et al., 1992). The test setup shown in Figure 15-6 incorporates seven 90-degree Massa piezoelectric transducers operating at 40-KHz, interfaced to a 33-MHz IBM-compatible PC. The general position-location strategy was based on a trilateration method developed by Figueroa and Mahajan (1994).

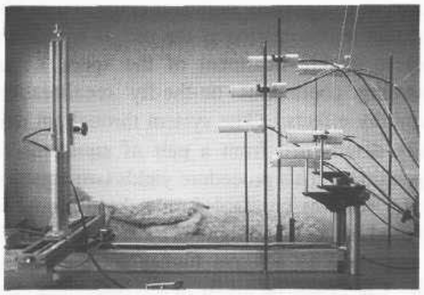

Figure 15-6. Experimental setup of the 3-D position location system showing the transmitter mounted on an X-Y-Z translation stage, and seven receivers distributed around the periphery of the work envelope (courtesy Tulane University).

The set of equations describing time-of-flight measurements for an ultrasonic pulse propagating from a mobile transmitter located at point (*u*, *v*, *w*) to various receivers fixed in the inertial reference frame can be listed in matrix form as follows (Figueroa & Mahajan, 1994):

$$\begin{Bmatrix} (t_1 - t_d)^2 \\ (t_2 - t_d)^2 \\ * \\ * \\ * \\ (t_n - t_d)^2 \end{Bmatrix} = \begin{bmatrix} 1 & r_1^2 & 2x_1 & 2y_1 & 2z_1 \\ 1 & r_2^2 & 2x_2 & 2y_2 & 2z_2 \\ * & & & & \\ * & & & & \\ * & & & & \\ 1 & r_n^2 & 2x_n & 2y_n & 2z_n \end{bmatrix} \begin{Bmatrix} \frac{p^2}{c^2} \\ \frac{1}{c^2} \\ -\frac{u}{c^2} \\ -\frac{v}{c^2} \\ -\frac{w}{c^2} \end{Bmatrix}$$

where:

t_i = measured time of flight for transmitted pulse to reach ith receiver
t_d = system throughput delay constant
r_i^2 = sum of squares of ith receiver coordinates
(x_i, y_i, z_i) = location coordinates of ith receiver
(u, v, w) = location coordinates of mobile transmitter
c = speed of sound
p^2 = sum of squares of transmitter coordinates.

The above equation can be solved for the vector on the right to yield an estimated solution for the speed of sound c, transmitter coordinates (u, v, w), and an independent term p^2 that can be compared to the sum of the squares of the transmitter coordinates as a checksum indicator (Figueroa & Mahajan, 1994). An important feature of this representation is the use of an additional receiver (and associated equation) to enable treatment of the speed of sound itself as an unknown, thus ensuring continuous on-the-fly recalibration to account for temperature and humidity effects. (The system throughput delay constant t_d can also be automatically determined from a pair of equations for $1/c^2$ using two known transmitter positions. This procedure yields two equations with t_d and c as unknowns, assuming c remains constant during the procedure.) A minimum of five receivers is required for an unambiguous three-dimensional position solution, but more can be employed to achieve higher accuracy using a least-squares estimation approach. Care must be taken in the placement of receivers to avoid singularities as defined by Mahajan (1992).

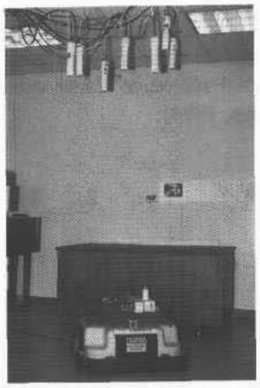

Figure 15-7. The ceiling-mounted ultrasonic position-location system achieves 0.01-inch accuracy with an update rate of 100 Hz (courtesy Tulane University).

Figueroa and Mahajan (1994) report a follow-up version intended for mobile robot position location (Figure 15-7) that achieves 0.01-inch accuracy with an update rate of 100 Hz. The prototype system tracks a TRC *Labmate* over a 9- by 12-foot operating area with five ceiling-mounted receivers, and can be extended to larger floor plans with the addition of more receiver sets. An RF datalink will be used to provide timing information to the receivers and to transmit the subsequent X-Y position solution back to the robot. (The current prototype incorporates a hard-wire tether.) Three problem areas are being further investigated to increase the effective coverage and improve resolution:

- Actual transmission range does not match the advertised operating range for the ultrasonic transducers, probably due to a resonant frequency mismatch between the transducers and electronic circuitry.
- The resolution of the clocks (6 MHz) used to measure time of flight is insufficient for automatic compensation for variations in the speed of sound.
- The phase-detection range-measurement correction sometimes fails when there is more than one wavelength of uncertainty. This problem can likely be solved using the frequency division scheme described by Figueroa and Barbieri (1991).

15.1.2 Ultrasonic Signature Matching

An alternative technique employed on ROBART II for periodically resetting the actual *X-Y* position and orientation was ultrasonic signature matching (Everett & Bianchini, 1987). This methodology was based on previous work done at Carnegie Mellon University, and later by Harrington and Klarer (1986; 1987) at Sandia National Laboratories (Figure 15-8).

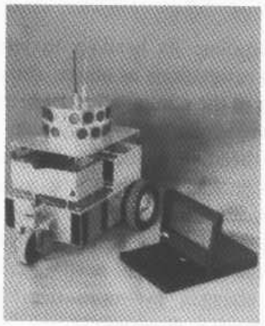

Figure 15-8. The Sandia Indoor Robot (courtesy Sandia National Laboratories).

Under this scheme, the robot must first perform a one-time "room digitizing" operation by moving in a raster-scan fashion through all unobstructed areas, stopping every 12 inches to fire the upper navigational sonar array. The ring of 24 ultrasonic sensors (spaced 15 degrees apart) thus generates a database of range returns, stored in polar coordinates, with an entry for each 12-inch square floor map unit marked as free. The database entries in effect represent unique signatures of the workspace (as seen by the ring of sensors) for each X-Y position in the map. The navigational array is placed as high as possible from the ground in order to minimize distortion due to the changing positions of transient objects.

When later performing a position estimation operation, the database of the operating area is searched for a location with a signature best matching the current set of range readings. An individual sensor return matches a database value if it falls within a specified window of acceptance, approximately 1.5 times the database resolution. Starting with the current dead- reckoned map position, the position estimator searches the database in an expanding fashion, looking for the entry (position) with the highest number of correlations matching the range values taken at the robot's present physical location.

The search algorithm also skews the current sonar data one sensor position (i.e. ±15 degrees) in each direction, in an attempt to correct for any error in current heading. If the highest number of correlations is not greater than a minimum threshold, the estimator searches a new set of neighbors farther from the original dead-reckoned position. Initial results using this technique at Sandia showed a sharp differential between the number of fits for a correct database match with respect to neighboring locations.

When a match is found with a sufficiently high correspondence, the robot's position is known to within 12 inches (the database resolution), and heading to within 15 degrees. To improve the positional accuracy, the estimator will interpolate a new location within the map, using the four sensor range values pointing 0, 90, 180, and 270 degrees relative to the robot (as long as each of these readings match their corresponding database returns within the specified tolerance).

The robot can also interpolate its heading to within about 1.5 degrees by performing several position estimations as above, rotating clockwise by 1 degree after each estimate. As long as the computed *X-Y* position and heading remain the same as the previous estimate, the robot continues to rotate and take range readings. If the estimated heading suddenly changes by 15 degrees while the estimated position remains unchanged, then it is assumed the robot has turned approximately halfway between the previous heading and the new heading. The interpolated heading can at this point be derived by subtracting 7.5 degrees (half the rotation interval) from the most recent heading estimate. If the *X-Y* position changes, or the heading changes by more than 15 degrees, then heading interpolation using this approach is discounted.

This database-search technique has proven to be fairly reliable for determining the robot's *X-Y* position during extensive testing, provided the operating environment does not change significantly. Some degradation is acceptable, as long as approximately 15 or more sensor readings of the 24 total are not affected. The number of correlations attained serves as a built- in indicator of database degradation, however, since as this number begins to approach the critical mark discussed above, the robot can simply initiate a new digitization routine to update the database. The only hitch here is some means of precisely monitoring the robot's position and orientation during this *build-database* process is required in order to ensure the database entries are themselves valid. To date, this has meant human supervision of the room digitizing operation.

15.2 Optical Position-Location Systems

Optically based position location systems typically involve some type of scanning mechanism operating in conjunction with fixed-location references strategically placed at pre-defined locations within the operating environment. A number of variations on this theme are seen in practice:

- Scanning detectors with fixed active-beacon emitters.
- Scanning emitter/detectors with passive retroreflective targets.
- Scanning emitter/detectors with active transponder targets.
- Rotating emitters with fixed detector targets.

One of the principle problems associated with optical beacon systems, aside from the obvious requirement to modify the environment, arises from the need to preserve a clear line of sight between the robot and the beacon. Preserving an unobstructed view is sometimes difficult if not impossible in certain applications such as congested warehouse environments. In the case of passive retroreflective targets, problems can sometimes arise from unwanted returns from other reflective surfaces, but a number of techniques exists for minimizing such interference.

15.2.1 CRAWLER I Homing Beacon

A very rudimentary method of beacon homing was implemented on the CRAWLER I robot introduced in Chapter 1 to facilitate automatic battery recharging. The scanning sensor was simply a cadmium-sulfide photoresistor mounted in the end of a 12-inch plastic tube (Figure 15-9). The collimating tube was rotated in the horizontal plane of the beacon by a small DC gearmotor from a sign display. A special contact sensor at the bottom of the rotating shaft was used to index the 0-degree position coinciding with the forward axis of travel.

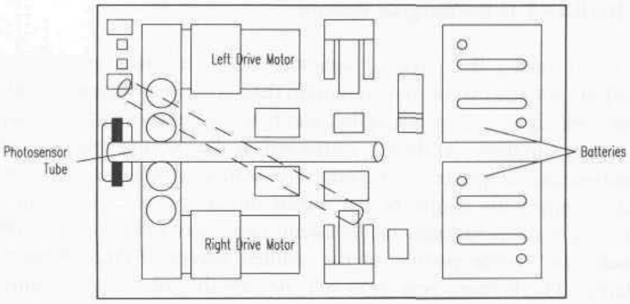

Figure 15-9. Top view of componentry layout on the CRAWLER I robot, showing the photosensor collimating tube aligned with the forward axis of travel, and displaced 30 degrees.

All of the control logic was implemented with surplus mechanical relays. The concept was simple enough; the photocell scanner rotated at a constant rate, and the turning action was started and halted by: 1) the shaft index sensor and 2) beacon detection by the photocell. The first sweep was used to determine if a beacon were present and in which direction the vehicle needed to turn. A pair of triple-pole double-throw relays were used to implement an electromechanical flip-flop to remember on which side of the vehicle the beacon had most recently been seen. (Keep in mind this was a high-school science project back in the mid-sixties).

For example, if the beacon lay off to the right side, the scanner would initiate a platform turn to the right by stopping the right drive motor when the collimating tube passed through the forward index (i.e., pointed straight ahead). As the sweep continued from left to right, the photocell would eventually detect the beacon, whereupon the control logic would restart the right drive motor. This process would repeat with each new sweep, and each time the turning action would last for a shorter period than before because the beacon would have moved closer to the 0-degree index as the robot turned toward it. When the beacon lay dead ahead, the sweep would start and stop the turn at the same time, therefore straight-line travel would not be interrupted.

A minor wrinkle in this scheme involved the fact that if the beacon were instead off to the left side, the events that initiated and terminated the turning action had to be interchanged. In other words, beacon detection would start the turn, and sweep index detection would halt it. The mechanics of this strategy were worked out in the relay logic, relying on the *photocell-left-or-right* information stored in the flip-flop to control the process. Fine tuning to achieve stability was accomplished by varying the sweep speed of the scanner with a rheostat. The results were surprisingly effective in light of the extremely crude design implementation.

15.2.2 ROBART II Recharging Beacon

Figure 15-10 shows the physical structure of the recharging system used by ROBART II. Situated above the aluminum base plate and electrically insulated by means of a Plexiglas spacer is a cylindrical housing containing the recharging and system power supplies. At the top of the unit is the homing beacon, visible from any direction and supported by a metal pipe with a coaxial extension that can be adjusted to match the height of the sensor on the robot. The homing beacon consists of a vertical-filament incandescent lamp surrounded by an optical filter that blocks the visible portion of the emitted energy (Kodak Wratten 89B or equivalent). The homing beacon is activated by the robot upon command via a dedicated radio link. Enclosed within the cylinder are the power supplies, a radio receiver, and associated decoding and control electronics.

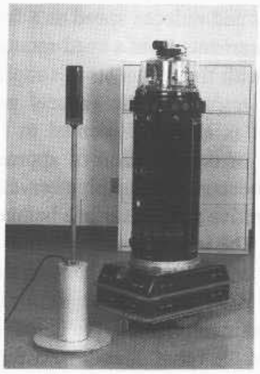

Figure 15-10. ROBART II approaches its automatic recharging station by homing in on the active near-infrared beacon shown at the top of the support pole.

There are two power supplies associated with the recharging station itself. A relatively low-current source remains energized at all times to power the radio receiver and also to energize the recharger contacts through a current-limiting resistor. This "sense" voltage (about 20 volts DC) allows the robot to know when a valid electrical connection has been established with the recharger. In addition, the sense voltage will drop to around 14 volts as soon as the battery has been connected as a load, activating the high-power battery charging supply after a 2-second delay. This second power supply furnishes the current required to recharge the battery and is automatically shut off when the robot disconnects. The delay is incorporated to allow the mating contacts to debounce before power is applied, markedly reducing contact erosion and pitting.

Once the battery monitor circuit on the robot detects a low-battery condition, the Scheduler initiates the docking sequence by requesting a path to the recharging station. The path planner first draws an imaginary circle of 24-inch radius around the last known location of the charger as encoded in the world model. A path is found to the nearest point of intersection with this circle and the robot then moves to this designated start position. The head pans from full left to full right, digitizing and storing the ambient light intensity of the room. The Scheduler next activates the homing beacon on the recharging station via the radio link and enters the beacon acquisition mode. The robot rescans the room from right to left, looking for a light source that was not present prior to beacon activation.

Positive identification is achieved by turning off the beacon while observing the selected target, after which the path planner updates the new beacon position in the model. The head pan position is servo-controlled to balance the outputs from two silicon photodetectors, and the resulting relative bearing used to calculate a steering command to cause the robot to turn in the appropriate direction. The robot relies on this optical tracking system to control heading while closing on the charger and reduces speed as a function of stand-off distance based on sonar range measurements from a head-mounted Polaroid transducer.

The task of connecting with the recharger is simplified by making the contact surfaces symmetrical with respect to the vertical pole supporting the homing beacon, so the same target is always presented to the mating contacts on the advancing robot regardless of the direction of approach. The cylindrical metal housing at the base of the beacon support pipe serves as the point of contact for the GND leg, with the respective mating surface being a metal strip attached to the front bumper of the robot. The inherent spring action of the tactile bumper keeps the conductive strip in tight contact with the housing once the two come together.

The connection for the HOT leg is made through the mating of two spring probes with the circular aluminum base plate. The probes extend vertically downward from the edge of the robot chassis. As the front of the chassis passes over the plate moving toward the metal housing supporting the beacon, the spring probes are brought into contact with the plate. Contact is maintained as motion continues toward bumper impact. The geometry of the configuration ensures the probes will be in contact with the plate as long as the front bumper contact is touching the power supply housing. Considerable margin for alignment error is allowed since the strip is 10 inches wide.

This recharging strategy was basically just a refinement and repackaging of the system developed earlier for ROBART I, which in turn was based on the original concept used by the CRAWLER robots back in 1965. In all three cases, the appropriate battery charger could be placed anywhere in the room, and the robot could quickly find it with no prior knowledge of its whereabouts. The underlying design philosophy was driven by an emphasis on making the docking operation as forgiving as possible to accommodate the known inadequacies of the navigation system. It eventually occurred to me that perhaps things should be the other way around. A fixed-location charger equipped with a homing beacon can provide a convenient mechanism for re-referencing a slightly disoriented robot. An alternative charging station incorporating this capability was developed for ROBART II and is discussed in Section 16.1.1.

15.2.3 Cybermotion Docking Beacon

The automated docking system used on the Cybermotion *Navmaster* robot incorporates a rather unique combination of a structured-light beacon to establish bearing, along with a one-way ultrasonic ranging system that determines stand-off distance. The optical portion consists of a pair of near-infrared transceiver units, one mounted on the front of the robot and the other situated in a known position and orientation within the operating environment. These two optical transceivers are capable of full-duplex data transfer between the robot and the dock at a rate of

9600 bits per second. Separate modulation frequencies of 154 and 205 KHz are employed for the uplink and downlink respectively to eliminate crosstalk. Under normal circumstances, the dock-mounted transceiver waits passively until interrogated by an active transmission from the robot. If the interrogation is specifically addressed to the assigned ID number for that particular dock, the dock control computer activates the beacon transmitter for 20 seconds. (Dock IDs are jumper selectable at time of installation.)

Figure 15-11 shows the fixed-location beacon illuminating a 90-degree field of regard broken up into two uniquely identified zones, designated for purposes of illustration here as the *Left Zone* and *Right Zone*. An array of LED emitters in the beacon head is divided by a pair of lenses and a double-sided mirror situated along the optical axis. Positive zone identification is initiated upon request from the robot in the form of a *NAV Interrogation* byte transmitted over the optical datalink. LEDs on opposite sides of the mirror respond to this *NAV Interrogation* with slightly different coded responses. The robot can thus determine its relative location with respect to the optical axis of the beacon based on the response bit pattern detected by the onboard receiver circuitry.

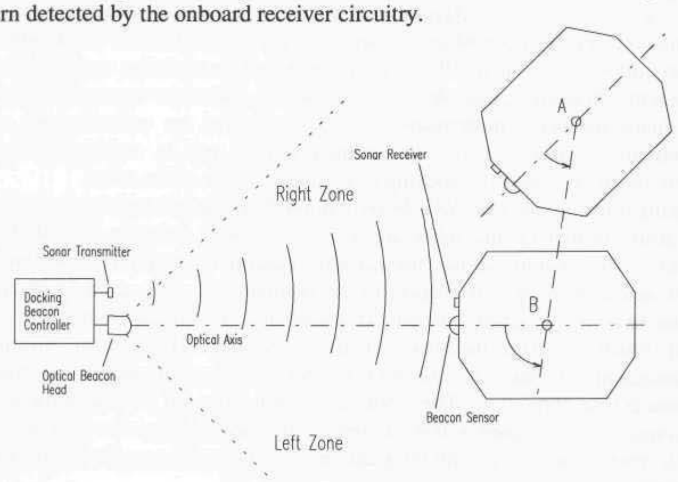

Figure 15-11. The structured-light near-infrared beacon on the Cybermotion battery recharging station defines an optimal path of approach for the *K2A Navmaster* robot.

When a docking action is requested (i.e., for recharging batteries, re-referencing position and azimuth, pick-up or delivery of material), the *Navmaster* moves into the general vicinity designated for dock approach (i.e., point *A*) and attempts to communicate with the dock via the near-infrared link. If no link is established, the robot scans first left and then right, aborting with a *Dock Failure* status if the search is unsuccessful. Assuming communications are established and the beacon is activated as discussed above, the robot sets the *Request to Dock* output bit at the dock and then waits for an acknowledgment. This handshaking procedure allows for any auxiliary equipment associated with the dock (that could conceivably interfere with the robot's approach) to report its status.

Once cleared to approach, the robot turns in the appropriate direction and executes the steepest possible (i.e., without losing sight of the beacon) intercept angle with the beacon optical axis. Crossing the optical axis at point *B* is flagged by a sudden change in the bit pattern of the *NAV Response Byte*, whereupon the robot turns inward to face the dock. The beacon optical axis establishes the nominal path of approach, and in conjunction with range offset information uniquely defines the robot's absolute location. This situation is somewhat analogous to a TACAN station (Dodington, 1989) with but a single defined radial.

Measuring the offset distance from vehicle to dock is accomplished in rather elegant fashion through use of a dedicated non-reflective ultrasonic ranging configuration. This high-frequency (>200 KHz) narrow-beam (15 degrees) sonar system consists of a piezoelectric transmitter mounted on the docking beacon head and a complimentary receiving transducer mounted on the front of the vehicle. A ranging operation is initiated upon receipt of the *NAV Interrogation Byte* from the robot; the answering *NAV Response Byte* from the docking beacon signals the simultaneous transmission of an ultrasonic pulse. The difference at the robot end between time of arrival for the *NAV Response Byte* over the optical link and subsequent ultrasonic pulse detection is used to calculate separation distance. This dual-transducer master/slave technique assures an unambiguous range determination between two well defined points and is unaffected by any projections on or around the docking beacon and/or face of the robot.

During transmission of a *NAV Interrogation Byte*, the left and right sides of the LED array located on the robot are also driven with uniquely identifiable bit patterns. This feature allows the docking beacon computer to determine the robot's actual heading with respect to the nominal path of approach. Recall the docking beacon's structured bit pattern establishes (in similar fashion) on which side of vehicle centerline the docking beacon is located. This heading information is subsequently encoded into the *NAV Response Byte* and passed to the robot to facilitate course correction. The robot closes on the beacon, halting at the defined stop range (not to exceed 8 feet) as repeatedly measured by the docking sonar. Special instructions in the path program can then be used to reset vehicle heading and/or position.

15.2.4 Hilare

Early work incorporating passive beacon tracking at the Laboratoire d'Automatique et d'Analyse des Systemes (LAAS), Toulouse, France, involved the development of a navigation subsystem for the mobile robot Hilare (Bauzil, et al., 1981). The system consisted of two near-infrared emitter/detectors mounted with a 25-cm vertical separation on a rotating mast, used in conjunction with passive reflective-beacon arrays at known locations in three corners of the room.

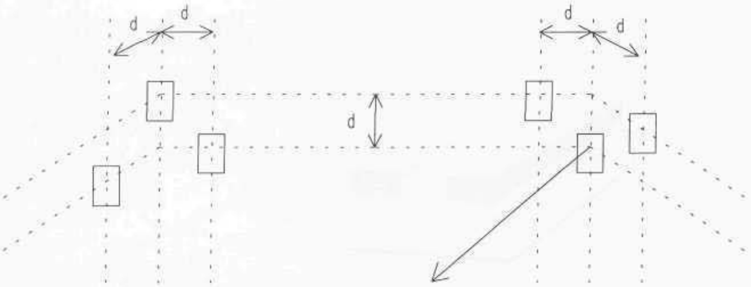

Figure 15-12. Retroreflective beacon array configuration used on the mobile robot Hilare (adapted from Bauzil, et al., 1981).

Each of these beacon arrays was constructed of retroreflective tape applied to three vertical cylinders, spaced in a recognizable configuration as shown in Figure 15-12. One of the arrays was inverted so as to be uniquely distinguishable for purposes of establishing an origin. The cylinders were vertically spaced to intersect the two planes of light generated by the rotating optical axes of the two emitters on the robot's mast. A detected reflection pattern as in Figure 15-13 confirmed beacon acquisition. Angular orientation relative to each of the retroreflective arrays was inferred from the stepper motor commands that drove the scanning mechanism; lateral position was determined through simple triangulation.

▨	R	▨
R	▨	R

Figure 15-13. A confirmed reflection pattern as depicted above was required to eliminate potential interference from other highly specular surfaces (Bauzil, et al., 1981).

15.2.5 NAMCO *Lasernet®* *Scanning Laser Sensor*

The NAMCO *Lasernet®* *Scanning Laser Sensor* introduced in Chapter 4 employs retroreflective targets distributed throughout the operating area of an *automated guided vehicle* in order to measure range and angular orientation (Figure 15-14). A servo-controlled rotating mirror pans a near-infrared laser beam through a horizontal arc of 90 degrees at a 20-Hz update rate. When the beam sweeps across a target of known dimensions, a return signal of finite duration is sensed by the detector. Since the targets are all the same size, the signal generated by a close target will be of longer duration than that from a distant one.

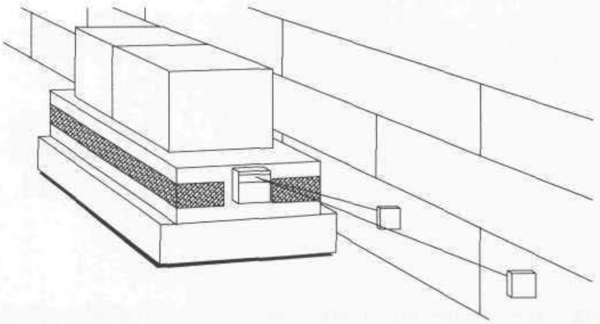

Figure 15-14. The *Lasernet*® system can be used with projecting wall-mounted targets to guide an AGV at a predetermined offset distance (courtesy NAMCO Controls).

Angle measurement is initiated when the scanner begins its sweep from right to left; the laser strikes an internal synchronization photodetector that starts a timing sequence. The beam is then panned across the scene until returned by a retroreflective target in the field of view. The reflected signal is detected by the sensor, terminating the timing sequence (Figure 15-15). The elapsed time is used to calculate the angular position of the target in the equation (NAMCO, 1989):

$$\theta = V T_b - 45$$

where:

θ = target angle
V = scan velocity (7200 degrees/sec)
T_b = interval between scan initiation and target detection.

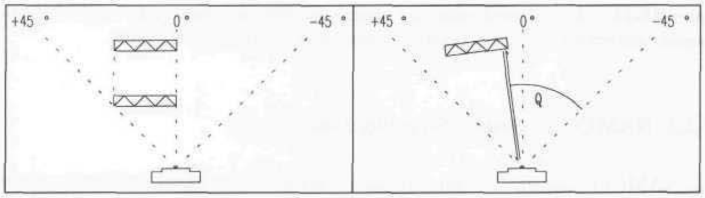

Figure 15-15. (A) Perceived width of a retroreflective target of known size is used to calculate range; (B) while the elapsed time between sweep initiation and leading edge detection yields target bearing (courtesy NAMCO Controls).

This angle calculation determines either the leading edge of the target, the trailing edge of the target, or the center of the target, depending upon the option selected within the *Lasernet*® software option list. The angular accuracy is ±1 percent, and the angular resolution is 0.1 degrees for the analog output; accuracy is within ±0.05 percent with a resolution of 0.006 degrees when the RS-232 serial port is used. The analog output is a voltage ranging from 0 to 10 volts over the range of ±45 degrees, whereas the RS-232 serial port reports a proportional "count value" from zero to 15,360 over this same range.

15.2.6 Caterpillar *Self-Guided Vehicle*

Caterpillar Industrial, Inc., Mentor, OH, manufactures a free-ranging AGV for materials handling that relies on a scanning laser triangulation scheme to provide positional updates to the vehicle's onboard dead-reckoning system. The Class-I laser rotates at 2 rpm to illuminate passive retroreflective barcode targets affixed to walls or support columns at known locations up to 15 meters away (Gould, 1990; Byrne, et al., 1992). The barcodes serve to positively identify the reference target and eliminate ambiguities due to false returns from other specular surfaces within the operating area. An onboard computer calculates X-Y positional updates through simple triangulation to null out accumulated dead-reckoning errors (Figure 15-16).

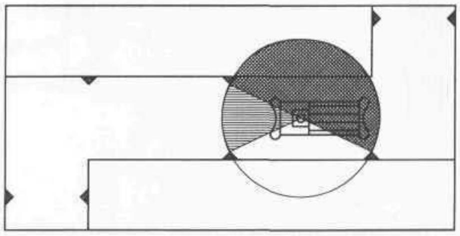

Figure 15-16. Retroreflective barcode targets spaced 10 to 15 meters apart are used by the Caterpillar SGV to triangulate position (adapted from Caterpillar, 1991a).

Some target occlusion problems have been experienced in an exterior application due to heavy fog, as would be expected, and minor difficulties have been encountered as well during periods when the sun was low on the horizon (Byrne, et al., 1992). The *Self-Guided Vehicle* relies on dead reckoning under such conditions to reliably continue its route for distances of up to 10 meters before the next valid fix.

The mobility configuration is a hybrid combination of tricycle and differential drives, employing two independent series-wound DC motors powering 18-inch rear wheels through sealed gearboxes (Caterpillar, 1991b). High-resolution resolvers (Chapter 2) attached to the single front wheel continuously monitor steering angle and distance traveled. A pair of mechanically scanned near-infrared proximity sensors sweeps the path in front of the vehicle for potential obstructions. Additional near-infrared sensors monitor the area to either side of the vehicle, while ultrasonic sensors cover the back.

15.2.7 TRC *Beacon Navigation System*

Transitions Research Corporation, Danbury, CN, has incorporated their LED-based *LightRanger* discussed in Section 6.1.7 into a compact, low-cost navigational referencing system for open-area autonomous platform control. The TRC *Beacon Navigation System* calculates vehicle position and heading at ranges up to 80 feet within a quadrilateral area defined by four passive retroreflective beacons as shown in Figure 15-17 (TRC, 1994). A static 15-second unobstructed view of all four beacons is required for initial acquisition and set-up, after which only two beacons must remain in view as the robot moves about the area. No provision is yet provided to periodically acquire new beacons along a continuous route, so operation is currently constrained to a single zone roughly the size of a small building (i.e., 80 by 80 feet).

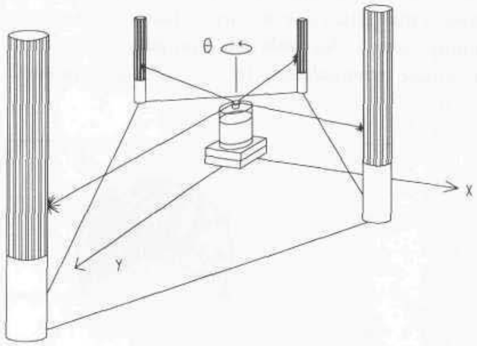

Figure 15-17. The TRC *Beacon Navigation System* calculates position and heading based on ranges and bearings to two of four passive beacons defining a quadrilateral operating area (courtesy TRC).

System resolution is 12 centimeters in range and 0.125 degrees in bearing for full 360-degree coverage in a horizontal plane. The scan unit (less processing electronics) is a cube approximately 10 centimeters on a side, with a maximum 1-Hz update rate dictated by the 60-rpm scan speed. A dedicated *68HC11* microprocessor continuously outputs navigational parameters (X, Y, θ) to the vehicle's onboard controller via an RS-232 serial port. Power requirements are 0.5 amps at 12 volts DC and 0.1 amp at 5 volts DC.

15.2.8 Intelligent Solutions *EZNav Position Sensor*

Intelligent Solutions, Inc. (ISI), Marblehead, MA, offers a laser-based scanning beacon system that computes vehicle position and heading out to 600 feet using cooperative electronic transponders (100 feet with passive reflectors). The *EZNav*

Position Sensor is a non-ranging triangulation system with an absolute bearing accuracy of ±0.03 degrees at a scan rate of 600 rpm (ISI, 1994a). The scanner mechanism consists of a rotating mirror attached at a 45-degree angle to the vertical shaft of an incremental optical encoder; for increased azimuthal accuracy, a timer interpolates between encoder counts (ISI, 1994b). Motor velocity is servoed under interrupt control every 100 milliseconds for a resolution of 0.1 percent.

The eye-safe near-infrared laser generates a 1-milliwatt output at 810 nanometers, amplitude modulated at 1.024 MHz to minimize interference from low-frequency ambient light sources. The fan-shaped beam is spread 4 degrees vertically to ensure target detection at long range while traversing irregular floor surfaces, with horizontal divergence limited to 0.3 milliradians. Each target is uniquely coded, and up to 32 separate targets can be processed in a single scan, with vehicle X-Y position calculated every 100 milliseconds (Maddox, 1994). The sensor package (Figure 15-18) weighs 10 pounds, measures 15 inches high and 12 inches in diameter, and has a power consumption of only 300 milliamps at 12 volts.

Figure 15-18. The *EZNav Position Sensor* can process up to 32 separate beacon targets per scan, with a complete X-Y position update computed at a 10-Hz rate (courtesy Intelligent Solutions, Inc.).

The *EZNav Position Sensor* is the latest development of this scanning laser technology. A similar version of this position sensor called *Lasernav* was previously developed by ISI engineers while working for Denning Mobile Robots. The *Lasernav* unit is used by the Mobile Robotics Laboratory at Georgia Tech as the primary navigational sensor on a Denning MRV-2 robotic base (Figure 15-19), in support of their work in reactive multiagent robotic systems (Balch & Arkin, 1994).

Figure 15-19. The earlier *Lasernav* prototype is used by Georgia Tech as the primary navigational referencing sensor on a Denning *MRV-2* robotic base (courtesy Georgia Institute of Technology).

15.2.9 Imperial College Beacon Navigation System

Premi and Besant (1983) of the Imperial College of Science and Technology, London, England, describe an AGV guidance system that incorporates a vehicle-mounted laser beam rotating in a horizontal plane that intersects three fixed-location reference sensors as shown in Figure 15-20. The photoelectric sensors are arranged in collinear fashion with equal separation, and are individually wired to a common FM transmitter via appropriate electronics so that the time of arrival of laser energy is relayed to a companion receiver on the vehicle. A digitally coded identifier in the data stream identifies the activated sensor that triggered the transmission, thus allowing the onboard computer to measure the separation angles α_1 and α_2. An absolute or indexed incremental position encoder monitoring laser scan azimuth is used to establish platform heading.

This technique has some inherent advantages over the use of passive retroreflective targets, in that false acquisition of specular surfaces is eliminated, and longer ranges are possible since target reflectivity is no longer a factor. More robust performance is achieved through elimination of target dependencies, allowing a more rapid scan rate to facilitate faster positional updates. The one-way nature of the optical signal significantly reduces the size, weight, and cost of the onboard scanner with respect to that required for retroreflective beacon acquisition. Tradeoffs, however, include the increased cost associated with installation of power and communications lines and the need for significantly more expensive beacons. This can be a significant drawback in very-large-area installations, or scenarios where multiple beacons must be incorporated to overcome line-of-sight limitations.

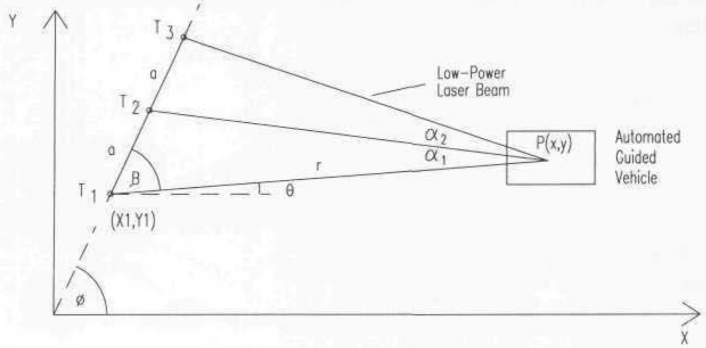

Figure 15-20. Three equidistant collinear photosensors are employed in lieu of retroreflective beacons in the Imperial College laser triangulation system for AGV guidance (adapted from Premi & Besant, 1983).

AGV position P(X,Y) is given by the equations (Premi & Besant, 1983):

$$x = x_1 + r\cos\theta$$

$$y = y_1 + r\sin\theta$$

where:

$$r = \frac{a\sin(\alpha_1 + \beta)}{\sin\alpha_1}$$

$$\beta = \arctan\left[\frac{2\tan\alpha_1\tan\alpha_2}{\tan\alpha_2 - \tan\alpha_1}\right] - \alpha_1$$

$$\theta = \phi - \beta$$

15.2.10 MTI Research *CONAC*

A similar type system using a predefined network of fixed-location detectors is currently being marketed by MTI Research, Inc., Chelmsford, MA. MTI's *CONAC (Computerized Optoelectronic Navigation and Control)* is a relatively low-cost high-performance navigational referencing system employing a vehicle-mounted laser *STROAB (STRuctured Optoelectronic Acquisition Beacon)*. The scanning laser beam is spread vertically to eliminate critical alignment, allowing the reference *NOADs (Networked Optoelectronic Acquisition Datums)* to be mounted at arbitrary heights (Figure 15-21). Detection of incident illumination by a *NOAD* triggers a response over the network to a host PC, which in turn calculates the implied angles α_1 and α_2. An index sensor built into the *STROAB* generates a special rotation reference pulse to facilitate heading measurement. Indoor accuracy is advertised at ± 0.05 inches for position and ±0.05 degrees for heading.

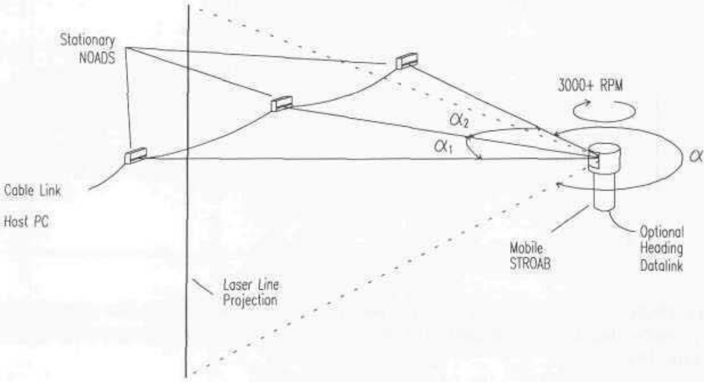

Figure 15-21. The patent-pending *Computerized Optoelectronic Navigation and Control (CONAC)* system employs a number of networked detectors tracking a rapidly scanning laser mounted on the moving vehicle (courtesy MTI Research, Inc.)

The reference *NOADs* are strategically installed at known locations throughout the area of interest, and daisy chained together with ordinary four-conductor modular telephone cable. Alternatively the *NOADs* can be radio linked to eliminate cable installation problems, as long as power is independently available to the various *NOAD* sites. (One project with MIT/Lincoln Laboratory involves a 2-kilometer system with a radio-*NOAD* spacing of 100 meters.) *STROAB* acquisition range is sufficient to where three *NOADs* can effectively cover a full acre assuming no interfering structures block the view. Additional *NOADs* are typically employed to increase fault tolerance, with the optimal set of three *NOADs* dynamically selected by the host PC, based on the current location of the robot and any predefined visual barriers. The selected *NOADs* are individually addressed over the network in accordance with assigned codes (set into DIP switches on the back of each device at time of installation).

An interesting and rather unconventional aspect of *CONAC* is that no fall-back dead reckoning capability is incorporated into the system (MacLeod & Chiarella, 1993). The 3000-rpm angular rotation speed of the laser *STROAB* facilitates rapid position updates at a 25-Hz rate, which MTI claims is sufficient for safe automated transit at highway speeds, provided line-of-sight contact is preserved with at least three fixed *NOADs*. To minimize chances of occlusion, the lightweight (less than 9 ounces) *STROAB* is generally mounted as high as possible on a supporting mast.

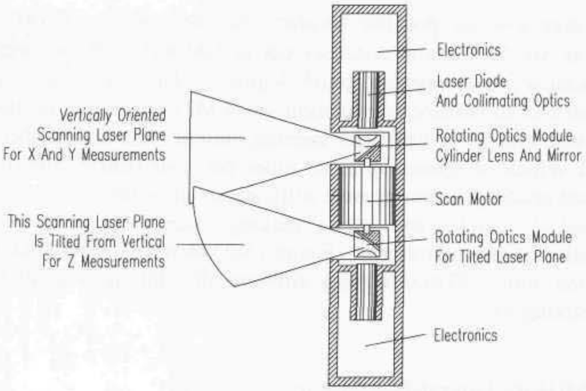

Figure 15-22. Simplified cross-sectional view of the dual-laser position location system now under development for tracking multiple mobile sensors in 3-D applications (courtesy MTI Research, Inc.).

A stationary active-beacon system that tracks an omni-directional sensor mounted on the robot is currently under development to allow for tracking multiple units. (The current *CONAC* system allows only one beacon to be tracked at a given time.) The basic system consists of two synchronized stationary beacons that provide bearings to the mobile sensor to establish its *X-Y* location. A hybrid version of this approach employs two lasers in one of the beacons as illustrated in Figure 15-22, with the lower laser plane tilted from the vertical to provide *Z*-axis resolution for three-dimensional applications.

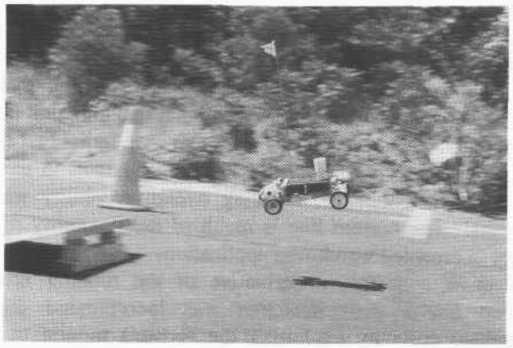

Figure 15-23. A small model car driven under *CONAC* control executes a preprogrammed raster-scan pattern in an outdoor parking lot before hitting the jump ramp with unerring precision (courtesy MTI Research, Inc.).

Long-range exterior position accuracy for the current *CONAC* system is specified as ±0.25 inches at distances out to 600 feet, with no degradation in heading accuracy over interior (±0.05 degrees). The system was successfully demonstrated in an outdoor environment when MTI engineers outfitted a Dodge *Caravan* with electric actuators for steering, throttle, and brakes, then drove the unmanned vehicle at speeds up to 50 miles per hour (Baker, 1993). Absolute position and heading accuracies were sufficient to allow the *Caravan* to maneuver among parked vehicles and into a parking place using a simple *AutoCad* representation of the environment. Figure 15-23 shows a 1/10th-scale model race car outfitted with a *STROAB* going airborne after hitting a small ramp in an outdoor parking lot.

15.2.11 MDARS Lateral-Post Sensor

A 360-degree field-of-view beacon tracking system of the type discussed above was considered for use on the MDARS Interior robot to assist in position referencing in semi-structured warehouse operations, but never implemented for a number of reasons. For starters, the effectiveness of a multiple-beacon triangulation scheme is to a large extent dependent on the overall field of view, which suggests the ideal scanning system should be located as high as possible with 360-degree coverage. In the case of a security robot, unfortunately, these same criteria likewise influence performance of both the surveillance camera and the intrusion-detection suite. Having three such sensor systems competing for a full-circle view at the very top of the robot introduces some non-trivial design challenges, complicated further still by the fact that video and datalink antennae also work best when situated above all other componentry.

Yet another important consideration is the likelihood of line-of-sight contact with a number of widely distributed beacons. Space is generally a premium in warehouse environments, and as a consequence vision is often restricted to straight shots up and down long narrow aisles. Surrounding shelving severely limits the effective coverage area for a conventional scanning unit and necessitates additional reflective beacons closely spaced down each individual aisle, adding to the cost of an already expensive system. Protruding targets in narrow aisles are vulnerable to fork truck damage, reducing overall reliability while increasing maintenance costs. The bottom line is much of the flexibility of a 360-degree capability is lost in crowded warehouse applications.

In light of these concerns, a derivative of the rotating laser referencing technique called *lateral post detection* was incorporated on MDARS to significantly reduce costs by exploiting the forward motion of the robot for scanning purposes. Short vertical strips of 1-inch-wide retroreflective tape are placed on various immobile objects (usually structural-support posts) on either side of a *virtual path* segment (Figure 15-24). The exact *X-Y* locations of these tape markers are encoded into the *virtual path* program. Installation takes only seconds, and since the flat tape does not protrude into the aisleway at all, there is little chance of damage from a passing fork truck.

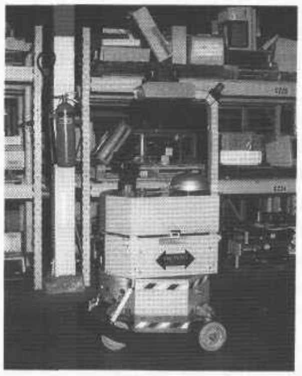

Figure 15-24. A short vertical strip of retroreflective tape can be seen affixed to the structural post in the MDARS warehouse environment (courtesy Naval Command Control and Ocean Surveillance Center).

A pair of Banner *Q85VR3LP* retroreflective sensors mounted on the turret of the *Navmaster* robot face outward to either side as shown in Figure 15-25. These inexpensive sensors respond to reflections from the tape markers along the edges of the route, triggering a "snapshot" *virtual path* instruction that records the current side-sonar range values. The longitudinal position of the platform is updated to the known marker coordinate, while lateral position is inferred from the sonar data, assuming both conditions fall within specified tolerances.

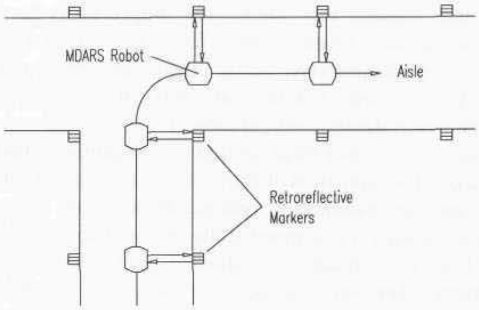

Figure 15-25. Polarized retroreflective sensors are used to locate vertical strips of reflective tape attached to shelving support posts in the Camp Elliott warehouse installation of the MDARS security robot.

The accuracy of the marker correction is much higher (and therefore assigned greater credibility) than that of the lateral sonar readings due to the markedly different uncertainties associated with the respective targets. The polarized Banner sensor responds only to the presence of a retroreflector while ignoring even highly specular surrounding surfaces, whereas the ultrasonic energy from the sonar will echo back from any reflective surface encountered by its relatively wide beam. Protruding objects in the vicinity of the tape (quite common in a warehouse environment) result in a shorter measured range value being read than the reference distance for the marker itself. The overall effect on *X-Y* bias is somewhat averaged out in the long run, as each time the vehicle executes a 90-degree course change the association of *X* and *Y* components with tape versus sonar updates is interchanged.

This lateral-post referencing concept was implemented on the MDARS unit in May 1994 and tested in an operational warehouse environment at Camp Elliott in San Diego, CA. The *Navmaster* robot was run continuously back and forth along a 150-foot path, with seven tape markers set on posts 20 feet apart. No other navigational referencing instructions were contained in the path program. Initial heading and location errors were quickly nulled out after the second or third post was detected, and accumulated errors remained essentially insignificant for the remaining length of the path. Each time the robot reversed course at the end of a run, some noticeable heading error was introduced on the diagnostic display but then quickly resolved as lateral-post updates were processed on the return leg.

We tried to get the system to fail by purposely injecting errors into the sonar range measurements. An increasing number of markers were corrupted throughout the course of this test by placing protruding objects (i.e., false sonar targets) immediately adjacent to the retroreflective tape. These objects were extended further and further into the aisle until at the end of the test, four of seven markers were in error with associated offsets of 7.5", 16", 10.5", and 6.5". Various combinations were tried in terms of which markers to perturb in an effort to generate the worst-case scenario (i.e., every other one, or four in a row). In general, the system remains very stable, and simply shifts the path laterally to accommodate the induced range offset. The robot's track basically follows a profile determined by the perceived sonar targets, and the platform continues to navigate in a very robust fashion without any noticeable instabilities.

An alternative triangulation configuration (Figure 15-26) can be employed to completely eliminate this sonar range ambiguity altogether by taking advantage of the excellent target discrimination feature of the Banner sensor. Two identical retroreflective units are mounted at oblique angles from the normal and with known separation baseline d_s, symmetrically oriented so their converging beams cross at point E a fixed distance x_c (about 3 to 4 feet) from the robot. The measured difference between leading-edge detection by the two sensors in conjunction with the known speed V_r of the robot determines the effective relative displacement *d* of the target along path CD (or path C'D') in the robot's reference frame. The sequence of detection (i.e., Sensor A followed by Sensor B, or vice versa) determines whether the tape stripe lies inside of or beyond the point of convergence of the beams, thus eliminating any ambiguity.

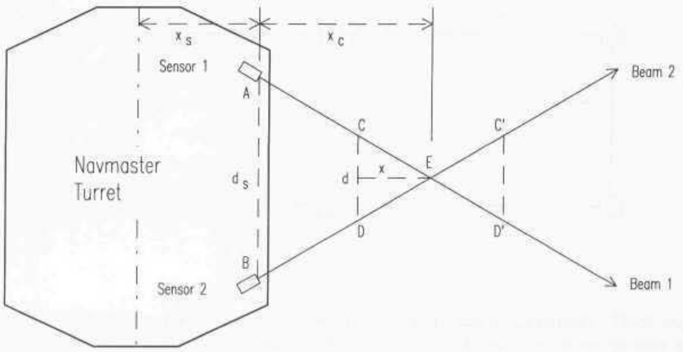

Figure 15-26. A pair of retroreflective sensors on each side of the *Navmaster* turret can be used to triangulate range to the retroreflective tape marker.

Triangles *ABE* and *CDE* are similar triangles, and so:

$$\frac{x}{x_c} = \frac{d}{d_s} \quad \text{which yields:} \quad x = \frac{d\, x_c}{d_s} = \frac{v_r\, t\, x_c}{d_s}$$

where:

x = target offset from point of beam convergence
x_c = known distance from robot to point of convergence
d = effective displacement of target due to robot motion
v_r = velocity of robot
t = measured time between target detections.

The vehicle lateral offset x_v from the known position of the tape marker is then given by:

$$x_v = x_s + x_c \pm x$$

where:

x_v = perceived lateral distance from vehicle centerline to marker position
x_s = lateral mounting offset between sensors and vehicle centerline.

The sign of x is positive if sensor 2 detects the tape marker before sensor 1.

One of the drawbacks of this method is increased possibility of target occlusion due to protruding objects on either side of the tape. Preliminary MDARS experience has shown that the highest probability of post detection exists for straight-in sighting directly normal to the path axis. An angled beam, on the other hand, is more likely to be masked as shown in Figure 15-27.

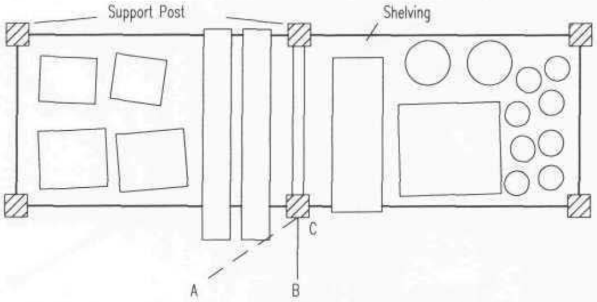

Figure 15-27. Protruding objects in the vicinity of a reflective marker will interfere with the sonar range measurements and can also occlude an off-normal optical sensor view such as along path AC.

A second problem encountered with the triangulation ranging approach in this scenario is the dependence on platform velocity. In the case of the *Navmaster,* a relatively slow update rate (10 Hz) of velocity information over the internal communications net could introduce errors if acceleration or deceleration should occur during the timing operation. Constant velocity cannot be assured in the vicinity of the markers since the collision avoidance strategy automatically servos speed of advance in relationship to perceived congestion.

15.3 References

Baker, A., "Navigation System Delivers Precision Robot Control," Design News, p. 44, December, 1993.

Balch, T., Arkin, R.C., "Communication in Reactive Multiagent Robotic Systems," *Autonomous Robots*, Vol. 1, pp. 1-25, Kluwer Academic Publishers, Boston, MA, 1994.

Bauzil, G., Briot, M., Ribes, P.., "A Navigation Subsystem Using Ultrasonic Sensors for the Mobile Robot Hilare," Proceedings of 1st Conference on Robot Vision and Sensory Control, Stratford/Avon, U.K., pp. 47-58, 13 April, 1981.

Byrne, R.H., Klarer, P.R., Pletta, J.B., "Techniques for Autonomous Navigation," Sandia Report SAND92-0457, Sandia National Laboratories, Albuquerque, NM, March, 1992.

Caterpillar, Product Literature, SGV-1092/91, Caterpillar Self Guided Vehicle Systems, Mentor, OH, 1991a.

Caterpillar, Product Literature, SGV-1106/91, Caterpillar Self Guided Vehicle Systems, Mentor, OH, 1991b.

Dodington, S.H., "Electronic Navigation Systems," *Electronic Engineer's Handbook,* D. Christiansen and D. Fink, eds., 3rd edition, New York, McGraw Hill, pp. 76-95, 1989.

Dunkin, W.M., "Ultrasonic Position Reference Systems for an Autonomous Sentry Robot and a Robot Manipulator Arm", Masters Thesis, Naval Postgraduate School, Monterey, CA, March 1985.

Everett, H.R., Bianchini, G.L., "ROBART II; An Intelligent Security Robot", Proceedings, U.S. Army Training and Doctrine Command Artificial Intelligence and Robotics Symposium, June 1987.

Figueroa, J.F., Doussis, E., Barbieri, E., "Ultrasonic Ranging System for 3-D Tracking of a Moving Target," 92-WA/DSC-3, Proceedings, Winter Annual Meeting, American Society of Mechanical Engineers, Anaheim, CA, November, 1992.

Figueroa, J.F., Lamancusa, J.S., "A Method for Accurate Detection of Time of Arrival: Analysis and Design of an Ultrasonic Ranging System," Journal of the Acoustical Society of America, Vol. 91, No. 1, pp. 486-494, January, 1992.

Figueroa, J.F., Barbieri, E., "Increased Measurement Range Via Frequency Division in Ultrasonic Phase Detection Methods," *Acustica*, Vol. 73, pp. 47-49, 1991.

Figueroa, J.F., Mahajan, A., "A Robust Navigation System for Autonomous Vehicles Using Ultrasonics," *Control Engineering Practice*, Vol. 2, No. 1, pp. 49-59, 1994.

Gould, L., "Is Off-Wire Guidance Alive or Dead?" Managing Automation, pp. 38-40, May, 1990.

Harrington, J.J., Klarer, P. R., "Development of a Self- Navigating Mobile Interior Robot Application as a Security Guard/Sentry", Sandia Report SAND86-0653, Sandia National Laboratories, July, 1986.

Harrington, J.J., Klarer, P.R., "SIR-1: An Autonomous Mobile Sentry Robot," Technical Report SAND87-1128, UC-15, Sandia National Laboratories, May, 1987.

ISI, "EZNav Position Sensor," Product Literature, Intelligent Solutions, Inc., Marblehead, MA, 1994a.

ISI, "EZNav Descriptive Manual," Product Literature, Intelligent Solutions, Inc., Marblehead, MA, April, 1994b.

ISR, *Radio Communications Option, Genghis Edition*, Product Literature, IS Robotics, Inc., Somerville, MA, May, 1994.

Lamancusa, J.S., Figueroa, J.F., "Ranging Errors Caused by Angular Misalignment Between Ultrasonic Transducer Pairs," *Journal of the Acoustical Society of America*, Vol. 87, No. 3, pp. 1327-1335, March, 1990.

MacLeod, E.N., Chiarella, M., "Navigation and Control Breakthrough for Automated Mobility," Proceedings, SPIE Mobile Robots VIII, Vol. 2058, pp. 57-68, 1993.

Maddox, J., "Smart Navigation Sensors for Automatic Guided Vehicles," *Sensors*, pp. 48-50, April, 1994.

Mahajan, A., "A Navigation System for Guidance and Control of Autonomous Vehicles Based on an Ultrasonic 3-D Location System," Master's Thesis, Mechanical Engineering Department, Tulane University, July, 1992.

NAMCO, "LNFL03-A 5M/4-90," *Lasernet* Product Bulletin, NAMCO Controls, Mentor, OH, November, 1989.

Premi, S.K., Besant, C.B., "A Review of Various Vehicle Guidance Techniques That Can Be Used by Mobile Robots or AGVs," 2nd International Conference on Automated Guided Vehicle Systems, Stuttgart, Germany, June, 1983.

TRC, *Beacon Navigation System*, Product Literature, Transitions Research Corporation, Danbury, CN, 1994.

16

Wall, Doorway, and Ceiling Referencing

For purposes of navigational referencing, indoor robotic systems can take advantage of a number of established landmarks in the form of wall structures, doorways, and ceilings or overhead beams that are not available in outdoor scenarios. (Outdoor applications, on the other hand, can take advantage of differential GPS, which is ineffective indoors due to signal blockage.)

16.1 Wall Referencing

Interior walls are probably the most commonly used structural attribute for deriving position and orientation information, with performance results determined primarily by the inherent accuracy limitations of the measurement techniques employed. Existing methodologies can be divided into four general classes:

- *Tactile* — The robotic platform aligns itself through direct physical contact with a wall of known orientation and location.
- *Non-Contact (Static)* — The platform faces off to a wall from a stationary position and determines offset and orientation from non-contact range data.
- *Non-Contact (Dynamic)* — The platform derives offset and heading from continuous real-time range data while in motion.
- Some combination of the above.

16.1.1 Tactile Wall Referencing

One obvious solution to the navigational re-referencing problem would be to bring the robot into actual contact (and alignment) with a predesignated wall section free of obstructions. The robot's heading under these conditions would be precisely orthogonal to the known wall orientation, with its positional offset from the wall equally unambiguous. While not very elegant, this method is extremely robust in the sense that range measurement inaccuracies are virtually eliminated. An added advantage is seen in the effective minimization of any backlash in the drivemotor reduction gears, since both gear trains are preloaded in the same direction. This tactile wall-referencing concept was implemented on ROBART II as an interim measure, pending the development of more sophisticated methods that did not require the robot to deviate from assigned functions solely for the purpose of resetting the navigational position and heading parameters.

To initiate this re-referencing procedure, the platform first moves to a position about 3 feet out and facing an unobstructed wall, based on the current dead-reckoning position information. The recalibration routine is then requested, whereupon the *Scheduler* computer (see Chapter 1) on board the robot assumes control. With the robot stationary, the *Scheduler* requests a sonar update from the *collision avoidance array* and checks to see that the robot is indeed within 4 feet from the wall. If the measured range exceeds 4 feet, an error message is generated. Otherwise, the ranges seen by transducer #1 (mounted on the head) and transducer #8 (center of lower array) are compared; with the robot facing an unobstructed wall, these ranges should be nearly equal. If the lower range is less than the upper range by more than a specified tolerance, some obstruction is assumed to be present between the robot and the wall (Figure 16-1), and this situation is reported to the *Planner* as an error condition.

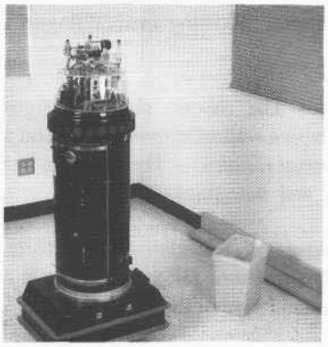

Figure 16-1. An interfering obstruction shows up in the form of conflicting range values for the upper and lower forward-looking sonar sensors.

Assuming no discrepancies are detected, the *Scheduler* requests repeated updates from sonar transducer #8 and initiates forward travel, decreasing speed as the range to the wall falls off. When the measured distance drops below 19 inches, the *Scheduler* checks the lower three *near-infrared optical proximity sensors* for wall confirmation. The sensitivities of the outer two proximity sensors are set to acquire the wall surface at a distance of 26 inches, while the center is set for a distance of 32 inches; therefore, all three should see the wall at 19 inches. If such is not the case, action is taken in accordance with the following rules:

- If none of the sensors see a target, forward motion is halted and an error message is sent to the *Planner*.
- If the center sensor only sees a target, forward motion is halted, and an error message is sent to the *Planner*.
- If the left sensor only does not see a target, the right drive motor is halted, causing the robot to turn right.
- If the right sensor only does not see a target, the left drive motor is halted, causing the robot to turn left.

The software loops in this mode until all three sensors see the wall, whereupon straight-line travel is resumed, or an error condition occurs. The last two rules above have the effect of correcting any gross misalignments with the wall surface prior to impact. Preliminary alignment could also be accomplished in the wall approach by doing a line-fitting operation on data from the lower *collision avoidance array* (see next section).

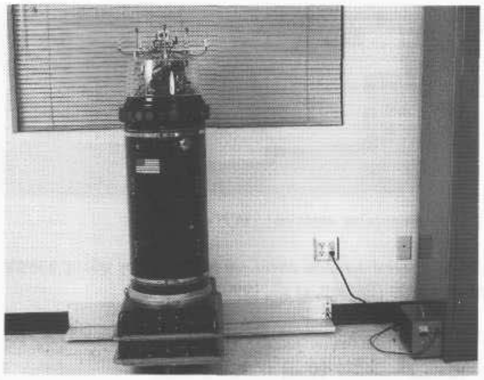

Figure 16-2. When ROBART II is firmly docked at the wall charging strip, heading and longitudinal position errors are eliminated.

At this point, the robot should be moving forward towards the wall at minimum speed (1.07 inches/second). The *Scheduler* waits for wall impact with the tactile bumper (Chapter 3) and stops each drivemotor when its associated side of the bumper indicates contact. For example, if the left side of the bumper deflects first, the *Scheduler* stops the left drivemotor, allowing the right motor to continue until such time as the right side of the bumper deflects. This reflexive action turns the robot in such a way as to square it off to the wall, whereupon forward motion stops. The *Scheduler* next backs the platform away from the wall exactly 1 inch and then resumes forward travel at minimum speed for two seconds. Wheel slippage occurs for approximately half a second as the robot's forward travel is halted upon contact with the wall (Figure 16-2), thereby symmetrically preloading the drive reduction gears to minimize backlash errors.

With the spring-loaded tactile bumper pressed firmly against the wall, and both motors stopped, the *Scheduler* requests range data from the two side-looking sensors in the upper *navigational sonar array*. One (or both) of these ranges represents the distance to a known lateral reference target, such as a bookcase (Figure 16-3) or orthogonal wall surface. This measured range is relayed to the *Planner*, completing the navigational parameter update. With this information, the robot's perceived location is updated in the model, thus eliminating any accumulated dead-reckoning errors. If the wall surface is suitably equipped with contact plates for recharging the onboard batteries (Figure 16-2), this method of recalibration becomes a little more practical than would otherwise be the case, in that the robot needs to make physical contact anyway in order to recharge.

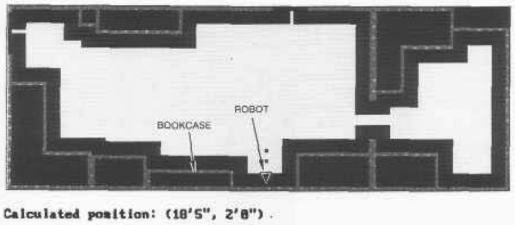

```
Calculated position: (18'5", 2'8") .
```

Figure 16-3. Lateral position errors are nulled out by taking a sonar range reading to the bookcase on the robot's right (Everett, et al., 1990).

16.1.2 Non-Contact Wall Referencing

Stationary walls of known orientation offer an attractive mechanism for resetting system heading as well as one component of the lateral position, even without actual physical contact. The concept as implemented on ROBART II calls for positioning the robot near an unobstructed wall surface, and then sequentially firing the 11 transducers in the lower *collision avoidance sonar array*. A line-fitting operation can then be performed on the subsequent data (Table 16-1) from the five transducers in the vicinity of the minimum range value. (The minimum range theoretically should represent the reading from that transducer whose axis was most nearly orthogonal to the wall surface.) The angle of the resulting line with respect to the robot is used to adjust the robot's perceived heading based on the known orientation of the wall (Figure 16-4). In addition, the robot's longitudinal offset from this wall is made available as well.

Table 16-1. Measured sonar data for angular orientation of -7.5 degrees (see Figure 16-4).

Range (inches)	Bearing (degrees)	X (inches)	Y (inches)
35.55	36	20.87	28.72
30.75	18	9.50	29.24
30.75	0	0.00	30.75
35.55	-18	-10.97	33.76
41.95	-36	-24.66	33.94

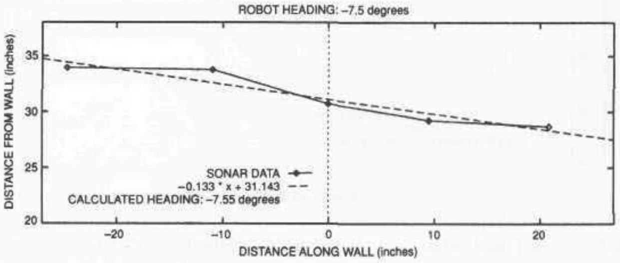

Figure 16-4. A calculated angular offset of -7.55 degrees is obtained for an actual orientation of -7.5 degrees (adapted from Everett, et al., 1990).

A complete navigational update (*X-Y* position and heading) could theoretically be obtained in a corner situation at the intersection of two orthogonal walls. Attempts to determine platform heading using this concept on ROBART II, however, met with only limited success due to specular reflection and beam divergence (see Figure 16-5). These problems were aggravated by the physical orientation of the ranging sensors, which fanned out radially from the cylindrical housing. This arrangement works to your advantage when trying to detect an obstacle for collision avoidance purposes, as the odds of a single transducer being nearly normal to the target surface are greatly increased. On the other hand, the odds of two or more transducers in the radial array being normal to a planar wall surface are likewise inherently low. The range values associated with those sensors which are not normal to the wall surface, obviously, are going to be adversely affected (Table 16-2), as accuracy falls off when the angle of incidence varies from the perpendicular. Since fairly accurate data from at least three transducers is required for the wall referencing algorithm to function properly, this represents a fundamental problem.

Table 16-2. Measured sonar ranges for angular orientation of 7.5 degrees (see Figure 16-5).

Range (inches)	Bearing (degrees)	X (inches)	Y (inches)
43.55	36	25.60	35.23
35.55	18	10.99	33.81
35.55	0	0.00	35.55
33.95	-18	-10.49	32.29
41.95	-36	-24.66	33.94

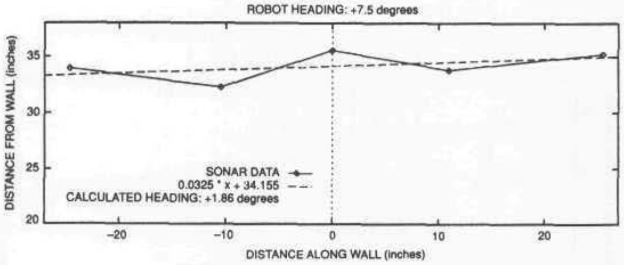

Figure 16-5. A calculated offset of 1.86 degrees is obtained for an actual orientation of 7.5 degrees.

One possible solution that was considered called for placing two or more additional ultrasonic ranging transducers along the front panel of the robot's base, which was a planar as opposed to cylindrical surface as shown in Figure 16-6. The platform would first rotate in place to turn to the heading indicated by the axis of the minimum range value discussed above, and then fire the front panel sensors; the resulting range values should be close in value if in fact the front panel were aligned parallel to the wall. If the difference was not within a specified tolerance, the robot would rotate slightly to correct the discrepancy. Once roughly aligned in this fashion, the front panel sensors, all normal to the target surface, would provide the highly accurate range data needed by the line-fit algorithm, which would subsequently determine the robot's precise angular orientation with respect to the wall. Alternatively, inexpensive short-range (5 to 6 feet) optical ranging systems with tightly focused beams and less susceptibility to problems associated with specular reflection could be employed for this application in place of the ultrasonic rangefinders.

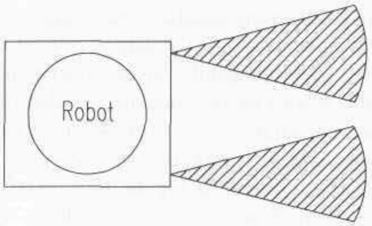

Figure 16-6. Potential mounting configuration for two additional sonar transducers to facilitate wall referencing on ROBART II (adapted from Everett, et al., 1990).

The Cybermotion *Navmaster* robot employs a *virtual path instruction* known as "wall approach" to reset the longitudinal displacement parameter only (i.e., no attempt is made to determine platform heading). The robot is known to be approaching a wall directly ahead and has been told that at the end of the current path segment it should be a certain distance from this wall. Knowing the absolute position of the wall, the robot can then update the unknown coordinate using the measured range in the forward direction upon completion of the move. Cybermotion's "wall-approach" instructions are generally used in conjunction with "wall-following" instructions (see next section) for a complete navigational solution (Holland, et al., 1990).

16.1.3 Wall Following

Wall following is another type of referencing technique, similar to the method described above, except that it takes place while the robot is traveling along a wall rather than facing it. Both the TRC *HelpMate* (Krishnamurthy, et al., 1988) and the Cybermotion *Navmaster* (Holland, et al., 1990) robots rely extensively on *wall-following* strategies. The nomenclature is somewhat misleading in the sense that the robot does not actually follow the wall in a servo-controlled fashion, but rather obtains a navigational reference from it. Only a single side-looking transducer is required, as the forward motion of the robot is exploited to provide the baseline separation required for heading calculation. While *wall following* can be used to effectively reset the robot's heading and lateral (either the X or Y) position coordinate, the longitudinal displacement along the path of travel remains unknown.

The basic procedure is described by Kadonoff (1990) and typically applied where the robot is traveling parallel to a wall of known position and orientation with a specified lateral separation. During the execution of this path segment, the robot repetitively fires a non-contact ranging sensor that is perpendicular to and facing the wall. Over a period of time the system thus accumulates several data points, each consisting of the measured range to the wall and the associated longitudinal position of the robot along the path of travel. A straight-line fit can be made to these data points using standard linear regression techniques (Devore, 1982). If a "good" fit is obtained (i.e., the data do not deviate significantly from a straight line), the line is accepted and the lateral offset from the wall as well as the current heading of the robot can be calculated as described below. With this information, the robot can adjust course to correct its offset and heading, turning toward or away from the wall as appropriate.

A simple example is illustrated in Figure 16-7. The robot begins the *wall-following* maneuver at point A and proceeds to point B, with the measured sonar ranges indicated in the figure by lines emanating from the robot and terminating somewhere near the wall shown at the bottom. Table 16-3 lists the range data collected by the side-looking sonar as a function of longitudinal displacement along path segment AB.

Table 16-3. Sonar versus actual (measured) range readings along path segment AB of Figure 16-7.

Path Position	Sonar Range	Actual Range	Path Position	Sonar Range	Actual Range	Units
0.0	33.2	33.7	59.8	36.2	36.6	inches
5.4	33.7	33.7	66.8	36.4	36.6	inches
11.2	33.8	34.2	72.2	36.5	37.1	inches
19.3	34.2	34.7	78.4	36.6	37.1	inches
23.9	34.6	34.7	84.8	36.8	37.4	inches
29.4	34.8	35.2	90.4	37.2	37.4	inches
36.0	35.3	35.6	96.6	37.6	37.9	inches
42.7	35.5	36.1	102.5	37.9	37.9	inches
49.9	35.9	36.1	108.0	38.0	38.4	inches
55.9	36.1	36.6	114.0	38.2	38.4	inches

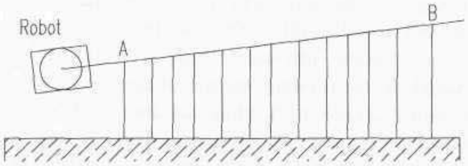

Figure 16-7. A line-fit operation is performed on several sonar range readings taken while the robot is in motion to establish relative heading and lateral offset with respect to the wall.

The linear regression equations used to calculate the slope, intercept, and estimated variance are as follows (Everett, et al., 1990):

$$m = \frac{n\sum(x_i\, y_i) - \sum x_i \sum y_i}{n\sum x_i^2 - (\sum x_i)^2}$$

$$Y_I = \frac{\sum y_i - m\sum x_i}{n}$$

$$\sigma^2 = \frac{\sum y_i^2 - Y_I \sum y_i - m\sum(x_i y_i)}{n-2}$$

where:

m = slope
n = number of sonar readings taken (20 in this example)
σ^2 = variance
Y_I = intercept.

Using these formulas, the equation of the line (Figure 16-8) resulting from the use of the sonar range values is:

$$y = 0.0416\,x + 33.885 \qquad \sigma^2 = 0.0530.$$

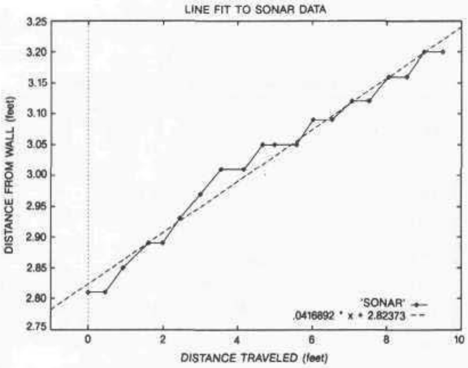

Figure 16-8. Plot of actual sonar data from Table 16-3 and resulting least-squares fit (Everett, et al., 1990).

Similarly, the equation of the line (Figure 16-9) using the robot's measured position from the wall is:

$$y = 0.0420\,x + 33.517 \qquad \sigma^2 = 0.0335.$$

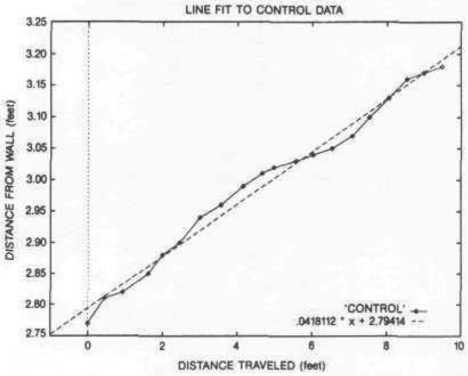

Figure 16-9. Plot of measured (reference) data from Table 16-3 and resulting least-squares fit. Undulations in the data are caused by imperfections in the wall itself (Everett, et al., 1990).

Figure 16-10 below shows a comparison of the two lines: the slopes are extremely close and the sonar data is offset from the measured (reference) data by only 0.03 feet (0.36 inch).

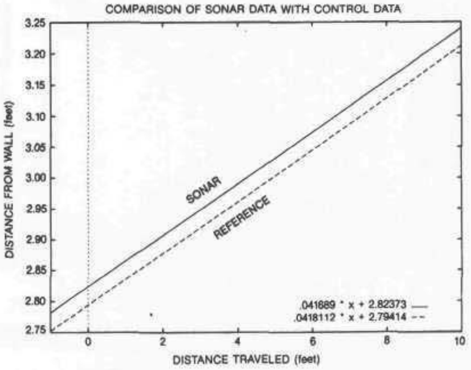

Figure 16-10. A comparison of the sonar and reference line-fit operations depicted in Figure 16-8 and Figure 16-9 above depict a lateral offset of about 0.3 inches (Everett, et al., 1990).

The robot's heading with respect to the wall can be calculated by taking the arctangent of the slope. For the sonar data, this yields:

$$\theta = \arctan(0.0416) = 2.382 \text{ degrees}$$

while for the measured (reference) data:

$$\theta = \arctan(0.0420) = 2.405 \text{ degrees.}$$

In this particular example, the sonar-estimated heading of 2.382 degrees varies by only 0.023 degrees in comparison to the actual measured results.

16.2 Doorway Transit Referencing

The concept of using existing interior doorways as navigational landmarks has always been appealing, in that no modifications to the surrounding environment are required. In certain indoor environments, the robot by necessity must travel through a doorway to enter an adjoining space. If in so doing the system could obtain an accurate positional update, then such would indeed represent an elegant solution to the problem of cumulative dead-reckoning errors. The doorway penetration approach employed on ROBART II can be decomposed into the following tasks:

- Finding the doorway.
- Entering the doorway.
- Verifying the doorway.
- Determining longitudinal position relative to doorway.
- Determining lateral position relative to doorway.
- Determining heading (angular orientation) relative to doorway.

The first of these tasks is addressed through use of a combination of ultrasonic ranging sensors, which have good distance measurement capability but poor angular resolution, and optical proximity sensors, which typically have superior angular resolution but little or no ranging capability. The problem is greatly simplified by virtue of the fact that the *Planner* knows where the door is located within the map structure and can direct the robot reasonably well to the vicinity of this position. In addition, the *Planner* always orients the path segment that actually penetrates the door opening to be orthogonal to the associated wall. With such *a priori* information, the task of finding the doorway's actual position with respect to the robot is greatly simplified.

To accomplish this task, the *Planner* informs the *Scheduler* that the current path segment penetrates a door opening and provides the estimated bearing and distance to the door. The *Scheduler* rotates the head to this bearing (typically straight ahead), thus pointing the long-range near-infrared proximity sensor (Figure 16-11) at the center of the anticipated passage. Unless the robot is significantly misaligned due to accumulated dead-reckoning errors, the proximity sensor will return a "no target" condition, as it should be looking through the open doorway. If this is not the case, the head begins scanning 15 degrees either side of centerline in an attempt to find the opening. If this search fails to locate the doorway, an error condition is returned informing the *Planner* that the robot is either significantly lost to where the door penetration routine won't work, or the door is closed.

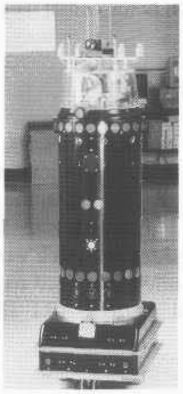

Figure 16-11. ROBART II searches for the door opening using the head-mounted programmable near-infrared proximity detector discussed in Chapter 7 (courtesy Naval Command Control and Ocean Surveillance Center).

Assuming the opening is detected, the *Scheduler* next attempts to locate the left and right edges by panning the head and watching the proximity sensor output for a "target" condition, indicative of energy being reflected from the door casings (see doorway detail, Figure 16-12) and adjacent wall areas to either side. Head position angles corresponding to the left and right boundaries are then averaged to yield a relative bearing to the actual center of the doorway.

The *Scheduler* alters the robot's heading to be coincident with this bearing and begins looking at the sonar data from the center five transducers in the *collision avoidance array* for range confirmation. Measured distance to the door should be within a specified tolerance of the estimated range provided earlier by the *Planner*, less distance traveled in the interim, otherwise another error condition is returned. If the robot is more than 5 feet from the doorway, the center three transducers should all indicate ranges within this window of acceptance.

As the robot closes on the doorway, the beam from the center transducer should eventually break through the opening, with a corresponding increase in range to target. This occurs at the point where the effective beamwidth at the indicated distance becomes less than the width of the doorway, assuming the robot is perfectly aligned with the center of the opening. (Perfect alignment is typically not the case, however, resulting in a slight delay as the beam narrows further on approach, before the jump in range is observed.)

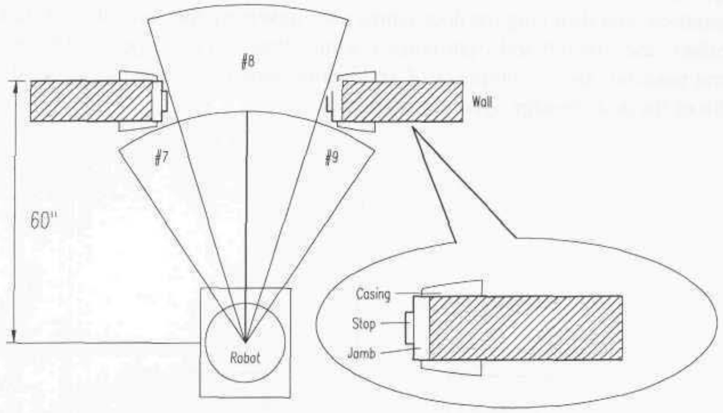

Figure 16-12. Energy is reflected from the left and right door casings, but the center beam (#8) penetrates the door opening at a distance of about 5 feet.

It may appear the robot's alignment with the doorway could be calculated in advance at a distance of approximately 4 feet by simply comparing the range returns from transducers #7 and #9, but this method turns out to be unreliable due to the possibility of furniture or other objects on either side of the door interfering with the beam. In addition, doorways are sometimes placed in the corner of a room in close proximity to an adjoining wall, which will interfere with the sonar readings on that particular side. For this reason, it was found necessary to let the robot get very close to the opening as discussed above before assessing alignment.

At the instant the center beam penetrates the opening, the two adjoining beams from transducers #7 and #9 should by virtue of their orientation in the array be directed at the left and right door casings, as shown in Figure 16-12. The respective range readings from these two transducers at this point should again be consistent with the previously estimated range to the doorway, until such time as the indicated ranges decrease to around 36 inches, whereupon these beams should break through the opening, as shown in Figure 16-13. If either of these ranges decreases below 12 inches prior to penetration, the robot is likely to impact the side of the door, and the *Scheduler* will have to execute a corrective maneuver to attain better alignment.

The next step in the procedure calls for deriving *X-Y* positional data while passing through the door opening. The most obvious solution for the transverse fix is to ping the two side-looking transducers in the upper *navigational sonar array* at the left and right door jambs; the only difficulty here would be knowing exactly when to ping. One solution might be to ping continuously during transit, and then use the minimum range value thus obtained. An alternative approach would be to estimate the distance to the center of the opening from the last set of range values measured by *collision avoidance* transducers #7 and #9 just prior to penetration, and then ping the door jambs after traversing that amount of distance. In either case, the left and right range readings thus obtained specify the robot's lateral position, and for purposes of verification should add together to yield the width of the door passage, typically 36 inches.

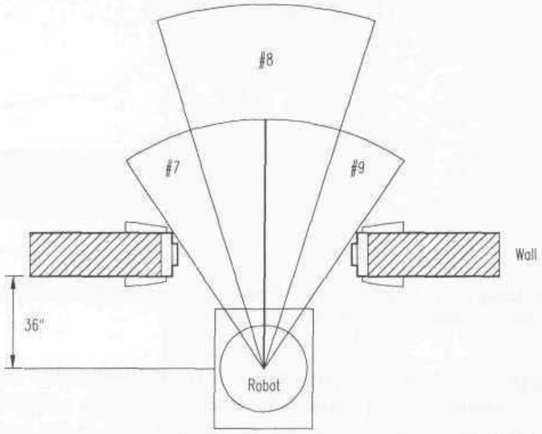

Figure 16-13. As the robot closes on a 36-inch doorway, all three sonar beams should penetrate the opening at approximately 3 feet.

The task of obtaining a longitudinal fix during doorway transit is a little more difficult. The longitudinal fix could be derived from the last set of readings obtained by the forward-looking sonar transducers mentioned above, but the accuracy would be somewhat suspect. Alternatively, if the transverse fix discussed above is obtained by successive pinging of the casings, then postanalysis of the data should yield a door edge profile in the sense that ranges to either side will decrease to some minimum upon entry, remain at that minimum plus or minus some tolerance value for a finite length of time proportional to the width of the jamb (thickness of the wall), and then increase. The midpoint of this period of minimum ranges would then correspond to the midpoint of the door jamb width (centerline of the wall), which is of course the desired longitudinal fix.

Both of the above solutions, however, assume an ideal door opening in the center of an unobstructed wall and will suffer significantly from the presence of objects near the open doorway, not the least of which might be the door itself. (When in the open position, the door folds back to one side, adding several inches in projected target surface that will interfere with the ranging process.) This is primarily due to problems associated with specular reflection and beam divergence in the ultrasonic rangefinders employed. Diffuse-mode near-infrared proximity sensors are often employed in an effort to compensate for some of the limitations in ultrasonic systems, in that the beams can be tightly focused, and specular reflection is less significant due to the shorter wavelengths involved (Banner Engineering, 1993a, 1993b). This type of proximity sensor provides no range measurement capability, however, other than that which can be inferred from the strength of returning energy, which varies as a function of target reflectivity (Chapter 3).

If the sensors are mounted on the robot so as to be orthogonal to the direction of travel, however, they could be used to detect the leading edge of the door casing as the robot passed through the opening. As shown in Figure 16-14, the elapsed time between target detection by sensors mounted on either side of the robot also could be used to calculate the angular orientation of the robot with respect to the doorway, in accordance with the following formula:

$$\sin\theta = \frac{vt}{d}$$

where:

θ = angular orientation
v = velocity of robot
t = elapsed time between detections
d = target separation distance.

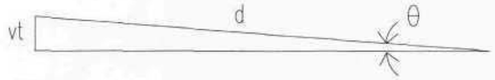

Figure 16-14. Elapsed time between doorway-overhead detection by left and right proximity sensor pairs can be used to calculate heading.

To achieve any useful accuracy in deriving the heading of the robot in this fashion, however, the following conditions must apply:

- The sensors must be rigidly mounted to retain their orthogonal relationship to the robot.
- The sensors must have well defined narrow beams.
- The excess gain must be sufficiently high to ensure rapid detection as the targets move into view.
- The time between left and right target detection must be accurately measured.
- The robot's heading must remain constant for this period.

- The distance traveled by the robot during this period must be accurately measured.
- The targets must stand out clearly from their respective backgrounds with no ambiguity.
- The lateral separation *d* between targets must be known in advance or measurable during transit.

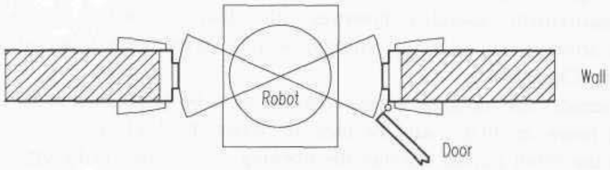

Figure 16-15. The door stops as well as the actual door can interfere with the ranging process (Everett, et al., 1990).

The first six conditions outlined above are easily met, but the latter two pose a problem. As previously discussed, objects on either side of the doorway can effectively mask the location of the door casing to make accurate leading-edge detection impossible. One way around this would be to apply strips of retroreflective tape to the door casings to create cooperative targets, and reduce the gain of the proximity sensors to where only these strips triggered a detection.

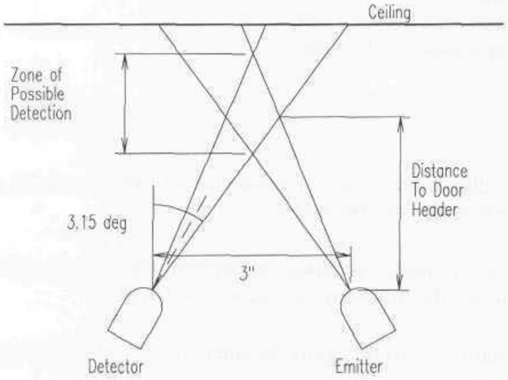

Figure 16-16. Objects (such as the ceiling) outside the zone of possible detection will be ignored by an emitter/detector pair configured in convergent mode.

The use of retroreflective tape, however, requires the environment be modified to accommodate the robot, which is not in keeping with the objective of using existing (unmodified) doorways as navigational aids. Such strips are somewhat obtrusive and distracting to humans and can be accidentally removed or painted over by maintenance crews. In addition, setting the detection threshold of the sensors to respond only to the retroreflective strips violates the requirement for high excess gain. In reality, the critical threshold setting required is likely to be impossible to achieve under dynamic real-world conditions. The robot may pass through the opening closer to one side than the other, and the distances involved can vary as well due to different doorway widths ranging anywhere from 30 inches to 72 inches or more.

Even if the leading edges could be precisely detected, ambiguities arise in measuring the distance between the actual locations of the left and right targets using ultrasonic ranging techniques. Referring to Figure 16-15, we see that both the door stops as well as the actual door itself can interfere with the ranging process. The resulting measurement accuracy, although acceptable for determining the lateral position of the robot in the doorway, would be insufficient for the desired final resolution in heading.

One solution to these problems is to reorient the proximity sensors to where the beams are vertical as opposed to horizontal, yet still orthogonal to the direction of robot motion. The target separation distance is thus a constant, precisely determined by and equal to the sensor displacement *d* on board the robot, eliminating one of the above concerns altogether. The upper door casing now becomes the target, where there is much less possibility of obstructions being present that might interfere with leading-edge detection. To further address this issue, the proximity sensors can be configured in the *convergent mode* as opposed to *diffuse mode*, taking advantage of the fact that the distance to the overhead casing will be fairly constant, regardless of the path followed by the robot through the doorway. (Standard door height is 80 inches.) This means objects (such as a ceiling or overhead light fixture) outside of the zone of potential detection will be ignored as illustrated in Figure 16-16, allowing for even greater excess gain to be employed.

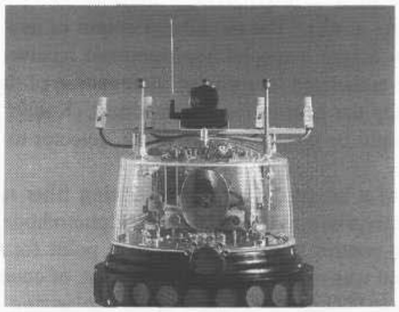

Figure 16-17. Two Banner emitter/detector pairs arranged on either side of the robot's head are used to detect passage under an overhead door frame.

A photo of this overhead doorway-detection configuration as installed on ROBART II is provided in Figure 16-17. The emitter and detector units are Banner models *SM31EL* and *SM31RL*, respectively (Banner, 1993a). These near-infrared sensors are normally intended to be operated in the *break-beam mode* (see Chapter 3) at distances out to 100 feet but were found to effectively detect diffuse target surfaces at a nominal sense range of 40 inches when arranged in the *convergent mode*.

16.3 Ceiling Referencing

One obvious disadvantage of a navigational strategy that depends primarily on dynamic wall referencing to control accumulated errors is the inability of the system to operate in unstructured scenarios that do not provide sufficient access to appropriate wall structures. A good example is seen in the case of the MDARS Interior robot that patrols primarily in warehouse environments, where walls exist only along the outer perimeter of the building and are typically obscured even there by stored materials (Gage, et al., 1995). Similarly, warehouse environments are generally devoid of internal doorway structures, at least to the extent such would be found in an office building of equivalent square footage. Almost all buildings, however, are fairly consistent from the standpoint of unobstructed ceiling access, opening up distinct possibilities for a number of overhead referencing strategies.

16.3.1 Polarized Optical Heading Reference

One of the initial concepts considered in the development of ROBART II as a heading update mechanism called for placement of a number of active beacons on the ceiling above the robot's operating area. These modulated near-infrared sources were to be fitted with polarizing filters of known angular origin (i.e., referenced to building north). The modulated output of any one of these sources would automatically trigger a special head-mounted receiver whenever the robot traversed within the associated footprint of illumination of the source. An optical filter that passed only the near-infrared component (Kodak Wratten 89B) of the incoming energy would be placed in front of the detector to minimize the effects of ambient lighting.

Upon detection of a beacon, a second polarizing filter mounted on the robot (just above the receiver's upward-looking PIN photodiode detector) would be rotated under servo control to ascertain the null point for which the minimum receiver output signal was observed. This null point, of course, would be directly related to the pre-established orientation of the polarizing filter on the source. There is somewhat of an ambiguity in this proposed scheme since there would exist two null positions, 180 degrees apart, corresponding to when the polarizing gratings of the two filters were made orthogonal to one another. This ambiguity was to be resolved by choosing that null position most closely in agreement with the robot's fluxgate compass heading.

It was speculated the ceiling mounted sources could be modulated in such a way as to be uniquely identifiable to the robot, thus allowing them to serve double duty as lateral position markers. This enhancement, however, would require the PIN photodiode to be replaced by a suitable two-axis position sensitive detector or CCD array. Rathbone, et al. (1986) proposed a similar system for AGV guidance that would employ an upward-looking imaging sensor able to positively identify and track a number of specifically coded near-infrared LED beacons mounted on the ceiling. This polarized heading reference concept was never seriously pursued due to the desire to avoid modifying the robot's environment to accommodate the needs of the navigation system, and the less than elegant requirement to mechanically servo the angular orientation of the polarizing filter at the detector.

16.3.2 Georgia Tech Ceiling Referencing System

A more robust ceiling referencing scheme employing an upward-looking digital camera was implemented about this same time frame by researchers at the Material Handling Research Center at Georgia Tech, for use in free-ranging AGV navigation (Holcombe, et al., 1988; Bohlander, et al., 1989). In addition, the Georgia Tech approach significantly reduced required installation costs through the use of passive landmarks instead of active-emitter targets (Figure 16-18).

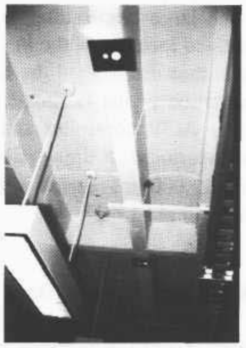

Figure 16-18. Asymmetrical retroreflective targets of known orientation and location serve as passive overhead markers for the *Landmark Tracking Camera System* (courtesy Georgia Institute of Technology).

A number of identical retroreflectors were mounted at known locations and orientations on the ceiling of the laboratory environment, approximately 5 meters apart. The *Landmark Tracking Camera System* (Figure 16-19) employed a xenon strobe to illuminate the overhead targets for subsequent detection by an 8192-pixel digital-RAM camera interfaced directly to an 8-bit *6500*-series microprocessor. The asymmetrical targets consisted of two different-diameter circles made of retroreflective paper affixed to a piece of black cardboard. Since the cooperative targets had a significantly higher reflectivity than the surrounding background, the camera threshold could be adjusted to eliminate everything except the desired circular targets from the binary image, thereby substantially reducing the amount of required processing (Holcombe, et al., 1988).

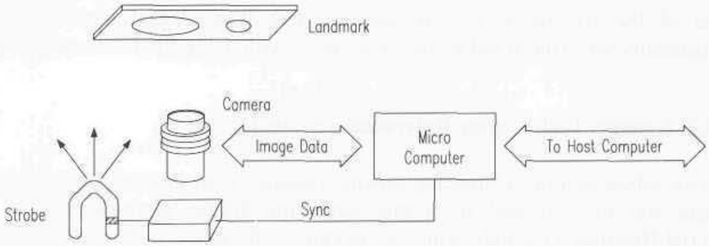

Figure 16-19. A xenon flash was used to illuminate the retroreflective landmark for subsequent detection by a binary digital-RAM camera (adapted from Holcombe, et al., 1988).

The *first moments* were calculated from the captured video data to find the centroid of the landmark, which was intentionally located within the diameter of the larger circle. An edge-finding operation was then performed (starting at the centroid location) to bound the large circle, after which the circle centerpoint could be calculated. The perceived location of the landmark centroid with respect to the center of the larger circle thus established the landmark's orientation. The relative *X-Y* location and orientation of the landmark as computed by the vision system was then passed to the AGV controller and integrated with odometry position estimates using an aperiodic Kalman filter. Experimental testing involving the collection of over 12,000 images showed the 3-σ position error to be less than 0.09 inches (Holcombe, et al., 1988).

16.3.3 TRC *HelpMate* Ceiling Referencing System

Transitions Research Corporation (TRC) employs a vision-based navigational referencing system on their *HelpMate* robot to determine platform lateral offset and heading from the known orientation of overhead lights (Krishnamurthy, et al., 1988; King & Weiman, 1990). In office buildings and hospitals, for example, such lighting fixtures are generally rectangular in nature and aligned parallel to the longitudinal axis of hallways and corridors. By thresholding the image and performing a series of edge-detect operations, the left and right boundaries of a light fixture can be reliably established. After first locating the light closest to the robot (i.e., at the top of the video image), the operation is repeated to identify a second light further down the hall. The left and right boundaries of the two lights are then extended to find their point of intersection on the horizon, known as the *vanishing point*.

The *HelpMate* vision system consists of an *80386*-based PC/AT computer, an associated frame grabber, and a forward-looking CCD camera tilted upward from the horizontal at some preset angle of pitch ϕ. The origin of the sensor's Cartesian coordinate system (depicted in Figure 16-20) is the midpoint of the scan line associated with the optical axis of the camera. The *vanishing point* is determined to be at pixel coordinates (i, j), where the extended centerline of the perceived light pattern also intersects the horizon. From this pixel information, the tangent components (u, v) of the vanishing point can be calculated, given the physical dimensions of the camera sensor and the focal length of the lens. The robot's heading θ (with respect to the perceived longitudinal axis of the light fixtures) can then be calculated as follows (King & Weiman, 1990):

$$\theta = \arctan(u \cos\phi)$$

where:

θ = relative heading of the robot
u = measured lateral offset to vanishing point
ϕ = camera pitch angle (fixed) with respect to horizontal.

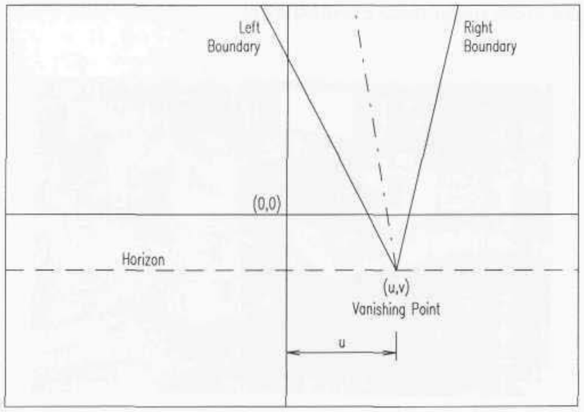

Figure 16-20. The lateral displacement *u* from the origin (in camera coordinates) of the *vanishing point* defined by the intersection of the perceived light centerline and the horizon determines the heading of the robot (adapted from King & Weiman, 1990).

If the vertical distance between the camera and the overhead lights is known in advance (or measured by sonar), the robot's lateral offset can also be calculated as follows (King & Weiman, 1990):

$$x_o = -\frac{c\cos\theta}{m\cos\phi} - \frac{c\sin\phi\sin\theta}{\cos\phi}$$

where:

x_o = lateral displacement of the robot from centerline of ceiling lights
c = vertical distance from camera to lights
m = slope of perceived centerline in camera coordinates.

16.3.4 MDARS Overhead-Beam Referencing System

An overhead vision system that combines elements of the Georgia Tech prototype and the doorway penetration system used on ROBART II is under consideration to support autonomous operation of the MDARS Interior robot in completely unstructured warehouse scenarios (Figure 16-21). The lack of definitive rack structures coupled with constantly changing load-out conditions encountered in bulk-storage facilities of this type poses a significant navigational challenge. While the intended aisleways may be predefined and in some cases even marked with paint stripes on the floor, there is no repeatability to the sonar profile created by the stored items. In fact, when portions of the warehouse are temporarily depleted of stock, there very likely is no target surface at all within the sensor's effective range. *Wall-following* and *wall-approach* re-referencing techniques clearly do not apply under these circumstances.

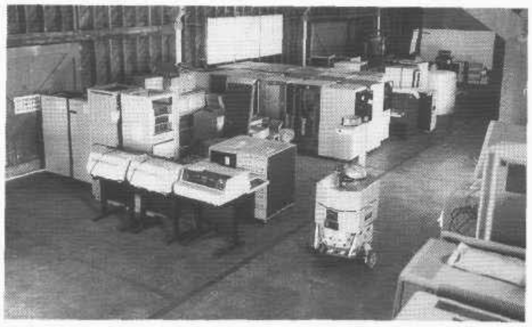

Figure 16-21. Lack of definitive walls or rack structures in bulk-storage facilities pose a significant navigational challenge (courtesy Naval Command Control and Ocean Surveillance Center).

As a consequence, an overhead optical referencing system is thought to be the only practical near-term solution to the needs of unstructured warehouse navigation. Since ceiling heights may vary anywhere from 10 to 60 feet or more, the higher resolution of a CCD-array camera was chosen over a more simplistic active near-infrared retroreflective proximity detector. To simplify the image-processing requirements, the overhead targets would consist of identical sections of 1-inch-wide retroreflective tape several feet in length. The tape sections would be attached to the underside of the roof-support rafters running perpendicular to the path of travel and actively illuminated by a strobe when the robot was in approximate position directly below. As in the case of the Georgia Tech system, the camera iris would be stopped down to eliminate all background returns other than the reflective tape itself.

The length of the installed tape segments would be chosen in conjunction with the fixed field of view of the camera and the local ceiling height to meet the following criteria:

- At least 50 percent of the tape segment is within the camera's horizontal field of view from any possible lateral position of the robot on the path below.
- The total length of the tape segment is slightly shorter than the full horizontal field of view of the camera.

The first requirement ensures there is sufficient length to the detected target image to adequately determine the slope of the line, and hence the platform heading. The second criteria guarantees detection of a tape end point, from which the robot's lateral position can be calculated.

16.4 References

Banner, *Photoelectric Controls*, Product Catalog, Banner Engineering Corp., Minneapolis, MN, 1993a.

Banner, *Handbook of Photoelectric Sensing*, Banner Engineering Corp., Minneapolis, MN, 1993b.

Bohlander, R.A., Holcombe, W.D., Larsen, J.W., "An Advanced AGVS Control System: An Example of Integrated Design and Control," Material Handling Research Center, Georgia Institute of Technology, Atlanta, GA, 1989.

Devore, J. L., *Probability & Statistices for Engineering and the Sciences*, pp. 422-436, Brooks/Cole Publishing Company, 1982.

Everett, H.R., "Survey of Collision Avoidance and Ranging Sensors for Mobile Robots," Technical Report No. 1194, Naval Command Control and Ocean Surveillance Center, San Diego, CA, 29 March, 1988.

Everett, H.R., Gilbreath, G.A., Tran, T., Nieusma, J.M., "Modeling the Environment of a Mobile Security Robot," Technical Document 1835, Naval

Command Control and Ocean Surveillance Center, San Diego, CA, June, 1990.

Gage, D.W., Everett, H.R., Laird, R.T., Heath-Pastore, T.A., "Navigating Multiple Robots in Semi-Structured Environments," ANS 6th Topical Meeting on Robotics and Remote Systems, Monterey, CA, February, 1995.

Holcombe, W.D., Dickerson, S.L., Larsen, J.W., Bohlander, R.A., "Advances in Guidance Systems for Industrial Automated Guided Vehicles," SPIE Vol. 1007, Mobile Robots III, Cambridge, MA, November, 1988.

Holland, J.M., Everett, H.R., Gilbreath, G.A., "Hybrid Navigational Control Scheme, SPIE Vol. 1388, Mobile Robots V, Boston, MA, November, 1990.

Holland, J.M., "An Army of Robots Roams the Night," International Robot and Vision Automation Show and Conference, Detroit, MI, pp. 17.1-17.12, April, 1993.

Kadonoff, Mark B., "Ultrasonic Wall-Following Controller For Mobile Robots", Mobile Robots IV, W.J. Wolfe, W.H. Chun, Editors, Proc. SPIE 1195, pp. 391-401, 1990.

King, S.J., Weiman, C.F.R., "HelpMate Autonomous Mobile Robot Navigation System," SPIE Vol. 1388, Mobile Robots V, Boston, MA, pp. 190-198, November, 1990.

Krishnamurthy, B., Barrows, B., King, S., Skewis, T., Pong, W., Weiman, C., "HelpMate: a Mobile Robot for Transport Applications," SPIE Vol. 1007, Mobile Robots III, Cambridge, MA, pp. 314-320, November, 1988.

Rathbone, R.R., Valley, R.A., Kindlmann, P.J., "Beacon-Referenced Dead Reckoning: A Versatile Guidance System", *Robotics Engineering*, December, 1986.

17

Application-Specific Mission Sensors

The ultimate goal of an autonomous robotic system is, of course, to perform some useful function in place of its human counterpart. Some of the more common applications currently being pursued include:

- Material handling (King & Weiman, 1990; MacLeod & Chiarella, 1993; Mattaboni, 1994).
- Floor cleaning (Bancroft, 1994).
- Physical security (Everett, 1988; George, 1992; Holland, 1993; Gage, et al., 1995).
- Inventory management (ISRA, 1994; Gage, et al., 1995).
- Nuclear and hazardous waste inspection (Byler, 1993; Heckendorn, et al., 1993).

The last three of these categories are probably the more interesting from the standpoint of their mission-specific sensing needs. To reasonably bound the discussion in keeping with the illustrative intent of this chapter, we will examine in detail only those two scenarios being addressed under the ongoing MDARS program: 1) physical security and 2) automated inventory assessment.

17.1 The Security Application

One of the earliest perceived applications for an autonomous mobile robot was acting as an intelligent sentry or security guard. Numerous sensors are readily available to support the detection functions (i.e., fire, smoke, intrusion, toxic gas, flooding, radiation). The ability to maintain an effective security presence under adverse (severe weather, degraded visibility) or even hazardous (nuclear, chemical, and biological) conditions is important, and therefore appropriately addressed by robotic systems. Reliable detection of intruders involves discrimination from background conditions of some property or properties unique to the presence or motion of a human, with sufficient signal-to-noise ratio to minimize the occurrence of nuisance alarms.

Security sensors of this type generally are classified either as *presence sensors*, which can detect a motionless body, or *motion sensors*, which require the intruder to move before detection is possible. A robust solution generally involves evaluation of more than just a single attribute, such as for example:

- Target motion.
- Thermal signature.
- Aspect ratio.
- Temporal history.

Passive detectors for the most part sense a change in ambient conditions due to movement or presence of an intruder within their field of view. This change could be associated with the observed level of illumination, thermal energy, noise, or even vibration normally present in an unoccupied space. *Active detectors* provide a controlled energy input into the observed environment, reacting to changes with respect to a monitored reference as caused by perturbations within the area of coverage. For this reason, active detectors can sometimes be tailored to provide more sensitivity or selectivity in a specific situation.

17.1.1 Acoustical Detection

A simple form of passive detection capability intended primarily for indoor scenarios can be illustrated by the use of a microphone that allows the system to "listen" for sounds in the protected area. Figure 17-1 shows the circuitry employed on ROBART II; an automatic gain control feature in the amplifier stage adjusts to ambient conditions, and any subsequent increase in signal level is detected by the *LM-339* comparator.

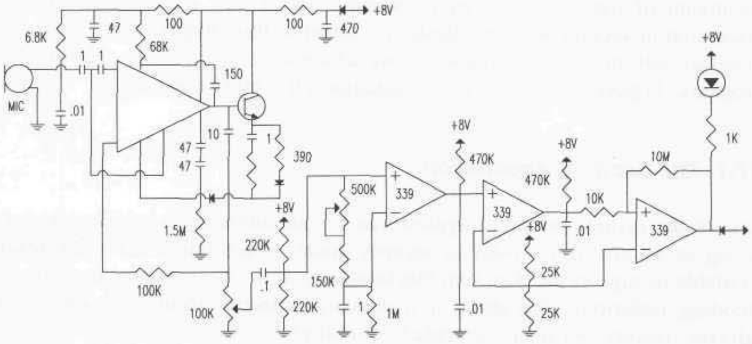

Figure 17-1. Schematic diagram of the acoustical amplifier circuitry used on ROBART II (Everett, et al., 1990).

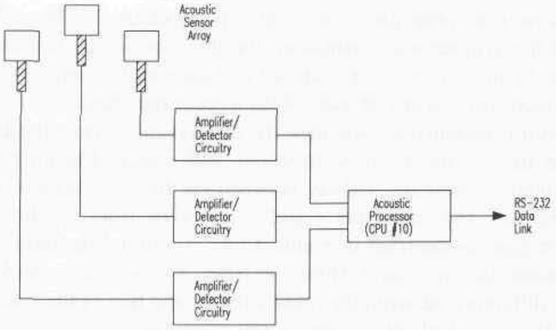

Figure 17-2. Block diagram of the *Acoustic Detection Array* used to passively determine a relative bearing to the source of a detected disturbance.

A three-channel *acoustic detection array* intended to provide bearing information to the source of detected noise was developed using the circuitry presented in Figure 17-1. The sensor array consists of three omni-directional microphones symmetrically oriented 120 degrees apart and separated by a distance *d*. The system will calculate a bearing to a sudden acoustical disturbance when the sound travels across the array and triggers the microphones in a specific sequence, the exact order being dependent on the relative position of the source. A block diagram of the system is presented in Figure 17-2.

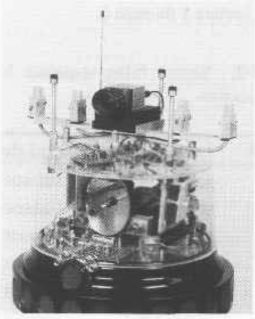

Figure 17-3. Three omni-directional microphones situated 120 degrees apart form a passive *acoustic detection array* that can localize the source of a perceived disturbance (courtesy Naval Command Control and Ocean Surveillance Center).

The array is mounted on top of ROBART II as shown in Figure 17-3, with the three transducers individually supported by coil springs. The springs provide some degree of acoustical isolation, while raising the transducers to yield a clear path for wavefront propagation without any blockage by the video camera. Because of the symmetrical orientation, the direction of the disturbance can be classified as being in one of six sectors by examining the detection sequence of the comparators associated with each of the three audio channels.

Each sector is bounded by two lines, the first extending from the array center *O* through the first sensor S_i, to be triggered, and a second originating at *O* and passing through a point B_{xy} midway between the first two sensors detecting the incoming noise. The subscripts *x* and *y* are taken from the first and second sensors to trigger, as depicted in Figure 17-4. Assuming the intruder (source of sound) is some distance away from the robot when initially detected, we can neglect the difference between the robot's height and that of the source with little adverse effect on resultant accuracy, and consider all derivations in a two-dimensional plane. Table 17-1 lists the detection-sequence information for each sector.

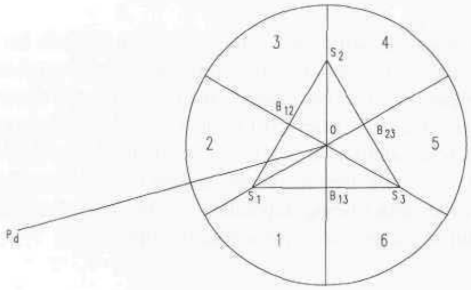

Figure 17-4. Diagram illustrating the relationship in the horizontal plane for acoustic sensors S_1, S_2, and S_3, and the corresponding sectors 1 through 6.

Table 17-1. Sensor firing sequence for the six potential sectors.

Sector #	1st detection	2nd detection
1	sensor #1	sensor #3
2	sensor #1	sensor #2
3	sensor #2	sensor #1
4	sensor #2	sensor #3
5	sensor #3	sensor #2
6	sensor #3	sensor #1

The individual sensor outputs are active low, with a negative transition triggered by the arrival of an incoming noise. Referring to Figure 17-5, the time delay T_1 (between first and second firings) and delay T_2 (between second and third firings) can be measured in order to determine the angle to the source. In keeping with the previously stated assumption that the intruder is some distance away from the sensors when first detected, wavefront propagation can be simplistically modeled as parallel lines perpendicular to a line extending from the array center *O* to the source of the detected disturbance at P_d. In addition, the speed of sound in air is assumed to be constant over the region of travel involved. For each sector, therefore, it is possible to calculate a bearing to the perceived location of the source, relative to the line segments $OB_{xy}(O_i)$ and to $OS_{xy}(O_i)$. Details of the derivation are provided by Tran (Everett, et al., 1990).

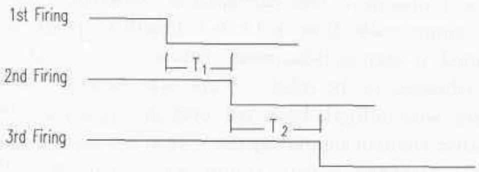

Figure 17-5. The relationship between time delays T_1 and T_2 is used to calculate the bearing to the perceived source.

While the *acoustic detection array* used on ROBART II was very effective in detecting impulse-type disturbances and involved less than $100 worth of hardware, it was completely insensitive to gradually increasing or steady-state noise. A much more sophisticated capability is seen in the *Integrated Acoustic Sensor* system employed on the Surrogate Teleoperated Vehicle (STV) presented in Chapter 1. Developed by SAIC Bio-Dynamics, Eugene, OR, the passive system is designed to alert the remote STV operator to approaching vehicles by detecting the low-frequency sounds of the engine (RST, 1993). The software first establishes a background acoustical signature during power-on initialization and then signals an alarm if the monitored noise level increases above the background threshold in four frequency bands (1-2 KHz, 2-4 KHz, 4-8 KHz, and 8-16 KHz).

Figure 17-6. The *Surrogate Teleoperated Vehicle (STV)* developed by Robotic Systems Technologies employs a 360-degree acoustical sensing array (top-left of mast) manufactured by SAIC Bio-Dynamics (courtesy Naval Command Control and Ocean Surveillance Center).

17.1.2 Vibration Sensors

Vibration sensors are commonly employed as motion detectors in automotive security systems and as window-breakage sensors in fixed-installation alarms. When deployed on a mobile security platform, such devices are usually mechanically coupled to the floor through wheel contact to detect structural vibrations due to footsteps or even earthquakes. ROBART I was equipped with a sensor of this nature made from a 12-inch length of piano wire enclosed in a vertically oriented quarter-inch-diameter section of brass tubing (Everett, 1982a; 1982b). Any vibration of the robot's frame was directly coupled to the tubing, causing the piano wire to jiggle back and forth, generating an electrical signal in a piezoelectric sense element supporting the wire at the bottom of the tube.

Mims (1987) describes a very simple and much more elegant fiber-optic vibration sensor, consisting of a phototransistor that monitors the light output from a short cantilevered length of plastic fiber attached to an LED emitter (Figure 17-7). Any transverse vibration of the housing assembly causes the free end of the fiber to be displaced in alignment from the optical axis of the phototransistor, with a subsequent reduction in light-coupling efficiency. As a consequence, the output signal from the detector is modulated in amplitude at the frequency of the applied vibration. A variation of this vibration sensing technique was incorporated on ROBART II for static security monitoring, in view of its inherent simplicity, low cost, and high output-signal amplitude.

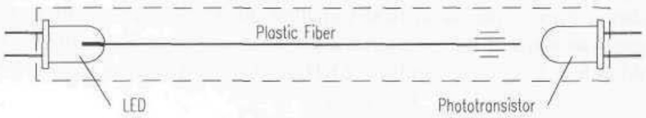

Figure 17-7. The active element in this inexpensive vibration sensor is a cantilevered length of plastic fiber cemented into a small hole in the epoxy housing of an ordinary LED (adapted from Mims, 1987).

17.1.3 Ultrasonic Presence Sensors

The *ultrasonic presence detection* system used on both ROBART II and the ModBot identifies a potential intrusion through changes in measured target distances as seen by one or more sensors in the 24-element *navigational sonar array*. The system creates a reference template consisting of the two most frequently observed range values for each of the individual transducers in the array and then compares subsequent readings to this template. The presence of an intruder within the field of view results in a range value that does not agree with the two possibilities recorded earlier in the reference template. The new range reading corresponds to the distance to the intruder, and the index (position) of the affected sensor within the 360-degree array provides a relative bearing, both of which are used by the host computer to plot the position of the suspected intruder on the map display.

17.1.4 Optical Motion Detection

The Sprague *D-1072* optical motion detector used on ROBART I responds to changes in perceived light level, incorporating a built-in lens to create a cone-shaped detection field (Weiss, 1979; Gontowski, 1983). After a brief settling period upon power-up, the circuit adjusts itself to ambient conditions, and any subsequent deviations from that setpoint will result in an alarm output. The low cost and directional nature of the device allow for several to be used collectively in an array to establish unique detection zones that help locate the relative position of the suspected security violation. The ability to provide geometric resolution of the intruder's position can be invaluable in tailoring an appropriate response in minimal time.

The *D-1072* optical motion detector suffered from three significant drawbacks that limited its utility and contributed to eventual discontinuation: 1) the current consumption of the device was fairly large, 2) it was susceptible to nuisance alarms, and 3) it responded only to visible light. The fact that the chip was incapable of sensing in the near-infrared region of the optical spectrum meant an intruder using an active night-vision device would not trigger an alarm even if the high-power source were pointed directly at the sensor. Interestingly, there are no systems in place even today at most high-security facilities employing elaborate automated equipment to warn guards the area is being illuminated by near-infrared energy.

For this reason, ROBART II was equipped with a dual-element optical motion detector designed specifically for scenarios in which the guarded installation could be under observation by potential intruders armed with a night-vision device employing a near-infrared source. The output of a cadmium-sulfide photosensor (sensitive only to visible light) is compared to an integrated lagging reference voltage derived from the same sensor, such that any change in scene intensity above a specified threshold will be detected. An identical circuit monitors the output of a silicon photosensor shielded by a near-infrared optical filter.

Simultaneous examination of the output states of both circuits reveals the type of lighting involved when motion is sensed (i.e., near-infrared, fluorescent, or incandescent). Fluorescent and incandescent light both produce energy in the visible-light portion of the energy spectrum and will activate the cadmium-sulfide detector, which is not sensitive to near-infrared. Incandescent and near-infrared sources will penetrate the optical filter to activate the broadband silicon detector, but the fluorescent source will be blocked. The following truth table applies:

Table 17-2. Sensed energy derived from detector status.

Activated detector	Sensed energy
Cadmium-sulfide	Fluorescent
Silicon	Near-infrared
Both	Incandescent

17.1.5 Passive Infrared Motion Detection

A significant development in security sensor technology is seen in the *passive infrared (PIR)* motion detector. Originally designed for both indoor and outdoor fixed-installation security systems, this type of *pyroelectric sensor* quickly found application on mobile robots due to its small size, low power consumption, and excellent performance and reliability characteristics (Everett, 1982a; 1982b; Quick, 1984). *PIRs* routinely exhibit remarkably low nuisance-alarm rates in indoor environments but can sometimes be triggered by gusty wind conditions when employed outdoors. The principle of operation as a motion detector is similar to the optical sensor described in the previous section, except a different range of wavelengths (7-16 micrometers) in the energy spectrum is being sensed.

Recall from Chapter 9 all objects with an absolute temperature above 0°K emit radiant energy in accordance with the Stephan-Boltzman equation (Buschling, 1994):

$$W = \varepsilon \sigma T^4$$

where:

W = emitted energy
ε = emissivity
σ = Stephan-Boltzman constant (5.67×10^{-12} watts/cm^{2}K^4)
T = absolute temperature of object in degrees Kelvin.

The *emissivity* of human skin is very close to unity (0.98) and the same for all races (Cima, 1984). A typical human gives off somewhere between 80 and 100 watts of radiant energy with a peak wavelength around 10 micrometers (Cima, 1990), thus producing a distinctive thermal signature.

Ordinary glass is 100-percent opaque at wavelengths longer than 5 micrometers, and therefore useless as a lens or window material for this application (Barron, 1992). Early *PIR* detectors (such as the unit used on ROBART I) employed fairly expensive germanium or zinc-selendide lenses, but more recent devices take advantage of high-density polyethylene Fresnel lenses, which are 60- to 80-percent transmissive at the wavelengths of interest. Fresnel lenses provide an equivalent degree of refraction in a much thinner package than conventional lenses, due to the discretized nature of their construction, and therefore absorb much less infrared radiation (Viggh & Flynn, 1988). An optical filter between the lens and sensing element restricts the admitted wavelengths to the region associated with human emission (i.e., 7-16 micrometers).

Typical *pyroelectric sensing elements* are thin-wafer slices of either lithium tantalate (Cima, 1984), ceramic (Philips, 1985), or polymer film (Tom, 1994) materials, with metallic electrodes deposited on opposite faces. The so-called *pyroelectric effect* arises due to thermally induced changes in polarization of the wafer or film (Philips, 1985). Incident photons absorbed by an exposed face heat the sandwiched material, generating a small charge that is in turn collected by the electrodes (Cima, 1984). The sense elements are made as thin as possible to minimize their thermal inertia for improved dynamic response.

Pyroelectric detectors can be thought of as "self-generating capacitors" (Eltec, 1993), with the voltage differential across the sense element given by (Philips, 1985):

$$v = \frac{Q}{C}$$

where:

v = voltage developed across the electrodes
Q = induced charge due to pyroelectric effect
C = effective capacitance of the detector.

As discussed in Chapter 11, current leakage paths in the sensor and associated electronics cause the voltage generated across the capacitive element to decay with time (Russell, 1993), and so the output is really proportional to the *change* in incident radiation. The pyroelectric sensor thus functions normally as a *motion detector* and not a *presence detector*.

In conventional security applications, the device is mounted such that the sense element "stares" at a stable thermal field of view and responds only when a moving entity disturbs the magnitude and distribution of incident photons (Cima, 1984). Most commercially available systems incorporate opposed-output dual-element detectors that provide common-mode rejection of global disturbances (Figure 17-8A), as was briefly discussed in Chapter 11. When a human target moves left to right through the sensor's field of view, the focused concentration of photons in the image plane moves right-to-left across the two detector elements. The lens geometry is such that the incident radiation falls almost exclusively at first on the right-hand detector, reaches a balance between the two as the intruder crosses the optical axis, and then shifts with continued motion to where the left sense element dominates. The resulting output signal is plotted as a function of time in Figure 17-8B. If the "intruder" stops moving at any point while still in view, the detector will settle out to equilibrium with no appreciable output signal.

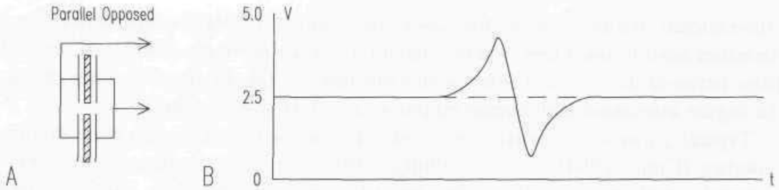

Figure 17-8. A typical output signal (B) of a dual-element detector (A) showing the characteristic rise and fall signature relative to the 2.5-volt equilibrium (adapted from Jones & Flynn, 1993).

Overall device sensitivity can be improved through use of multifaceted lenses that create a number of radial detection zones separated by blind alleys as shown in Figure 17-9A. An intruder moving laterally across these zones will inherently generate a sharp differential signal in the detector when going from a monitored to an unmonitored area, and vice versa (Philips, 1986). Vertical "stacking" of lens sections is often employed to break the foreground and background into different zones (Figure 17-9B), thereby enhancing the probability of detection for an intruder moving radially towards or away from the sensor (Cima, 1984).

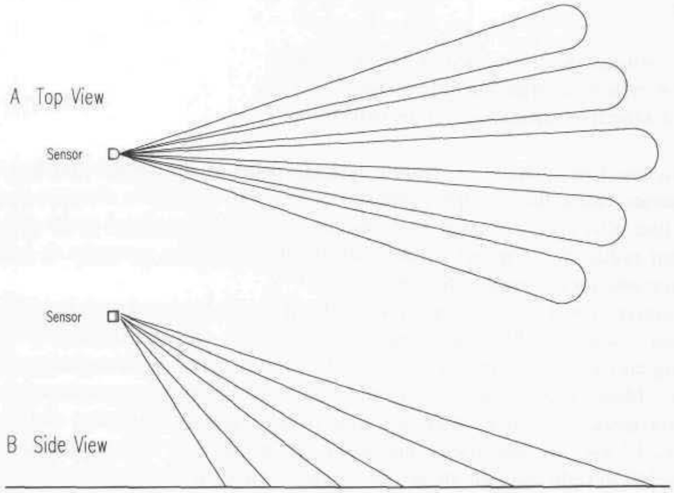

Figure 17-9. Effective coverage areas resulting from a multifaceted lens.

Some security-sensor manufacturers supply special lenses that create a so-called "pet-alley" dead-zone for blocking detection near the floor, in order to minimize nuisance alarms due to the harmless movement of indoor pets. While this approach may work fairly well for dogs, cats routinely aspire to lofty perches from which to survey their domain, and probably become even more adventuresome when their owners are away. "Quad-element" detectors have been introduced in attempts to distinguish among different sizes of stimuli (i.e., small animals versus humans), as part of a growing trend to achieve higher-resolution discrimination at the smart-sensor level (Ademco, 1989; Nippon, undated).

Eltec Instruments, Daytona Beach, FL, produces a 32-element pyroelectric array (Eltec, 1993). Tom (1994) describes a 16-element sensor design based on the *ferroelectric polymer* polyvinylidene fluoride, manufactured by AMP, Inc., Valley Forge, PA. The company's *PIRL180-100* detector incorporates a six-element polymer-film detector with a custom Fresnel lens providing 180-degree coverage divided into 20 discrete beams.

The relative performance of different types of pyroelectric detectors can be reasonably compared using a number of industry-established parameters. The *responsivity* of an IR sensor is defined as the resultant signal voltage per watt of incident radiation (Nippon, undated; Eltec, 1984):

$$R = \frac{V_s}{HA} = \frac{\Gamma}{d\omega\, C_d}$$

where:

R = *responsivity*
V_s = rms value of signal voltage
H = rms value of incident radiation (W/cm^2)
A = active sensor area
Γ = material parameter
d = electrode separation
$\omega = 2\pi f$ (chopping frequency of interrupted input radiation)
C_d = effective capacitance.

Noise equivalent power (NEP) is the radiant flux required to produce an output signal equal in magnitude to the sensor noise (Nippon, undated), or in other words, the *noise* divided by the *responsivity* (Eltec, 1984):

$$NEP = \frac{V_n\, HA}{V_s}$$

where:

NEP = *noise equivalent power* (watts)
V_n = rms value of noise signal.

The ultimate sensitivity of an IR detector is determined by its signal-to-noise ratio (Eltec, 1984). *Detectivity-star (D*)* is a term used to denote the sensor's signal-to-noise ratio when 1 watt of incident radiation falls on a 1-cm^2 sensor, and the noise is measured with a 1-Hz electrical bandwidth (Nippon, undated):

$$D^* = \frac{\sqrt{A\,\Delta f}}{NEP}$$

where:

D^* = detectivity-star
Δf = electrical bandwidth of measuring circuit.

The D^* parameter in effect normalizes the *NEP* to a given constant area for more equivalent comparison of different types of detectors (Eltec, 1984). The absolute temperature T of the blackbody radiation source, chopping frequency f, and electrical bandwidth Δf must be specified for meaningful results. (Standard values are 420°K, 1 Hz, and 1 Hz.) The larger the value of D^* the better.

Eltec *Model 442 IR-EYE* Integrated Sensor

The *Model 442 IR-Eye* pyroelectric sensor manufactured by Eltec Instruments, Inc., Daytona Beach, FL, is a parallel-opposed dual-detector configuration with integral analog signal processing (Eltec, 1991). Lithium tantalate ($LiTaO_3$), a non-hydroscopic single-crystal material that maintains its pyroelectric properties to a Curie point of 610°C, was chosen for its demonstrated sensitivity and stability (Eltec, 1993). The *Model 442* is the only current-mode (transimpedance) dual-element detector commercially available. Selected specifications for the basic sensor are provided in Table 17-3. For long-range operation in exterior settings (Cima, 1992), the sensor is incorporated into the *Model 862 Passive Infrared Telescope*, with narrow field-of-view ranges out to 500 feet.

Table 17-3. Selected specifications for the *Model 442 IR-Eye* detector (courtesy Eltec Instruments, Inc.).

Parameter	Value	Units
Spectral response	8-14	micrometers
NEP	1.1×10^{-9}	watts
D*	2.2×10^{8}	√Hz/watt
Responsivity	3.7×10^{5}	volts/watt
CMR (Minimum)	5/1	
(Maximum)	15/1	
Noise	0.36	millivolts/√Hz
Power	5-15	volts DC
	2	milliamps
Housing	TO-5	
Size (diameter)	.360	inches
(height)	.190	inches

Nippon Ceramic *Model SEA02-54* Pyroelectric Sensor

The *Model SEA02-54* pyroelectric sensor manufactured by Nippon Ceramic Co., Ltd., Tottori, Japan, is a series-opposed dual-detector configuration based on a ceramic ferroelectric material (Nippon, 1991). Typical motion-detection applications include occupancy sensing for lighting and air conditioning control, visitor enunciation, and security systems. The *Model SEA02-54* sensor and a lower-cost version (*Model RE200B*) are distributed in the United States by McGee Components, Inc., North Attleboro, MA. Selected specifications are listed in Table 17-4 below.

Table 17-4. Selected specifications for the *Model SEA02-54* and *Model RE200B* pyroelectric sensors (courtesy McGee Components, Inc.).

Parameter	*SEA02-54*	*RE200B*	Units
Spectral response	7-14	5-14	micrometers
NEP	8.8×10^{-10}	9.6×10^{-10}	watts
D*	1.6×10^{8}	1.5×10^{8}	√Hz/watt
Responsivity	3.2×10^{3}	3.3×10^{3}	volts/watt
Noise	70	80	millivolts/√Hz
Power	2.2-15	2.2-15	volts DC
	12	12	microamps
Housing	TO-5	TO-5	
Size (diameter)	9.2	9.2	millimeters
(height)	4.8	4.5	millimeters

Scanning PIR Configurations

The fact that pyroelectric sensors respond only to changes in thermal energy is actually an advantage in fixed-installation security systems, since an intruder must at some point move into the sensor's field of view to be considered a potential threat. In the case of a mobile security robot, however, this is not always the case. An intruder can easily enter a secured zone before the robot arrives on scene, and simply has to remain motionless (or hidden) when the area comes under temporary surveillance. Once the robot departs, the intruder is free to resume his or her clandestine activities until such time as the robot makes another patrol.

For this reason, investigations have been conducted into potential ways of operating pyroelectric sensors as *human presence detectors*. For example, a number of researchers have attempted to accommodate the differential nature of the pyroelectric sensor by scanning the device about the vertical axis, thus enabling detection of stationary thermal sources. The single PIR sensor incorporated on ROBART I was mounted on the robot's head to facilitate panning slowly back and forth in search of non-moving intruders (Everett, 1982a).

A commercially available scanning configuration is seen in Cybermotion's *Security Patrol Instrumentation (SPI)* module employed on their *SR2* robot (Holland, 1993). The *SPI* incorporates a scanning sensor array rotated by a small DC motor at about 60 rpm. Slip-ring connections are provided for four sensor modules spaced 90 degrees apart on the rotor assembly:

- Passive infrared vertical array.
- Visible-light vertical array.
- Continuous-wave K-Band microwave motion detector.
- Ultraviolet flame detector.

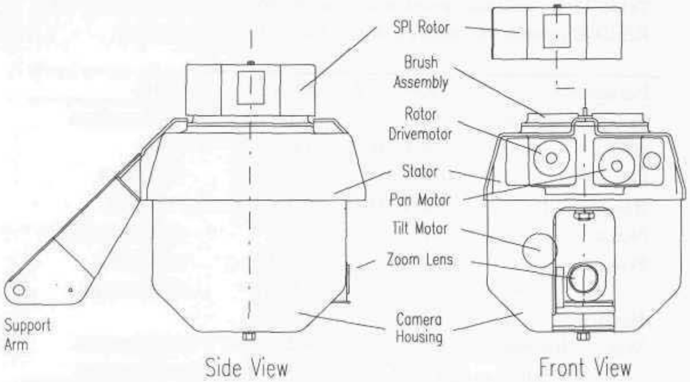

Figure 17-10. Schematic drawing of the Cybermotion *Security Patrol Instrumentation (SPI)* module with integrated surveillance camera pan-and-tilt (courtesy Cybermotion, Inc.).

The passive infrared vertical array consists of four Eltec *Model 442* sensors stacked to achieve an instantaneous field of view of 5.6 degrees horizontal and 31.6 degrees vertical. A *target identification algorithm* extracts perceived movement from scan-to-scan thermal differences and passes the results to a *target tracking algorithm*, where the highest probability targets are closely monitored. The company describes this hardware/software combination as neither a *motion detector* nor a *presence detector* in the strictest sense, but more of a "change-of-presence detector."

Viggh & Flynn (1988) describe a continuously rotating pyroelectric detector implementation on the MIT robot *Seymour* that incorporates a pair of narrow field-of-view sensors, also based on the Eltec *Model 442* detector. A *synthetic field of view* defined by the leading-edge detections associated with each of the two sensors is created by the scanning motion as illustrated in Figure 17-11. An output signal similar to that shown earlier in Figure 17-8 will be generated each time a *442* sensor sweeps across a high-contrast thermal source. The elapsed time interval between detections by the individual sensors is a function of the separation distance between the robot and the perceived hot spot, due to the diverging nature of the synthetic field of view, and thus indicative of range to a suspected human target. (The MIT system was expressly developed to support a human-following behavior routine.)

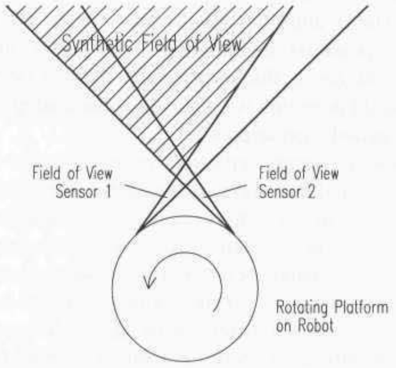

Figure 17-11. A rotating synthetic field-of-view created by two revolving *PIR* sensors yields a varying time delay between leading-edge detection of a stationary person that is proportional to range (adapted from Viggh & Flynn, 1988).

17.1.6 Microwave Motion Detection

Microwave motion detectors operating at radio frequencies rely on the *Doppler shift* introduced by a moving target (Chapters 8 and 9) to sense the relative motion of an intruder. Commercially available systems are generally of two types: 1) *continuous wave* and 2) *pulsed*. Most *continuous-wave* systems employ a *Gunn diode* serving as both transmitter and local oscillator, and a *Schottky-barrier mixer-diode* receiver feeding a low-noise intermediate-frequency (IF) amplifier (Alpha, 1987). *Pulsed* systems incorporate an additional square-wave driver as shown in Figure 17-12 to regulate the duty cycle (i.e., 10 percent typical) to conserve power.

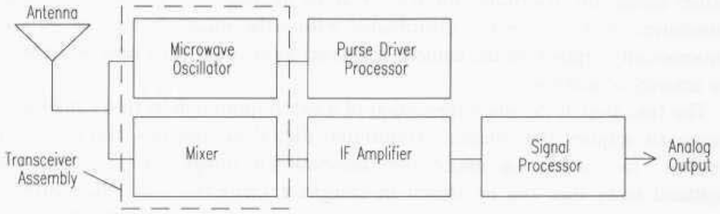

Figure 17-12. Block diagram of a typical pulsed Doppler microwave motion detector (adapted from Williams, 1989).

Both *continuous-wave* and *pulsed* configurations generally employ a common transmit and receive antenna. The *mixer diode* combines reflected energy from the target with a reference signal from the *Gunn oscillator*, generating an output signal with an amplitude that varies as a function of the phase difference between its two inputs, and with a frequency proportional to the relative radial velocity (Williams, 1991). The IF amplifier usually incorporates 60- and 120-Hertz notch filters to eliminate potential interference from power lines, as well as the fluctuations of ionized gas in fluorescent light fixtures (Williams, 1989; 1991). Some form of threshold detection is employed at the analog output to signal radial motion above a pre-established setpoint.

The electromagnetic energy emitted by microwave motion sensors can penetrate hollow walls and doorways, allowing the sensor to "see" into adjoining rooms in certain circumstances. This feature can be used to advantage by a robot patrolling a hallway to check locked office spaces and storerooms without need for entry. There is some inherent sensitivity to nuisance alarms, particularly in the presence of rotating machinery, or in scenarios where building walls and/or windows are subject to vibration from overflying aircraft or vehicular traffic. The effective detection of intruders is dependent on the degree of radial motion, target range, background interference, and the target's *effective cross-section* σ (Chapter 9). Human targets typically have a value of σ between 0.2 and 2.0 meters^2 (Alpha, 1987).

17.1.7 Video Motion Detection

Vision systems offer a sophisticated method of sensing intrusion in outdoor as well as indoor applications, with the added benefits of excellent resolution in the precise angular location of the intruder. A surveillance camera is used to digitize a scene for comparison with a previously stored image pattern representing the same region, and significant deviations between the two can be attributed to motion within the FOV. "Windowing" techniques can be employed on most systems to selectively designate certain portions of the image to be ignored (such as a tree blowing in the wind), resulting in a significant reduction in nuisance alarms. Simple algorithms that distinguish purposeful from random motion can further refine this discrimination feature at the intelligent-sensor level. Calculated boundaries of the perceived disturbance within the image frame can be used to automatically reposition the camera in closed-loop systems to keep it centered on the activity of interest.

The first step in the implementation of a video motion detection capability is of course to acquire the image. Traditional digital approaches employ a "frame grabber" to convert an entire two dimensional image into a corresponding digitized array that can be stored in computer memory. For every pixel there exists an associated RAM location describing scene intensity (gray levels) at that particular location. For a conventional 525-line television image with 512 pixels-per-line horizontal resolution, this equates to 268,800 memory locations (bytes). In other words, over a quarter megabyte of memory is required to store a single frame of video. The second step involves processing the data that has just been acquired. Due to the array size, even the simplest of operations, such as thresholding to convert to a binary image, is time consuming. More elaborate operations simply cannot be done using simplistic hardware before the next image arrives at the NTSC rate of 60 frames per second.

Experiments with the linear CCD-array cameras employed on ROBART II (see Chapter 4) showed it was possible to detect motion by examining only one horizontal line cutting through the region of interest in the scene. If several horizontal lines equally spaced throughout the scene are acquired, effective full-screen coverage could be achieved without the need to "grab" the entire frame. The image processing needs would be greatly reduced, and in most cases could be performed during the wait period between lines of interest when the acquisition system was idle. As an example, if only a single line is sufficient, the memory requirement would be reduced to half a kilobyte, with 16.4 milliseconds available for processing before the next line must be digitized.

The *Reconfigurable Video Line Digitizer* was developed for just this purpose, and consists of a high-speed (100-nanosecond conversion time) analog-to-digital (A/D) converter which samples the composite video signal of a conventional NTSC-format camera output. The composite video is also fed to a sync separator that splits off the horizontal and vertical sync pulses and provides a frame index (Figure 17-13). (Note: the single-chip *AD9502BM* video digitizer available from Analog Devices (Hansford, 1987) contains a flash A/D converter and integrated sync strippers.) The horizontal sync pulses drive a counter that identifies the scan line of interest in the scene, whereupon line digitizing is performed. The digital output of the A/D converter is written directly into dual-buffered high-speed (35-nanosecond) video RAM, in order that it might be accessed later by the microprocessor when the A/D is idle.

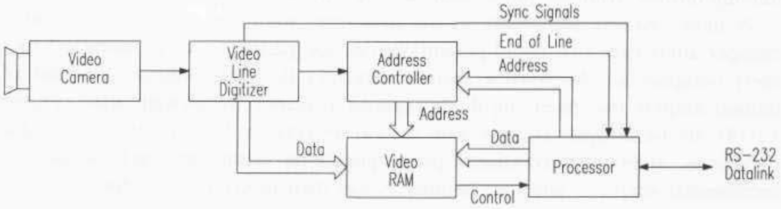

Figure 17-13. Block diagram of the video line grabber developed for use on ROBART II.

The most simplistic motion detection algorithm involves subtracting the latest intensity array from a previously acquired array, and reacting to any significant discrepancies indicative of changes in the scene under observation. In reality, some software filtering is required to eliminate noise and reduce the occurrence of nuisance alarms, but this is easily accomplished on a 512-element linear data array in the time available. (For simple motion detection schemes, 256 elements of horizontal resolution are more than adequate, further reducing required system complexity.)

Assuming full 512-pixel coverage, only 2K bytes of RAM are sufficient to support the microcomputer operating system and to save three select lines of video data, which normally would be equally spaced across the region of interest. Once motion is detected in any of the three lines, it is possible to select new lines for the next motion analysis operation. If these lines are chosen in such a fashion around the vicinity of the initially detected disturbance, it is possible over successive frames to converge on and effectively bound the area perturbed by the intrusion. In this fashion, the system can detect and output information describing the geometric area involved so as to provide servo-control inputs for camera positioning or robot motion algorithms.

17.1.8 Intrusion Detection on the Move

Most commercially available security sensors operate through detection of relative motion, and must be attached to a stable (i.e., non-mobile) mounting. In the early 1980s, Denning Mobile Robots experimented with a specially configured *microwave motion detector* developed by Alpha Industries in an attempt to address this problem (Everett, 1988). The Alpha sensor employed a programmable notch filter that theoretically could be set to filter out the Doppler component introduced by forward travel of the platform itself. In reality, however, this simplistic notch filter approach proved to be a bit idealistic, due to the off-axis velocity components arising from the cone-shaped nature of the beam and the presence of multiple harmonics. An alternative (but more costly) strategy may be to process the analog output signal with a pattern-matching algorithm trained to distinguish the less-structured Doppler components generated by a moving intruder from the more predictable results attributed to platform motion.

A more realistic possibility in the meantime would be to consider a much cheaper alternative that could potentially provide partial coverage using off-the-shelf components. *Microwave motion detectors* that discriminate direction of motion employ two receiving diodes spaced a quarter wavelength apart (Figure 17-14), so the Doppler outputs from the two mixers are 90 degrees out of phase (Williams, 1989). Conventional phase-quadrature techniques such as used in incremental encoders and interferometers can then determine direction of target motion. A common application for these direction-discriminating microwave devices is automatic traffic control, where it is necessary to distinguish between cars approaching a light and those moving away. For example, the AM Sensors *Model MSM10502* can be preset to respond only to objects moving toward the sensor, or alternatively away from the sensor.

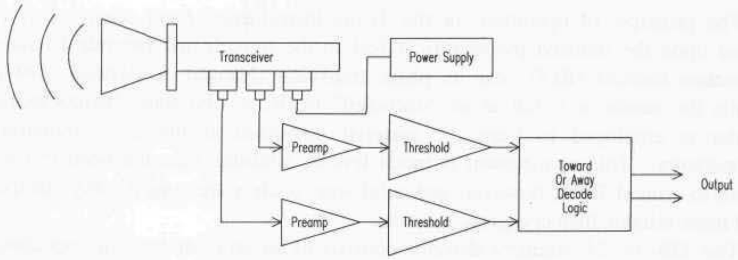

Figure 17-14. The use of two mixer diodes spaced a quarter-wavelength apart (90 degrees) allows for determination of the direction of relative motion (adapted from Williams, 1989).

Assuming stationary-object Doppler components due to forward motion of the platform (while admittedly consisting of a multitude of frequencies) are all indicative of relative movement towards the platform, the possibility for detecting intruder motion away from the platform seems obvious. A forward-looking direction-discrimination sensor, preset for receding objects only, should theoretically ignore the effects of platform motion altogether, yet respond to any mobile targets moving away from the vehicle. Similarly, a rear-facing sensor preset for approaching objects would likewise detect any mobile target gaining on the vehicle from behind. While there are obvious limitations to this detection strategy, they fortunately are somewhat aligned with the least vulnerable of potential intruder response scenarios. For example, an intruder in front of an approaching MDARS platform is most likely going to retreat rather than advance toward the vehicle, and in so doing becomes susceptible to detection.

The above approach seems worthy of further investigation as a low-risk interim solution for motion detection on the move. The most likely longer term candidate technology for truly solving the problem is probably image processing, based on video obtained from a *FLIR (forward-looking infrared)*, or a low-light-level or image-intensified CCTV camera. Conventional *FLIRs* and image-intensified cameras are not cheap, however, and the required image processing hardware is expensive as well. Recent developments in *uncooled FLIR* technology may hold promise for significantly reduced costs in the near future.

Texas Instruments Ferroelectric Focal Plane Array

Texas Instruments has been a principle contender in the recent development of a new generation of FLIRs that do not require cryogenic cooling of the detector element. Cryogenic cooling of conventional FLIRs adds to system complexity and cost, with a significant decrease in reliability, as most coolers have a *mean time between failure* of around 1500 hours. In addition, the initial cool-down period required after system start-up (before the detector becomes operational) can significantly hamper quick response in security applications.

The principle of operation for the Texas Instruments' *focal plane array* is based upon the induced pyroelectric effect in the ferroelectric-ceramic *barium-strontium titanate (BST)* near its phase transition (Hanson & Beratan, 1994). While the sensor is billed as an "uncooled" FLIR, a solid-state thermoelectric cooler is employed to keep the material stabilized at the 22°C transition temperature. This requirement is much less of a burden than the need to cool down to around 75°K, however, and solid-state coolers are considerably cheaper and more reliable than cryogenic systems.

The 328- by 245-element *detector* consists of an array of ceramic capacitors bump-bonded to CMOS VLSI readout circuitry containing a dedicated preamplifier, noise filter, buffer, and switch for each pixel (Hanson, et al., 1993). A row-address shift register and a column multiplexer are included into the IC design to generate a serial output format that can be easily processed to yield a standard composite-video signal. The *IR absorber* (Figure 17-15) consists of a three-layer resonant cavity, where the bottom layer is an opaque metal film that also serves as the common upper plate for the pyroelectric capacitors. A 1.25-micrometer-thick intermediate layer of *parylene* is used to tune the cavity for an absorption peak of approximately 10 micrometers (Hanson & Beratan, 1994). The detector face is a thin semi-transparent metal layer that matches the optical impedance of the cavity to free space.

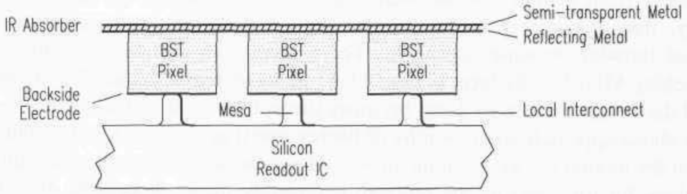

Figure 17-15. The Texas Instruments *focal plane array* is reticulated to reduce thermal crosstalk between pixels, and thermally isolated from the readout electronics by polyimide mesas (adapted from Hanson, et al., 1993).

Since pyroelectric sensors do not have a true DC response as previously discussed, a mechanical chopper is employed in the current design, with successive frames differenced to produce a final image. This technique produces a sort of halo effect around the edges of high-contrast (i.e., significant temperature differential) image features. While this artifact is of minimal concern in conventional surveillance scenarios, it can potentially interfere with automated motion-detection functions associated with robotic security equipment.

Texas Instruments received a Phase I *Low Cost Uncooled Sensor Program (LOCUSP)* contract award in 1990 to produce prototype weapons sights for the US Army, resulting in a demonstrated average *noise equivalent temperature difference (NETD)* of 0.08°C with *f*/1.0 optics (Hanson, et al., 1992). A *LOCUSP* Phase II contract was awarded in 1994 to further improve performance (Hanson &

Beratan, 1994). In an effort to transition this military-oriented technology into civilian law enforcement applications, the *Nightsight Thermal Vision System* (Figure 17-16) was jointly developed by Texas Instruments and Hughes Aircraft Company (TI, 1994). The goal was to produce a low-cost (approximately $6,000) night-vision system for installation in police cruisers.

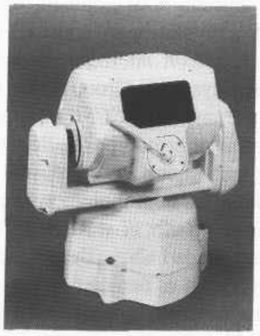

Figure 17-16. The *Nightsight Thermal Vision System* with integrated pan-and-tilt unit is available for crossbar installation on police cruisers for under $10,000 (courtesy Texas Instruments, Inc.).

Table 17-5. Selected specifications for the *Nightsight* camera (TI, 1994).

Parameter	Value	Units
Pixels	80,360	
Format	328 x 245	
Field-of-View	27 (V) by 18 (H)	degrees
NETD	< 0.12	degrees C
Detection Range (human)	20 - 900	feet
Video Interface	RS-170/NTSC	
Update rate	60	Hz
Image Polarity	selectable	
Warm up time	< 30	seconds
Power	9 - 16	volts DC
	6	watts
Size (length)	8	inches
(width)	6	inches
(height)	6	inches
Weight	< 8	pounds

The *Nightsight* kit consists of an uncooled IR sensor, pan-and-tilt unit, video display, control console, and the required interface hardware. The front window of the environmentally sealed sensor housing is equipped with an automatic defroster and wiper blade. Selected specifications are listed in Table 17-5.

Alliant Techsystems Microbolometer Focal Plane Array

Honeywell's Sensor and System Development Center, Bloomington, MN, developed in the early 1980s a revolutionary approach to high-resolution uncooled focal plane arrays, based on *silicon microbolometer* technology. In 1990, the company's former Defense Systems Group was spun off to form Alliant Techsystems and received a Phase I *LOCUSP* contract award to develop a low-cost battlefield surveillance sensor prototype (Gallo, et al., 1993).

Silicon micromachining techniques are employed to fabricate large arrays of individual detectors operating as microbolometers in the 8 to 12 micrometer region of the infrared spectrum (Gallo, et al., 1993). The 336- by 240-pixel array is made up of tiny masses suspended above the IC face by two support struts that provide excellent thermal isolation as depicted in Figure 17-17. Temperature rise due to incident radiation is quantified by measuring the resistance of a region of vanadium oxide on each small mass; the connections run down the support struts to the integrated readout electronics for each pixel. No cooler is required for operation, but a simple thermoelectric device is used to minimize the effect of thermal drift. The entire device is fabricated as a monolithic silicon IC, with a final etch step creating the gap under the masses.

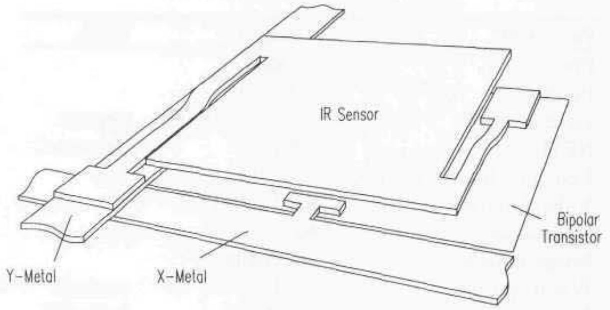

Figure 17-17. Typical microbridge detector element employed in the *microbolometer focal plane array* (adapted from Gallo, et al., 1993).

A *NETD* well under 0.1°C is achievable, along with a pixel-to-pixel thermal isolation of -142 dB, making "blooming" virtually non existent (Gallo, et al., 1993). The sensor's true DC response eliminates the need for a mechanical chopper, for improved reliability with reduced size, weight, and power consumption. In addition, the achievable *NETD* relative to comparable ferroelectric designs employing choppers is improved by a factor of two for the following reasons (Gallo, et al., 1993):

- The incident radiation is not blocked every other frame, for an improvement factor of 1.4.
- The sensor frame rate can be reduced from 60 Hz to 30 Hz, for an additional improvement factor of 1.4.

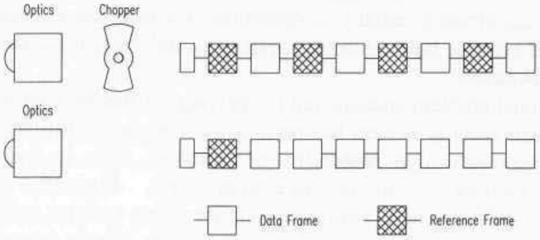

Figure 17-18. Chopperless operation provides twice the *noise equivalent temperature difference (NETD)* over comparable ferroelectric designs (adapted from Gallo, et al., 1993).

The basic *LOCUSP* sensor head comes with a dual-mode optics assembly that can be remotely operated to select either a wide (15- x 9-degree) or narrow (5- x 3-degree) field of view. Selected specifications are provided in Table 17-6 below.

Table 17-6. Selected specifications for the Alliant Techsystems uncooled FLIR (Gallo, et al., 1993).

Parameter	Value	Units
Pixels	82,320	
Format	240 x 336	
Field-of-View (wide)	15 (V) by 9 (H)	degrees
(zoom)	5 (V) by 3 (H)	degrees
NETD	< 0.1	degrees C
Detection Range (human)	4,920	feet
Video Interface	RS-170/NTSC	
Update rate	30	Hz
Image Polarity	selectable	
Warm up time	< 10	seconds
Power	24	volts DC
	12	watts
Size (length less optics)	5.1	inches
(width)	5.3	inches
(height)	7.1	inches
Weight (less optics)	< 7.3	pounds

17.1.9 Verification and Assessment

Potential security functions assigned to a mobile sentry robot can be categorized into four general areas: (1) *detection*, (2) *verification*, (3) *assessment*, and (4) *response* (Everett, 1988). *Detection* is readily addressable by a multitude of commercially available sensors of the type presented above. *Verification* involves cross-checking with other sensors to lessen the chances of a nuisance alarm and depends heavily upon both the types of detectors employed and the operating environment. The *assessment* task acts upon the data collected to ascertain the nature of the disturbance, usually to determine if a response is necessary. The *response* itself must be tailored to the application, the operating scenario, and the nature of the situation.

The traditional problem encountered in applying off-the-shelf intrusion sensors in an automated security system has been as the detector sensitivity is raised to provide the necessary high probability of detection, there is a corresponding unacceptable increase in the nuisance alarm rate. Operators quickly lose confidence in such a system where sensors are prone to false activation. For example, passive infrared motion detectors can be falsely triggered by any occurrence that causes a localized and sudden change in ambient temperature within the sensor's coverage area. This false triggering can sometimes occur naturally, as in the case of an exterior sensor viewing trees blowing in the wind. Optical motion detectors can be activated by any change in ambient light level, as could be caused by passing automobile headlights or lightning flashes. Discriminatory hearing sensors could be triggered by loud noises originating outside the protected area, such as thunder, passing traffic, or overflying aircraft. Microwave motion detectors can respond to rotating or vibrating equipment, and so forth.

A truly robust robotic or automated security system must employ a variety of intrusion detection sensors and not rely on any single method. This redundancy thwarts attempts to defeat the system, due to the higher probability of detection with multiple sensors of different types. Equally as important, such redundancy provides a means of verification to reduce the occurrence of nuisance alarms (i.e., redundant intrusion detection schemes operating on different principles will not all respond to the same spurious interference). The strategy employed on ROBART II involves using numerous types of broad coverage sensors (Figure 17-19) as primary detection devices, and higher-resolution units in a secondary confirmation mode to verify and more clearly characterize a suspected disturbance. The robot is alert at all times, but its acuity can be enhanced by self-generated actions that activate these additional systems when needed to better discriminate among stimuli.

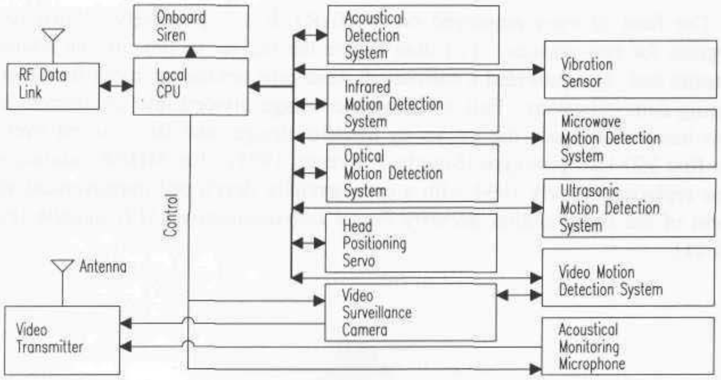

Figure 17-19. Block diagram of the security sensor suite employed on ROBART II.

The field of view is divided into four discrete zones (Figure 17-20), with different types of redundant motion detection schemes assigned to each zone. An array of 24 ultrasonic ranging units with 360-degree coverage can be activated to establish the position of a moving intruder with respect to the robot. A miniature high-resolution CCD surveillance camera is deployed on a panning mechanism for specific direction at areas of suspected disturbance. Assessment of the results is performed by appropriate software that cross-correlates among redundant primary sensors within a specific detection zone, and schedules and interprets subsequent verification by the secondary high-resolution sensors (Smurlo & Everett, 1993). The goal of the intelligent assessment software is to make the robot sensitive enough to detect any intrusion, yet smart enough to filter out nuisance alarms (Everett, et. al., 1988).

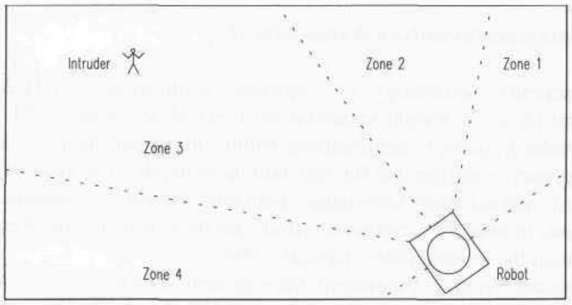

Figure 17-20. The six groups of intrusion detection sensors employed on ROBART II are arranged with full 180-degree coverage divided into four fan-shaped zones.

The field of view employed on ROBART II was purposely limited to 180 degrees for two reasons: 1) I didn't have the budget to procure the additional sensors and 2) it provided a convenient dead zone behind the robot for observers during demonstrations. Full 360-degree coverage divided into 24 discrete zones was incorporated into the follow-on ModBot design, and later carried over into the first MDARS prototype (Smurlo & Everett, 1993). The MDARS staring array was replaced in early 1994 with a commercially developed improvement in the form of the Cybermotion *Security Patrol Instrumentation (SPI)* module (Figure 17-21).

Figure 17-21. An early prototype of the *Security Patrol Instrumentation (SPI)* module with an underhung pan-and-tilt unit for surveillance camera (courtesy Cybermotion, Inc.).

17.2 Automated Inventory Assessment

The Microcircuit Technology in Logistics Applications (MITLA) Program Management Office at Wright-Patterson Air Force Base, Dayton, OH, is the focal point for *radio frequency identification* within the Department of Defense. As such, this agency is responsible for maintaining in-depth knowledge of the state of the art, and making that knowledge available to DoD customers. Ongoing developments in over 20 coordinated efforts are underway at a number of military installations in the United States (Lawlor, 1993).

The Physical Security Equipment Management Office submitted an informal request for an RF-tag market investigation to MITLA in early December 1993, as well as a list of potential suppliers previously compiled by the MDARS developers. A review of the stated MDARS needs as compared to existing capabilities within the industry subsequently conducted, with the more difficult core requirements for a long-range omni-directional system that could read/write to at least 10 or 12 feet addressed first. MITLA reported that to the best of their knowledge, only Savi Technology, Mountain View, CA, had a system (at the time) that could perform remote read/write operations in an omni-directional pattern at distances greater than 50 feet.

17.2.1 MDARS Product Assessment System

The MDARS *Product Assessment System* is physically separated into two groups of components respectively located at the host console and on the robotic platforms as depicted in Figure 17-22. The *Product Assessment Computer* collects tag data (when available) from multiple robots, storing the information in the *Product Database Computer*. The *Product Database Computer*, as the name implies, is a database that keeps track of all tags read in by the robots as well as those entered manually by the user. The *Database Access Computer* is the user interface to the *Product Database Computer*, allowing the entry of manual information, editing of existing tag information, as well as generation and viewing of various tag reports.

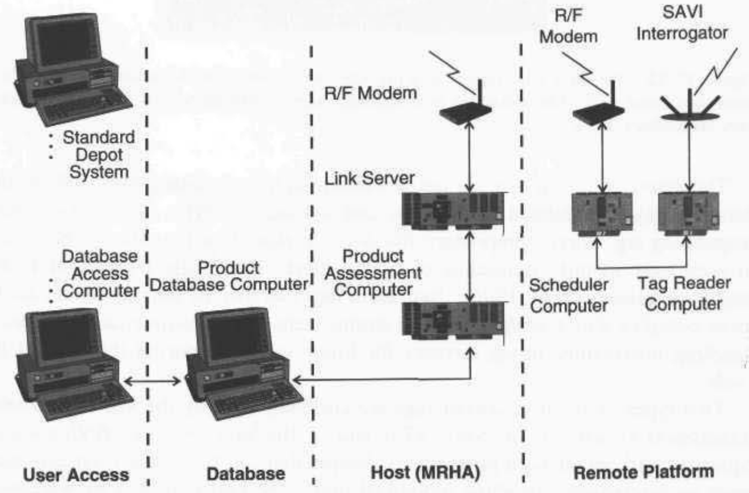

Figure 17-22. Block diagram of the MDARS Product Assessment System (courtesy Naval Command Control and Ocean Surveillance Center).

The hardware resident on each mobile robot consists of a Savi *Interrogator* for bidirectional communication with interactive RF transponder tags attached to high-value inventory items (Savi, 1994a), and a controlling *Tag Reader Computer*. When commanded by a *virtual-path program instruction*, the *Tag*

Reader Computer collects all tag information from the *Interrogator* and buffers it in internal blackboard memory for later transfer to the *Product Assessment Computer* when requested. The *Interrogator* is an off-the-shelf unit designed for unlicensed operation (below FCC Part 15 power levels) at either 315 or 433.92 MHz (Lawlor, 1993). Early models employed three 12-inch stub antennae mounted external to the half-spherical housing, 120 degrees apart for full omni-directional coverage, while the most recent version (Figure 17-23) incorporates a pair of antennae inside the housing for a rugged, less-obtrusive profile.

Figure 17-23. The Savi *Interrogator* is a microprocessor-controlled RF transceiver capable of omni-directional read/write operations to transponder tags located up to 150 feet away (courtesy Savi Technology, Inc.).

The *Interrogator* first sends out a wakeup signal consisting of a 3.49-second duration pulse modulated at 30-KHz, and uploads 10 bytes of data from each responding tag. Savi's proprietary *Batch Collection* algorithm allows the system to accurately identify thousands of tagged assets at a single read location in a matter of minutes (Savi, 1993). Individual tags can then be directly addressed for more complex data transfers, such as storing item-unique maintenance or special handling instructions in tag memory for future reference during the product life cycle.

Two types of RF transponder tags are currently used by the *MDARS Product Assessment System*: 1) the Savi *TyTag* and 2) the Savi *SealTag*. Both units are equipped with an onboard piezoelectric beeper that can be activated on command from an *Interrogator* to allow individual tags to be easily located by warehouse personnel (Savi, 1994b). The *TyTag* (Figure 17-24) operates on a 6-volt 600-mAh Lithium flat-pack battery and will automatically issue a low-battery warning (i.e., set a status bit in the tag's data stream) at 5.16 volts. The minimum operating voltage required to achieve a 25-foot line-of-sight range is 4.16 volts, and typical battery life is two years with two data collections per day. *TyTags* are normally intended for indoor operation only and are available with 128 or 256 bytes of non-volatile memory.

Table 17-7. Selected specifications for the Savi *Model CLIN 0003AA Interrogator.*

Parameter	Value	Units
Frequency	315 or 433	MHz
Range	300	feet
RF pattern	360	degrees
Memory	64K	bytes
Data rate (RF)	9600	baud
RS-232	9600	baud
RS-485	38.4K	baud
Power	6-15	volts DC
	100	milliamps
Size (diameter)	12	inches
(height)	4.5	inches
Weight	6.5	pounds

The *SealTag* (Figure 17-24) is enclosed in a rugged environmental package suitable for exposed outdoor operation and is available with an extended non-volatile memory of up to 128 kilobytes for mass storage of information such as product history or container manifests (Savi, 1994b). A 6-volt 1400-mAh lithium battery provides an expected service life of four years assuming two data collections per day, and battery status is automatically monitored as in the case of the *TyTag*. A real-time clock is incorporated into the SealTag design to facilitate time-stamping data or event occurrences.

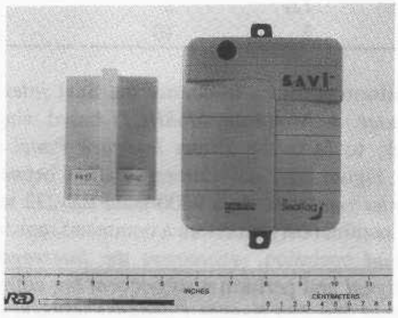

Figure 17-24. The Savi *TyTag* (left) is an interactive RF transponder with up to 256 bytes of read/write memory storage; the *SealTag* (right) can have up to 128 kilobytes and is equipped with four binary input lines that monitor external events (courtesy Savi Technology, Inc.).

An inverted-TTL RS-232 serial interface and four binary I/O lines are provide on the *SealTag* to communicate with auxiliary equipment and/or monitor external events. A change in logic level of an input line will toggle the state of an associated bit in the data stream read by the *Interrogator*, greatly expanding the versatility of the system. For example, an input line on a *SealTag* will be used in the MDARS Exterior program to monitor the physical status (i.e., open or shut) of high-security locks and will upload this information along with the lock serial number to the patrolling MDARS vehicle upon request. In this fashion, the same hardware used to verify inventory inside a locked space can also be used to collect binary type information describing related conditions (i.e., flooding, fire, smoke).

Table 17-8. Selected specifications for the *TyTag* and *SealTag*.

Parameter	*TyTag*	*SealTag*	Units
Frequency	314.975	433.92	MHz
Transmit power	< 10	< 10	microwatts
Range	200	300	feet
Memory	128 or 256	256, 8K, 128K	bytes
Environment	indoor	indoor/outdoor	
Audible beeper	yes	yes	
Real-time clock	no	yes	
Power	6	6	volts DC
(standby)	4	10	microamps
(active)	25	25	milliamps
Battery life	2	4	years
Size (length)	3.6	5.5	inches
(width)	2.35	4.5	inches
(height)	1.6	2	inches
Weight	5	10	ounces

The MDARS platform software to control the Savi *Interrogator* runs on the *Tag Reader Computer*, a Motorola *M68HC11*-based single-board computer developed exclusively to fit in the *Turret Interface Panel* of the Cybermotion platform (see again Figure 17-22). Communication between the *Tag Reader Computer* and the *Interrogator* is via a 9600-baud RS-232 serial link. The main loop of the software continuously monitors a command register awaiting direction to perform a *tag-read* operation, whereupon the *Interrogator* is instructed to transmit a *wakeup signal* and perform a subsequent tag collection. After the tag collection is completed, the *Tag Reader Computer* uploads the collected tag IDs from the *Interrogator*, and packetizes the data into its onboard memory for later collection by the MDARS *Product Assessment Computer* at the host console.

Listed below are some of the additional capabilities of the tag-reader software.

- Write to EEPROM of *Interrogator* to adjust power level of wakeup signal.

- Instruct *Interrogator* to send out a *tag-wakeup* signal.
- Determine battery status of each tag read.
- Determine signal strength of received signal from each tag.
- Read in the 24-hour clock of *Interrogator*.
- Store current X and Y coordinates of the platform.
- Instruct a specific tag to activate or deactivate its beeper.
- Perform a search to find a specific tag.

In January 1995, extensive testing was conducted by the MDARS development team at the Camp Elliott warehouse facility in San Diego (Figure 17-25) to assess the accuracy of several tag-position-estimation algorithms (Smurlo, et al., 1995). The test was also designed to determine the impact of performing tag-read operations at two different stop intervals (37.5 and 75 feet) along the route, using 173 Savi *TyTags* placed at known locations throughout the warehouse. For survey intervals of 37.5 feet, the best performing algorithm achieved an average of approximately 15 feet positional uncertainty (i.e., the difference between estimated and actual tag locations), while for survey intervals of 75 feet the uncertainty was increased to approximately 20 feet.

Figure 17-25. An earlier model of the Savi *Interrogator* mounted on top of the MDARS Interior robot undergoing feasibility testing at the Camp Elliott warehouse facility in San Diego, CA (courtesy Naval Command Control and Ocean Surveillance Center).

17.3 References

Ademco, "Quad Passive Infrared Motion Detector," *1989 Security Sourcebook: The Ademco Catalog of Products*, P6715, Ademco Alarm Device Manufacturing Company, Syosset, NY, May, 1989.

Alpha, "Theory, Operation, and Application of Microwave Motion Sensing Modules," *Sensors*, pp. 29-36, December, 1987.

Bancroft, A.J., "The First Commercial Floor Care Company that Ventured into the Production of Robotics," Conference on Intelligent Robotics in Field, Factory, Service, and Space, CIRFFSS '94, Houston, TX, pp. 669-674, March, 1994.

Barron, W.R., "The Principles of Infrared Thermometry," *Sensors*, pp. 10-19, Decmber, 1992.

Buschling, R., "Understanding and Applying IR Temperature Sensors," *Sensors*, pp. 32-37, October, 1994.

Byler, E., "Intelligent Mobile Sensor System for Drum Inspection and Monitoring," Phase I Topical Report, DOE Contract DE-AC21-92MC29112, Martin Marietta Astronautics Group, Littleton, CO, June, 1993.

Cima, D., "Using Lithium Tantalate Pyroelectric Detectors in Robotics Applications," Eltecdata #112, Eltec Instruments, Inc., Daytona Beach, FL, 1984.

Cima, D., "Using Optical Radiation for Security," Eltecdata #124, Eltec Instruments, Inc., Daytona Beach, FL, December, 1990.

Cima, D., "Surveillance Applications of the Eltec Model 862 Passive Infrared Telescope," Eltecdata #128, Eltec Instruments, Inc., Daytona Beach, FL, June, 1992.

Eltec, "Introduction to Infrared Pyroelectric Detectors," Eltecdata #100, Eltec Instruments, Inc., Daytona Beach, FL, 1984.

Eltec, "Model 442 IR-Eye Integrated Sensor," Preliminary Product Literature, Eltec Instruments, Inc., Daytona Beach, FL, April, 1991.

Eltec, "Model AR170, 32 Element Pyroelectric Array," Product Literature, Eltec Instruments, Inc., Daytona Beach, FL, December, 1993.

Everett, H.R., "A Computer Controlled Sentry Robot," *Robotics Age*, March/April, 1982a.

Everett, H.R., "A Microprocessor Controlled Autonomous Sentry Robot", Masters Thesis, Naval Postgraduate School, Monterey, CA, October 1982b.

Everett, H.R., "Security and Sentry Robots", *International Encyclopedia of Robotics Applications and Automation*, R.C. Dorf, ed., John Wiley, pp. 1462-1476, March, 1988.

Everett, H.R., Gilbreath, G.A., Alderson, S.L., Priebe, C., Marchette, D., "Intelligent Security Assessment for a Mobile Sentry Robot", Proceedings, 29th Annual Meeting, Institute for Nuclear Materials Management, Las Vegas, NV, June, 1988.

Everett, H.R., Gilbreath, G.A., Tran, T., Nieusma, J.M., "Modeling the Environment of a Mobile Security Robot," Technical Document 1835, Naval Command Control and Ocean Surveillance Center, San Diego, CA, June, 1990.

Gage, D.W., Everett, H.R., Laird, R.T., Heath-Pastore, T.A., "Navigating Multiple Robots in Semi-Structured Environments," ANS 6th Topical Meeting on Robotics and Remote Systems, Monterey, CA, February, 1995.

Gallo, M.A., Willits, D.S., Lubke, R.A., Thiede, E.C., "Low Cost Uncooled IR Sensor for Battlefield Surveillance," SPIE Infrared Technology XIX, Vol. 2020, San Diego, CA, July, 1993.

George, S.C., "Robot Revival," *Security*, pp. 12-13, June, 1992.

Gontowski, W., "Build a Motion Detector Alarm," *Electronic Experimenter's Handbook*, pp. 56-64, 1983.

Hansford, A., "The AD9502 Video Signal Digitizer and its Application", Analog Devices Application Note C1100-9-7/87, Norwood, MA, July, 1987.

Hansen, C., Beratan, H., Owen, R., Corbin, M., McKenney, S., "Uncooled Thermal Imaging at Texas Instruments," SPIE Infrared Technology XVIII, Vol. 1735, San Diego, CA, pp. 17-26, July, 1992.

Hanson, C., Beratan, H., Owen, R., Sweetser, K., "Low-Cost Uncooled Focal Plane Array Technology," Detector IRIS Meeting, Bedford, MA, August, 1993.

Hanson, C., Beratan, H. "Uncooled Pyroelectric Thermal Imaging," International Symposium on Applications of Ferroelectrics, 1994.

Heckendorn, F.M., Ward, C.W., Wagner, D.G., "Remote Radioactive Waste Drum Inspection with an Autonomous Mobile Robot," ANS Fifth Topical Meeting on Robotics and Remote Systems, American Nuclear Society, Knoxville, TN, pp. 487-492, April, 1993.

Holland, J.M., "An Army of Robots Roams the Night," International Robot and Vision Automation Show and Conference, Detroit, MI, pp. 17.1-17.12, April, 1993.

ISRA, "Military Finds Big Cost Savings from Mobile Robotics," *ISRA News*, Newsletter of the International Service Robot Association, Ann Arbor, MI, Fall, 1994.

Jones, J.L., Flynn, A.M., *Mobile Robots: Inspiration to Implementation*, AK Peters, Ltd., Wellesley, MA, p. 113, 1993.

King, S.J., Weiman, C.F.R., "HelpMate Autonomous Mobile Robot Navigation System," SPIE Vol. 1388, Mobile Robots V, Boston, MA, pp. 190-198, November, 1990.

Lawlor, M., "Microcircuit Technology Improves Readiness, Saves Resources," *Signal*, Armed Forces Communications and Electronics Association, August, 1993.

MacLeod, E.N., Chiarella, M., "Navigation and Control Breakthrough for Automated Mobility," Proceedings, SPIE Mobile Robots VIII, Vol. 2058, pp. 57-68, 1993.

Mattaboni, P., "An Update on Lab Rover: A Hospital Material Transporter," Conference on Intelligent Robotics in Field, Factory, Service, and Space, CIRFFSS '94, Houston, TX, pp. 405-406, March, 1994.

Mims, F.M., *Forrest Mims' Circuit Scrapbook II*, Howard W. Sams, Indianapolis, IN, pp. 170-171, 1987.

Nippon, "Pyroelectric Infrared Sensor," Nippon Ceramics Technical Information TI-101, McGee Components, Inc, North Attleboro, MA, undated.

Nippon, "Pyrosensor," Nippon Ceramics Product Literature PE 1001-1091, McGee Components, Inc, North Attleboro, MA, October, 1991.

Philips, "Ceramic Pyroelectric Infrared Sensors and Their Applications," Philips Technical Publication 163, Philips Semiconductors, Slatersville Division, Smithfield, RI, 1985.

Philips, "Movement Sensing Using a Multi-Element Fresnel Lens," Philips Semiconductors, Slatersville Division, Smithfield, RI, April, 1986.

Quick, C., "Animate vs. Inanimate," *Robotics Age*, Vol. 6, No. 9, August, 1984.

RST, "Surrogate Teleoperated Vehicle (STV) Technical Manual," Robotic Systems Technology, Westminster, MD, Contract No. N66001-91-C-60007, CDRL Item B001, Final Issue, 13 September, 1993.

Russell, R.A., "Mobile Robot Guidance Using a Short-Lived Heat Trail," *Robotica*, Vol. 11, Cambridge Press, pp. 427-431, 1993.

Savi, "The Savi Asset Management System," Product Brochure, Savi Technology, Inc., Mountain View, CA, 1993.

Savi, "System Components," Product Literature, Savi Technology, Inc., Mountain View, CA, April, 1994a.

Savi, "Savi Technology Ordering Guide," First Edition, Radio Frequency Identification Equipment Contract No. F33600-94-D-0077, Savi Technology, Inc., Mountain View, CA, November, 1994b.

Smurlo, R.P., Everett, H.R., "Intelligent Sensor Fusion for a Mobile Security Robot," *Sensors*, pp. 18-28, June, 1993.

Smurlo, R.P., Laird, R.T., Elaine, S., Jaffee, D.M., "The MDARS Product Assessment System," Association of Unmanned Vehicle Systems, 22nd Annual Technical Symposium and Exhibition, Washington, DC, July, 1995.

TI, "*Nightsight* Thermal Vision System," Product Literature, Texas Instruments, Inc., Attleboro, MA, November, 1994.

Tom, E., "Polymer Film Arrays in Pyroelectric Applications," *Sensors*, pp. 75-77, September, 1994.

Viggh, H.E.M., Flynn, A.M., "Infrared People Sensors for Mobile Robots," SPIE Vol. 1007, Mobile Robots III, Cambridge, MA, pp. 391-398, November, 1988.

Weiss, M., "Protect Your Valuables - Light Sensitive Security Alert," *Radio Electronics*, April, 1979.

Williams, H., "Proximity Sensing with Microwave Technology," *Sensors*, pp. 6-15, June, 1989.

Williams, H., "The Basic Principles of Microwave Proximity Sensing," *Sensors*, pp. 26-28, May, 1991.

Appendix
Alphabetical Listing of Cited Organizations

3M Traffic Control Materials
3M Center, Bldg 553-1A-01
St. Paul, MN 55144
POC: Tom Dahlin
Tel: 612-736-7505
Fax: 612-733-2227

Acuity Research, Inc.
3475P Edison Way
Menlo Park, CA 94025
POC: Robert Clark
Tel: 415-369-6782
Fax: 415-369-6785

AGV Products, Inc.
9307-E Monroe Road
Charlotte, NC 28270
POC: Mats Herrstromer
Tel: 704-845-1110
Fax: 704-845-1111

Alliant Techsystems, Inc.
600 Second Street NE
Hopkins, MN 55343-8384
POC: Mike Gallo
Tel: 612-931-6873
Fax: 612-931-4305

Alpha Industries, Inc.
20 Sylvan Road
Woburn, MA 01801
POC: Bill Sherman
Tel: 617-935-5150
Fax: 617-933-5582

AMP, Inc.
950 Forge Avenue
Valley Forge, PA 19482
POC: Edward Tom
Tel: 610-666-3500
Fax: 610-666-3509
AM Sensors, Inc.
(See Monitor Manufacturing, Inc.)

Analog Devices
One Technology Way
PO Box 9106
Norwood, MA 02062-9106
Tel: 617-329-4700
Fax: 617-326-8903

Apogee Robotics, Inc.
(Last known address)
2643 Midpoint Drive
Fort Collins, CO 80525
POC: Mike Henningsen

Applied Physics Systems
897 Independence Ave.
Suite 1C
Mountain View, CA 94043
POC: Robert Goodman
Tel: 415-965-0500
Fax: 415-965-0404

Applied Research Lab
PO Box 30
Penn State University
State College, PA 16804
POC: Henry Watson
Tel: 814-865-6345
Fax: 814-863-1183

Arizona State University
Chemistry Department
Tempe, AZ 85287-1604
POC: Prof. Neal Woodbury
Tel: 602-965-3294
Fax: 602-965-2747

Arnold Engineering, Inc.
PO Box 1567
Norfolk, NB 68072-1567
POC: Kent Liesemeyer
Tel: 402-371-6100
Fax: 402-371-1994

Ashtec, Inc.
1170 Kifer Road
Sunnyvale, CA 94086
POC: Sue MacLean
Tel: 408-524-1400
Fax: 408-524-1500

Associates and Ferren
Box 609 Wainscott-NW Road
Wainscott, NY 11975
POC: Bran Ferren
Tel: 516-537-7800
Fax: 516-537-4343

Banner Engineering Corp.
9714 10th Ave N.
Minneapolis, MN 55441
POC: Bob Garwood
Tel: 612-544-3164
Fax: 612-544-3213

Barnes and Reineke Corp.
425 East Algonquin
Arlington Heights, IL 60005
POC: Mike Fitzgerald
Tel: 708-640-3740
Fax: 708-640-0354

Barrier Systems, Inc.
1100 E. William Street, Suite 206
Carson City, NV 89701-3104
POC: Jay Ciccotti
Tel: 702-885-2500
Fax: 702-885-2598

Bell and Howell Mailmobile Co.
411 East Roosevelt Ave.
Zeeland, MI 49464-1395
POC: Rick Paske
Tel: 800-325-7400
Fax: 616-772-6380

Blue Road Research
2555 NE 205th Street
Troutdale, OR 97060
POC: Eric Udd
Tel: 503-667-7772
Fax: 503-667-7880

Bonneville Scientific
918 East 900 South
Salt Lake City, UT 84105
POC: Josephine Grahn
Tel: 801-359-0402
Fax: 801-359-0416

CANSPACE
(See University of New Brunswick)

Carnegie Mellon University
Robotics Institute
Pittsburgh, PA 15213
POC: Chuck Thorpe
Tel: 412-268-3612
Fax: 412-268-5571

Caterpillar Industrial, Inc.
Automated Vehicle Systems
5960 Heisley Road
Mentor, OH 44060-1881
POC: David Heinz
Tel: 216-357-2246
Fax: 216-357-4410

Charles Stark Draper Laboratory
555 Technology Square, MS 27
Cambridge, MA 02139
POC: Bill Kaliardos
Tel: 617-258-1989
Fax: 617-258-2121

Chesapeake Laser Systems, Inc.
222 Gale Lane
Kennett Square, PA 19348-1734
POC: Larry Brown
Tel: 610-444-4253
Fax: 610-444-2321

Computer Sciences Corp.
7405 Alban Station Court
Suite B-206
Springfield, VA 22150
POC: Susan Hower
Tel: 703-912-7880
Fax: 703-912-6082

Control Engineering
8212 Harbor Springs Road
Harbor Springs, MI 49740
POC: Bruce Lindsay
Tel: 616-347-3931
Fax: 616-347-3342

Corning, Inc.
Telecommunications Products
Division
35 W. Market Street
Corning, NY 14831
POC: Vincent P. Martinelli
Tel: 607-974-3539
Fax: 607-974-3975

Cybermotion, Inc.
115 Sheraton Drive
Salem, VA 24153
POC: John Holland
Tel: 703-562-7626
Fax: 703-562-7632

David Sarnoff Research Center
201 Washington Road
Princeton, NJ 08540-6449
POC: Dr. Peter Burt
Tel: 609-734-2451
Fax: 609-734-2662

Denning Branch International
Robotics
1401 Ridge Avenue
Pittsburgh, PA 15233
POC: Alan Branch
Tel: 412-322-4412
Fax: 412-322-2040

Denning Mobile Robots, Inc.
(See Denning Branch International
Robotics)

Dinsmore Instrument Company
1814 Remell Street
Flint, MI 48503
POC: R.C. Dinsmore
Tel: 313-744-1330
Fax: 313-744-1790

Eltec Instruments, Inc.
PO Box 9610
Central Business Park
Daytona Beach, FL 32020-9610
POC: David Cima
Tel: 800-874-7780
Fax: 904-258-3791

Environmental Research Institute of
Michigan
Box 8618
Ann Arbor, MI 48107
POC: Frank Pont
Tel: 313-994-1200
Fax: 313-994-3890

ESP Technologies, Inc.
21 LeParc Drive
Lawrenceville, NJ 06848
POC: Susan Cox
Tel: 609-275-0356
Fax: 609-275-0356

General Microwave
5500 New Horizons Blvd.
Amityville, NY 11701
POC: Mathew Jacobs
Tel: 516-226-8900, X304
Fax: 516-226-8966

Georgia Institute of Technology
Mobile Robot Laboratory
College of Computing
Atlanta, GA 30332
POC: Prof. Ronald Arkin
Tel: 404-894-8209
Fax: 404-853-0957

Hamamatsu Corp.
360 Foothill Rd.
Bridgewater, NJ 08807
POC: Norman H. Schiller
Tel: 908-231-0960
Fax: 908-231-1218

Harris Technologies, Inc.
PO Box 6
Clifton, VA 22024
POC: Jim Harris
Tel: 703-266-0900
Fax: 703-968-8827

Hewlett-Packard Components
Customer Information Center
Building 49 AV
19310 Pruneridge Avenue
Cupertino, CA 95014
Tel: 800-752-9000

Hitachi Cable America, Inc.
50 Main Street
White Plains, NY 10606-1920
POC: Ray Ikeda
Tel: 914-993-0990
Fax: 914-993-0997

Honeywell, Inc.
Microswitch Division
11 West Spring Street
Freeport, IL 61032
POC: John Mitchell
Tel: 800-537-6945
Fax: 815-235-6545

Honeywell, Inc.
Military Avionics Division
11601 Roosevelt Boulevard
St. Petersburg, FL 33716-2202
POC: Jody Wilkerson
Tel: 813-579-6473
Fax: 813-579-6832

Honeywell, Inc.
Solid State Electronics Center
12001 Highway 55
Plymouth, MN 55441
POC: Tamara Bratland
Tel: 612-954-2992
Fax: 612-954-2051

Honeywell, Inc.
Technology Center
3660 Technology Drive
Minneapolis, MN 55418
POC: James E. Lenz
Tel: 612-951-7715
Fax: 612-951-7438

Honeywell Visitronics
(See Honeywell, Micro Switch
Division)

IBM Research
30 Saw Mill River Road
Hawthorne, NY 10532
POC: Jonathan Connell
Tel: 914-784-7853
Fax: 914-784-6307

Intelligent Solutions, Inc.
1 Endicott Avenue
Marblehead, MA 01945
POC: Jim Maddox
Tel: 617-639-8144
Fax: 617-639-8144

IS Robotics
Twin City Office Center, Suite #6
22 McGrath Highway
Somerville, MA 02143
POC: Colin Angle
Tel: 617-629-0055
Fax: 617-629-0126

Kaman Sciences
Remote Control Program
1500 Garden of the Gods Road
Colorado Springs, CO 80933-7463
POC: Doug Caldwell
Tel: 719-599-1285
Fax: 719-599-1942

Kearfott Guidance and Navigation
1150 McBride Avenue
Little Falls, NJ 07424
POC: James G. Koper
Tel: 201-785-6000, X5492
Fax: 201-785-5555

KVH Industries, Inc.
110 Enterprise Center
Middletown, RI 02842
POC: Sandy Oxx
Tel: 401-847-3327
Fax: 401-849-0045

LAAS - CNRS
7, avenue du Colonel Roche
31077 Toulouse Cedex, France
POC: Raja Chatila
Tel: (33) 61 33 63 28
Fax: (33) 61 33 64 55

Litton Industrial Automation
(See Saurer Automation Systems)

Macome Corp.
7-32-6 Nishikamata Ohta-ku
Tokyo 144 Japan
POC: S. Kamewaka

Magellan Systems Corp.
960 Overland Court
San Dimas, CA 91773
POC: Emile Yakoup
Tel: 909-394-6062
Fax: 909-394-7050

Magnavox Advanced Products and Systems
2829 Maricopa Street
Torrance, CA 90503
POC: Eric Furlong
Tel: 310-618-1200
Fax: 310-618-7074

Martin Marietta Aerospace Corp.
Space Systems Division
PO Box 179
Denver, CO 80201
POC: Wendell Chun
Tel: 303-971-7945
Fax: 303-971-4093

Massa Products Corp.
280 Lincoln Street
Hingham, MA 02043
POC: Paul Shirley
Tel: 617-749-4800
Fax: 617-740-2045

Massachusetts Institute of Technology
Artificial Intelligence Lab
545 Technology Square
Cambridge, MA 02139
POC: Anita Flynn
Tel. 617-253-3531
Fax: 617-253-0039

Merritt Systems, Inc.
2425 N. Courtenay Parkway
Suite 5
Merritt Island, FL 32953
POC: Daniel Wegerif
Tel: 407-452-7828
Fax: 407-452-3698

Microswitch Division
(See Honeywell, Inc.)

Millitech Corp.
PO Box 109
Deerfield, MA 01373-0109
POC: Ken Wood
Tel: 413-665-8551
Fax: 413-665-2536

Monash University
Department of Electrical and Computer Systems Engineering
Clayton, Australia VIC 3168
POC: Andrew Russell

Monitor Manufacturing, Inc.
44W320 Keslinger Road
PO Box 8048
Elburn, IL 60119-8048
POC: Thomas F. Meagher
Tel: 708-365-9403
Fax: 708-365-5646

Motorola, Inc.
Government and Systems Technology Group
8220 E. Roosevelt Road
PO Box 9040
Scottsdale, AZ 85252-9040
POC: Burt Woelkers
Tel: 602-441-7685
Fax: 602-441-7677

MTI Research, Inc.
313 Littleton Road
Chelmsford, MA 01824
POC: Edward N. MacLeod
Tel: 508-250-4949
Fax: 508-250-4605

Murata Electronics North America
2200 Lake Park Drive
Smyrna, GA 30080
POC: Satoshi Ishino
Tel: 404-436-1300
Fax: 404-436-3030

NAMCO Controls
5335 Avion Park Drive
Highland Heights, OH 44143
POC: Greg Miller
Tel: 800-NAM-TECH
Fax: 216-946-1228

NASA Goddard Space Flight Center
Robotics Branch, Code 714.1
Greenbelt, MD 20771
POC: John Vranish
Tel: 301-286-4031
Fax: 301-286-1613

NASA Jet Propulsion Laboratory
4800 Oak Grove Drive
Pasadena, CA 91109
POC: Larry Mathies
Tel: 818-354-3722
Fax: 818-354-8172

National Institute for Standards and Technology
Building 200, Room B124
Gaithersburg, MD 20899
POC: Marty Herman
Tel: 301-975-2000
Fax: 301-990-9688

National Research Council of Canada
Institute for Information Technology
Ottawa, Ontario, Canada, K1A 0R6
POC: Francois Blais
Tel: 613-993-7892
Fax: 613-952-0215

National Semiconductor Corp.
2900 Semiconductor Drive
P.O. Box 58090
Santa Clara, CA 95052-8090
Tel: 408-721-5000
Fax: 408-739-9803

Naval Command Control and Ocean Surveillance Center (NCCOSC)
RDT&E Division 5303
San Diego, CA 92152-7383
POC: Bart Everett
Tel: 619-553-3672
Fax: 619-553-6188

Naval Ocean Systems Center (NOSC)
(See Naval Command Control and Ocean Surveillance Center)

Naval Postgraduate School
Department of Computer Science
Monterey, CA 93940
POC: Prof. Bob McGhee
Tel: 408-656-2026
Fax: 408-656-2814

Naval Research Laboratory
Chemistry Division
Code 6177
Washington, DC 20375-5000
POC: Richard J. Colton
Tel: 202-767-0801
Fax: 202-767-3321

Navigation Technologies Corp.
740 Arques Avenue
Sunnyvale, CA 94086
POC: Daniel Udoutch
Tel: 408-737-3200
Fax: 408-737-3280

Nonvolatile Electronics, Inc.
11409 Valley View Road
Eden Prairie, MN 55344
POC: Jay Brown
Tel: 612-829-9217
Fax: 612-829-9241

NovAtel Communications Ltd.
6732 8 Street N.E.
Calgary, Alberta, Canada T2E 8M4
POC: Bryan R. Townsend
Tel: 403-295-4500
Fax: 403-295-0230

Oak Ridge National Laboratory
PO Box 2008
Oak Ridge, TN 37831-6304
POC: William R. Hamel
Tel: 615-574-5691
Fax: 615-576-2081

Odetics, Inc.
1515 South Manchester Highway
Anaheim, CA 92802-2907
POC: Tom Bartholet
Tel: 714-758-0300
Fax: 714-774-9452

OmniTech Robotics
2640 Raritan Circle
Englewood, CO 80110
POC: Dave Parish
Tel: 303-922-7773
Fax: 303-922-7775

Perceptron, Inc.
23855 Research Drive
Farmington Hills, MI 48335
POC: Dave Zuk
Tel: 810-478-7710
Fax: 810-478-7059

Phase Laser Systems, Inc.
14255 N. 79th Street
Suite 6
Scottsdale, AZ 85260
POC: Michael Brubacher
Tel: 602-998-4828
Fax: 602-998-5586

Philips Semiconductors
100 Providence Pike
Slatersville, RI 02876
POC: Ed Martins
Tel: 401-767-4458
Fax: 401-767-4403

Physical Security Equipment
Management Office
10101 Gridley Road
Suite 104
Fort Belvoir, VA 22060-5818
POC: Jerry Edwards
Tel: 703-704-2412
Fax: 703-704-2495

Polaroid Corp.
784 Memorial Drive
Cambridge, MA 02139
POC: Phil Jackman
Tel: 617-386-3964
Fax: 617-386-3966

Precision Navigation, Inc.
1235 Pear Avenue
Suite 111
Mountain View, CA 94043
POC: Mark Moran
Tel: 415-962-8777
Fax: 415-962-8776

Precision Technology, Inc.
4000 Chesswood Drive
Downsview, Ontario
Canada M3J 2B9
POC: Bruce Buck
Tel: 416-630-0200
Fax: 416-630-4414

Quantic Industries, Inc.
990 Commercial Street
San Carlos, CA 94070
Tel: 408-867-4074
Fax: same as above

Redzone Robotics
2425 Liberty Avenue
Pittsburgh, PA 15222
POC: Jeff Callen
Tel: 412-765-3064
Fax: 412-765-3069

RIEGL USA
Laser Measurement Systems
8516 Old Winter Garden Road #101
Orlando, FL 32835-4410
POC: Ted Knaak
Tel: 407-294-2799
Fax: 407-294-3215

Robotic Systems Technology
1110 Business Parkway
Westminster, MD 21157
POC: Scott Myers
Tel: 410-876-9200
Fax: 410-876-9470

Robotic Vision Systems, Inc.
425 Rabro Drive East
Hauppauge, NY 11788
POC: Howard Stern
Tel: 516-273-9700
Fax: 516-273-1167

Rockwell International
3200 East Renner Road
Richardson, TX 75082
POC: Larry Creech
Tel: 214-705-1704
Fax: 214-705-3284

Safety First Systems, Ltd.
42 Santa Barbara Drive
Plainview, NY 11803
POC: Alan Hersch
Tel: 516-681-3653
Fax: 516-938-6558

SAIC Bio-Dynamics
(See Robotic Systems Technology)

Sandia National Labs
PO Box 5800
Albuquerque, NM 87185-0860
POC: Paul Klarer
Tel: 505-844-2900
Fax: 505-844-5946

Sandia National Labs
Organization 9122
PO Box 5800
Albuquerque, NM 87185-0860
POC: John Sackos
Tel: 505-844-3033
Fax: 505-844-7020

SatCon Technology Corp.
161 First Street
Cambridge, MA 02142-1221
POC: Ralph Fenn
Tel: 617-349-0815
Fax: 617-661-3373

Saurer Automation Systems
11818 James Street
Holland, MI 49424
POC: Dwight Williams
Tel: 616-393-0101
Fax: 616-393-0331

Savi Technology, Inc.
450 National Avenue
Mountain View, CA 94043-2238
POC: Alan Bien
Tel: 415-428-0550
Fax: 415-428-0444

Schwartz Electro-Optics, Inc.
3404 N. Orange Blossom Trail
Orlando, FL 32804
POC: Robert Gustavson
Tel: 407-298-1802
Fax: 407-297-1794

Space Electronics, Inc.
4031 Sorrento Valley Blvd.
San Diego, CA 92121
POC: David Czajkowski
Tel: 619-452-4166
Fax: 619-452-5499

Sperry Marine, Inc.
Seminole Trail
Charlottesville, VA 22901
POC: Peter Arnold
Tel: 804-974-2000
Fax: 804-974-2259

Systron Donner Inertial Division
BEI Electronics
2700 Systron Drive
Concord, CA 94518-1399
POC: Scott Orlosky
Tel: 510-682-6161
Fax: 510-671-6590

Texas Instruments, Inc.
Defense Systems and Equipment
PO Box 655474, MS-37
Dallas, TX 75265
POC: Charles Hanson
Tel: 214-995-0874
Fax: 214-995-2231

Texas Instruments, Inc.
Nightsight
34 Forest Street
Attleboro, MA 02703
POC: Stan Kummer
Tel: 508-236-1396
Fax: 508-699-3242

Transitions Research Corp.
Shelter Rock Lane
Danbury, CT 06810
POC: John Evans
Tel: 203-798-8988
Fax: 203-791-1082

Trimble Navigation
P.O. Box 3642
Sunnyvale, CA 94088-3642
POC: Joel Avery
Tel: 408-481-8927
Fax: 408-481-2000

Tulane University
Mechanical Engineering Department
New Orleans, LA 70118-5674
POC: Prof. Fernando Figueroa
Tel: 504-865-5775
Fax: 504-865-5345

University of Michigan
1101 Beal Avenue
Ann Arbor, MI 48109-2110
POC: Dr. Johann Borenstein
Tel: 313-763-1560
Fax: 313-944-1113

University of Minnesota
111 Church Street SE
Minneapolis, MN 55455
POC: Prof. Max Donath
Tel: 612-625-2304
Fax: 612-625-8884

University of Nebraska
Department of Mathematics and
Computer Science
Omaha, NE 68182
Tel: 402-554-2800
Fax: 402-554-2975

University of New Brunswick
Geodetic Research Laboratory
Department of Geodesy and
Geomatics Engineering
Fredericton, N.B., Canada E3B 5A3
POC. Prof. Richard Langley
Tel: 506-453-5142
Fax: 506-453-4943

University of South Carolina
Swearingen Engineering Center
Columbia, SC 29208
POC: Prof. Joe Byrd
Tel: 803-777-9569
Fax: 803-777-8045

Unmanned Ground Vehicle Joint
Program Office
(See US Army Missile Command)

US Army Engineering Topographical
Laboratory (USAETL)
ATTN: CEETL-TL-SP
Building 2592
Fort Belvoir, VA 22060-5546
POC: Stephen DeLoach
Tel: 703-355-3026
Fax: 703-355-3176

US Army Missile Command
Unmanned Ground Vehicle Joint
Program Office, Building 5410
Redstone Arsenal, AL 35896-8060
POC: COL Jeff Kotora
Tel: 205-876-3988
Fax: 205-842-0947

Vehicle Radar Safety Systems, Inc.
10 South Gratiot
Mt. Clemens, MI 48043
POC: Charles Rashid

VORAD Safety Systems, Inc.
10802 Willow Court
San Diego, CA 92127
POC: Kevin Wixom
Tel: 619-674-1450
Fax: 619-674-1355

Watson Industries, Inc.
3041 Melby Road
Eau Claire, WI 54703
POC: William Watson
Tel: 715-839-0628
Fax: 715-839-8248

Wright Laboratories
Robotics Lab, Building 9738
Tyndall AFB, FL 32403-5319
POC: Ed Brown
Tel: 904-283-3725
Fax: 904-283-9710

Zemco Group, Inc.
(Last known address)
3401 Crow Canyon Road
Suite 201
San Ramon, CA 94583
POC: Peter Blaney

Zexel Corp.
37735 Enterprise Court
Suite 600
Farmington Hills, MI 48331
POC: Mike Rice
Tel: 810-553-9930
Fax: 810-553-9931

Index